MINERALIZATION, TEXTURAL AND ALTERATION CHARACTERISTICS OF THE ŞAHİNLİ (SIRAKAYALAR AND KARATEPE) LOW-SULFIDATION EPITHERMAL DEPOSIT (LAPSEKİ, NW TURKEY)

A THESIS SUBMITTED TO
THE GRADUATE SCHOOL OF NATURAL AND APPLIED SCIENCES
OF
MIDDLE EAST TECHNICAL UNIVERSITY

BY

GÜLNUR DİLEKLER

IN PARTIAL FULFILLMENT OF THE REQUIREMENTS
FOR
THE DEGREE OF MASTER OF SCIENCE
IN
GEOLOGICAL ENGINEERING

MAY 2022

Approval of the thesis:

MINERALIZATION, TEXTURAL AND ALTERATION CHARACTERISTICS OF THE ŞAHİNLİ (SIRAKAYALAR AND KARATEPE) LOW-SULFIDATION EPITHERMAL DEPOSIT (LAPSEKİ, NW TURKEY)

submitted by **GÜLNUR DİLEKLER** in partial fulfillment of the requirements for the degree of **Master of Science** i**n Geological Engineering, Middle East Technical University** by,

Prof. Dr. Halil Kalıpçılar
Dean, Graduate School of **Natural and Applied Sciences** _____

Prof. Dr. Erdin Bozkurt
Head of the Department, **Geological Engineering** _____

Assist. Prof. Dr. Ali İmer
Supervisor, **Geological Engineering, METU** _____

Examining Committee Members:

Prof. Dr. Tolga Oyman
Geological Engineering, Dokuz Eylül University _____

Assist Prof. Dr. Ali İmer
Geological Engineering, METU _____

Prof. Dr. İlkay Kuşcu
Geological Engineering, Muğla Sıtkı Koçman University _____

Assoc. Prof. Dr. Fatma Toksoy Köksal
Geological Engineering, METU _____

Assoc. Prof. Dr. Kaan Sayıt
Geological Engineering, METU _____

Date: 06.05.2022

I hereby declare that all information in this document has been obtained and presented in accordance with academic rules and ethical conduct. I also declare that, as required by these rules and conduct, I have fully cited and referenced all material and results that are not original to this work.

Name Last name : Gülnur Dilekler

Signature :

ABSTRACT

MINERALIZATION, TEXTURAL AND ALTERATION CHARACTERISTICS OF THE ŞAHİNLİ (SIRAKAYALAR AND KARATEPE) LOW-SULFIDATION EPITHERMAL DEPOSIT (LAPSEKI, NW TURKEY)

Dilekler, Gülnur
Master of Science, Geological Engineering
Supervisor : Assist. Prof. Dr. Ali İmer

May 2022, 148 pages

The Şahinli Au-Ag deposit is located in Lapseki (Çanakkale), within the NW part of the Biga Peninsula. Mineralized veins are hosted in Permo-Triassic Çamlıca metamorphics and dacite porphyries of middle Eocene Beyçayır volcanics. Au-Ag mineralization occurs in two distinct zones, the Sırakayalar and Karatepe sectors, which occupy eastern and western flanks of a NW-trending steeply-incised valley, respectively. Karatepe comprises a series of structurally-controlled NNW- and E–W-trending, steeply-dipping quartz veins hosted within dacite porphyry and mica schist. Mineralized veins in Sırakayalar, however, have been largely disrupted and displaced except for locally-preserved rootless veins. These veins are preserved as blocks within an intensely oxidized clay-cemented talus separated from the underlying metamorphic basement by a damage zone. Unoxidized mineralized veins were also observed within upper levels of the schists. Karatepe and Sırakayalar orebodies show many similarities in terms of ore/gangue mineralogy, alteration styles, vein paragenesis, and textural characteristics. Periodic hydrothermal activity in both areas resulted in development of a variety of vein textures from early massive silica to later bladed, crustiform-colloform, and cockade textures, most of which have been later brecciated episodically. Massive gray quartz veins with Au°,

electrum, pyrite, and arsenopyrite yield highest Au-Ag grades. Wall-rock alteration is characterized by an inner zone of silicification enveloped by quartz-sericite ±kaolinite ±chlorite ±adularia alteration. The Şahinli mineralization exhibits characteristics of low-sulfidation epithermal deposits worldwide and in Biga Peninsula, including the adjacent Lapseki Au deposit as well as Madendağ and Küçükdere deposits. Disrupted veins at Sırakayalar represent the first example of a buried epithermal system in Biga Peninsula and suggests potential for similar epithermal Au-Ag mineralization in the region under younger cover.

Keywords: Low-sulfidation epithermal, gold-silver, Lapseki, Biga Peninsula, Cenozoic

ÖZ

ŞAHİNLİ (SIRAKAYALAR VE KARATEPE) DÜŞÜK-SÜLFİDASYONLU EPİTERMAL AU-AG YATAĞININ (LAPSEKİ, KB TÜRKİYE) CEVHERLEŞME, DOKUSAL VE ALTERASYON ÖZELLİKLERİ

Gülnur, Dilekler
Yüksek Lisans, Jeoloji Mühendisliği
Tez Yöneticisi: Dr. Öğr. Üyesi Ali İmer

Mayıs 2022, 148 sayfa

Şahinli Au-Ag yatağı, Lapseki'de (Çanakkale), Biga Yarımadasının KB kesiminde yer almaktadır. Cevherli damarlar Permo-Triyas Çamlıca metamorfikleri ve Orta Eosen Beyçayır volkaniklerine ait dasit porfiriler içerisindedir. Au-Ag cevherleşmesi, KB yönelimli dik bir oyuntu vadisinin sırasıyla doğu ve batısındaki Sırakayalar ve Karatepe sektörleri olarak adlandırılmış iki ayrı bölgede gerçekleşmiştir. Karatepe, dasit porfiri ve mika şistler içerisinde yer alan, yapısal kontrollü KKB- ve D–B-yönelimli, dik açılı bir dizi kuvars damarından oluşmaktadır. Sırakayalar cevherli damarları ise kısmen korunmuş köksüz bazı damarlar haricinde genelde parçalanmış ve yer değiştirmiş haldedir. Bu damarların çoğu, kuvvetli derecede oksitlenmiş kil çimentolu ve alttaki metamorfik taban birimlerinden bir hasar zonuyla ayrılmış birikinti malzemesi içerisinde korunmuş haldedir. Oksitlenmemiş cevherli damarlar şistlerin üst seviyelerinde de gözlenmektedir. Karatepe ve Sırakayalar cevherleşmeleri cevher/gang mineralojisi, alterasyon tipleri, damar parajenezi ve dokusal özellikler açısından pek çok benzerliğe sahiptir. Her iki bölgede aralıklarla gerçekleşen hidrotermal süreçler, periyodik olarak breşleşme gösteren, erken evrede masif silis sonrasında bıçaksı, kabuksu-kolloform ve kokart dokuların gelişimine neden olmuştur. En yüksek Au

ve Ag tenörleri Au°, elektrum, pirit ve arsenopirit içeren masif gri kuvars damarları içerisinde gözlenmiştir. Yan kayaç alterasyonu, içteki silisleşme zonunu saran kuvars-serizit ±kaolinit ±klorit ±adularya alterasyonuyla karakterizedir. Şahinli cevherleşmesi dünyadaki tipik düşük-sülfidasyonlu epitermal yataklarla ve Biga Yarımadası'ndaki komşu Lapseki Au yatağı ile Madendağ ve Küçükdereyle benzerlik göstermektedir. Sırakayalardaki taşınmış damarlar Biga Yarımadası'nda bu tarz gömülü bir epitermal sistemin ilk örneğini temsil etmektedir. Buna göre bölgede genç örtü altında gömülü benzer epitermal Au-Ag cevherleşme potansiyeli bulunmaktadır.

Anahtar Kelimeler: Düşük-sülfidasyon epitermal, altın-gümüş, Lapseki, Biga Yarımadası, Senozoyik

To future

ACKNOWLEDGMENTS

Firstly, I would like to express my gratitudes to my advisor Assist Prof. Dr. Ali İmer who gave me so much support, knowledge and wise guidance of mineral deposits discipline in geology so that this dissertation is actualized. He is always thrustworthy and openhearted. Secondly, I would like to express my appreciation to Esan Ezcabaşı Industrial and Raw Material company for permission and funding of the project, and Mustafa Tuna Kaskatı, head of exploration department, and İbrahim Uçar, exploration manager of the company, for their all supports.

This thesis would not be finished without my friends and/or colleagues who are Ulviye Demirörs, Selma Ağbaba Aytekin, Hande Vona, Oğuzhan Gümrük, Akın Çil, Uğur Can Bayhan and Yağmur Han. Orhan Karaman, Ferda Çetin and Tahsin Kıray deserve the greatest respect for their helps during field studies, sample collections and thin section preparations. Hande Vona assisted me during TerraSpec measurements, therefore I am sending my deep thanks to her for it also.

Special appreciation goes to Ali Özkanlı who is my past, present and future. He always gave his mere and emotional support. He does not give up thrusting me during this challenging process. Thanks to him for his endless love.

Finally and most importantly, I can not express my endless love and gratitude to my family. My mother Havva Dilekler and my sister İlknur Dilekler were always with me and help me to walk this way. They always standed me up when I fell on this way. My father Mahmut Dilekler loved me so much. He was my hero. He is always in my heart and in my mind.

TABLE OF CONTENTS

LIST OF TABLES

TABLES

LIST OF FIGURES

FIGURES

CHAPTER 1

INTRODUCTION

Biga Peninsula in northwestern Turkey comprises part of a collisional tectonic belt developed following opening and episodic subduction of the Tethyan oceanic basins that once remained between continental fragments derived from Laurasia and Gondwana (Şengör and Yılmaz, 1981; Okay and Tüysüz, 1999). Deposits that usually occur in clusters that characterizing several economically important mineral provinces, subprovinces, and districts, and Biga Peninsula hosts a large number of metallic ore. Ongoing exploration efforts across the Biga Peninsula help not only to improve our understanding of the geology of the region, but also to understand its economic potential in terms of base and precious metal mineralization.

1.1 Thesis Objectives

This thesis focuses on the Şahinli (Sırakayalar and Karatepe) low-sulfidation epithermal Au-Ag deposit, and aims to understand the general aspects of the mineralized system and to identify the geological controls on ore formation. As epithermal mineralization occurs in two distinct domains, these will be evaluated in a comparative manner since relationship between Karatepe and Sırakayalar mineralization has not been well-understood. The general outcomes will also be integrated into the Cenozoic metallogeny of the Biga Peninsula. The main thesis objectives that will be addressed are identification of the geological framework of the Karatepe and Sırakayalar Sectors, and identification of the ore and gangue mineralogy, alteration styles, textural features and paragenesis of the epithermal veins. The thesis objectives were addressed through field work, drill core and surface sampling, and petrographic analyses.

1.2 Location and Setting

The Şahinli tenement is located in the Lapseki area (Çanakkale) within NW Biga Peninsula (NW Turkey), about 4 km NE of the town of Şahinli (Fig. 1.1). Gold-silver mineralization at Şahinli occurs mainly within quartz veins in two separate zones, the Karatepe and Sırakayalar Sectors, located approximately 1 km apart from each other. The tenement also lies immediately to the north of the adjacent Lapseki gold mine of TÜMAD Mining. There is also Şahinli/Tespihdere mineralization including Sırakayalar vein zones in literature studied by Yılmaz et al. (2010) mentioned by same names; however, its location is on a different area, south of Şahinli mentioned in this study.

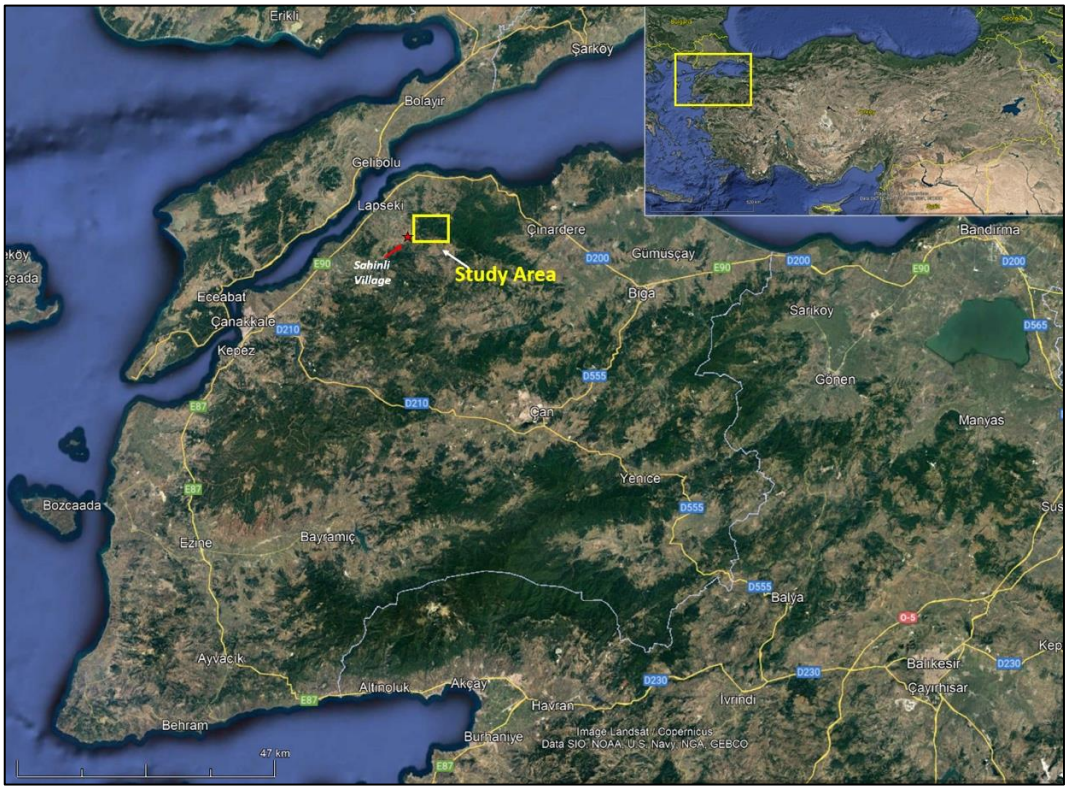

Figure 1.1. Location of the study area (Google Earth image).

In the study area, mineralized veins are spatially associated with Permo-Triassic basement units of Çamlıca metamorphics, and andesite to dacite porphyries of Cenozoic age. Middle Miocene rhyolites and ignimbrites as well as Late Miocene–

Pliocene continental sediments comprise post-mineralization cover units in the deposit area. Au-Ag mineralization occurs in two distinct zones, identified as Sırakayalar and Karatepe mineralized systems, which occupy eastern and western flanks of a NW-trending steeply-incised valley, respectively.

1.3 Previous Studies

The current project on the Şahinli deposit was conducted when the tenement was owned by ESAN Mining (ESAN), and had been previously explored by Atlantis Mining. In 2011, ESAN completed a reconaissance exploration programme through rock, soil, and trench sampling combined with geopysical surveys. Initial drilling by ESAN commenced in 2012, and continued until 2019. The Sırakayalar sector of the tenement consisted of waste dump and stock areas as well as narrow adits remaining from ancient mining activities during Roman times.

Prior to ESAN's work, Yıldırım and Cengiz (2004) described Şahinli as an epithermal-style Au-Ag mineralization based on the follow-up studies tracing significant arsenic and antimony anomalies higlighted at Adatape by the Mineral Research and Exploration Institute of Turkey (MTA). Primary Au mineralization in study area was related to quartz veins and silicified zones within both schist and volcanics lithologies. Yıldırım and Cengiz (2004) also noticed gold enrichment in Plio-Quaternary terrace deposits, Miocene–Pliocene conglomerate, and in tuffs and agglomerates.

Later, Keser (2015) studied variably-textured epithermal quartz (colloform, cockade, bladed and saccharoidal textures) and indicated that these epithermal features developed in highly deformed Paleozoic schists cross-cut and overlain by andesitic-dacitic volcanics.

In another study on Şahinli mineralization, Clark (2014) focused on geochemical and mineralogical aspects of the epithermal system and emphasized the role of low to moderate temperature, low-salinity fluids of dominantly meteoric origin in gold-

silver deposition. Several distinct paragenetic stages were identified in this study as early massive silica development later followed by coarsely-crystalline quartz and jigsaw breccias.

1.4 Methodology

This study comprised both field and laboratory studies conducted between early 2019 and late 2020. Field work mainly included confirmation and updating of geological maps prepared by ESAN geologists, and surface and drill core sampling of both Sırakayalar and Karatepe systems. A total of 82 drill core samples were collected from 6 diamond drill holes, two representing the Karatepe vein system and another four from the Sırakayalar sector. All sampled drill holes were quick-logged, and collected samples were photographed, initially on site and later at the Department of Geological Engineering of the Middle East Technical University (METU).

In order to understand the classification the sub-volcanic unit based on immobile element concentrations (Nb/Y vs. Zr/Ti plot of Pearce, 1996), 21 samples from six drillholes for the Karatepe Member were utilized.

Collected drill core and surface samples were prepared into polished thin sections for identification of ore and gangue minerals, alteration styles, ore textures, and mineral paragenesis based on different stages of quartz textures. Petrograpic examination of 82 polished thin sections was undertaken at METU using a transmitted- and reflected-light polarized microscope.

A number of selected samples representing various alteration styles from Karatepe and Sırakayalar zones were analyzed using an ASD TerraSpec 4 Hi-Res Mineral Spectrometer for spectral characterization of alteration minerals. Raw data was obtained by TSG software and short-wave infra red (SWIR) profiles were constructed using Spectragryh software. SWIR spectroscopy detects the reflected energy changed by bending and stretching of bonds and vibrations of molecules

within 1000–2500 nm wavelength ranges (Clark, 1999). Certain mineral phases such as phyllosilicates (includiing clay minerals) and carbonates show characteristic spectra through absorption of specific molecular groups of OH, H_2O and cation hydroxyl bonds of Al-OH, Fe-OH and Mg-OH include by crystal lattice of the minerals (Hunt, 1977). Absorption energies account for distinct wavelength positions; for example, OH and H_2O features can be detected by 1400 and 1900 nm while cation bonds are detected by 2200, 2250 and 2330 nm wavelength ranges (Hauff, 2008).

For a number of selected quartz vein intervals (391 intervals of 38 drillholes for Karatepe, 268 intervals of 55 drillholes for Sırakayalar), their macro-textures and corresponding geochemical results of Au and Ag were examined.

In order to understand the relationship between alteration styles and gold-silver mineralization, molar ratio plots were prepared following the formulations of Warren et al. (2007). Molar ratio plots can give information regarding mass transfer associated with alteration of volcanics lithologies in hydrothermal environments (Giggenbach, 1988). One of the significant mass change in altered volcanics are associated with K-metasomatism, and K-rich mineral assemblages are increased through the mineralization (Warren et al., 2007). During K-metasomatism, Na and Ca are also lost while K is gained (Warren et al., 2007). In order to obtain such information, (2Ca+Na+K)/Al (molar) and K/Al (molar) ratios were used and plotted in same versus graph. Firstly, multi element data were filtered for Ca, Na, K and Al; and then their molar values were measured to get the ratios. Molar ratio diagrams were plotted using multi-element geochemical data of least-altered and altered porphyritic host rocks intersected in diamond drill holes.

CHAPTER 2

EPITHERMAL DEPOSITS: A REVIEW

2.1 Conceptual Framework of Epithermal Precious Metal Deposits

In hydrothermal systems, mineral deposition is considered to take a place as a consequence of fluctuations in physico-chemical variables of hydrothermal fluids such as in pressure, temperature, acidity, salinity, and oxygen fugacity as well as in concentrations of ligands including sulfur and carbon species. Such variations may result from ore depositional processes mainly including cooling, decompression, fluid mixing, and water-rock interactions (Cooke and McPhail, 2001). Besides, one of the most important deposit types among the class of hydrothermal ore deposits are epithermal deposits, and these also form in environments that are exposed to physico-chemical changes of metasomatic events.

Epithermal deposits are significant sources for Au and Ag and they may also contain economic concentrations of Cu, Pb, Zn, Hg, Sb, Te, Se and sometimes platinum group elements (Cooke and Simmons, 2000; Hedenquist et al., 2000; Sillitoe and Hedenquist, 2003; Simmons et al., 2005). Epithermal ores most commonly occur as veins, disseminations, and breccias usually hosted in volcanic and volcanoclastic rocks, and sometimes in metamorphic or sedimentary basement lithologies (Cooke and Simmons, 2000; Simmons et al., 2005).

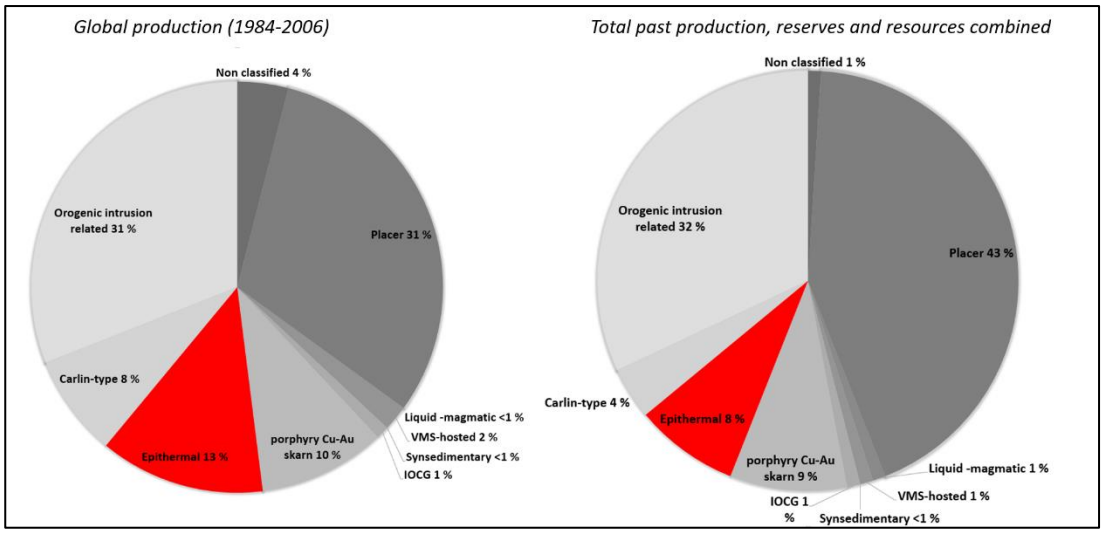

Figure 2.1. Pie chart showing comparisional significances of different ore deposits with gold commodity considering their global production between 1984–2006 and their total past reserves, resources and productions. (Frimmel, 2008)

Many epithermal deposits are concentrated around the continental, oceanic arc and back-arc systems along the Circum-Pacific Belt and also along the Tethyan orogenic belt. The latter extends from southern Europe in the west to Western Pacific in the east (Richard, 2014). According to Frimmel (2008), epithermal ores comprise about 13% of recent global gold production and 8% of total past production, reserves, and resources of gold (Fig. 2.1). Among these, the largest gold endowments come from intermediate-sulfidation epithermal deposits in addition to porphyry deposits, followed by low-sulfidation epithermal deposits. The latter is usually characterized by relatively small orebodies but with highest-grades, including the Cenozoic-age deposits of the western Tethyan belt (Baker, 2019).

Most active geothermal and volcanic-hydrothermal systems are considered as responsible for discharging of a wide spectrum of heated hydrothermal fluids that subsequently form epithermal deposits (Sillitoe, 2015; Fig. 2.2). Base and precious metal mineralization in epithermal systems form over temperatures ranging from <150^{o}C to ~300^{o}C, and within the uppermost part of the crust from near surface down to about 1.5 km depth (White and Hedenquist, 1995; Cooke and Simmons, 2000; Hedenquist et al., 2000, Simmons et al., 2005).

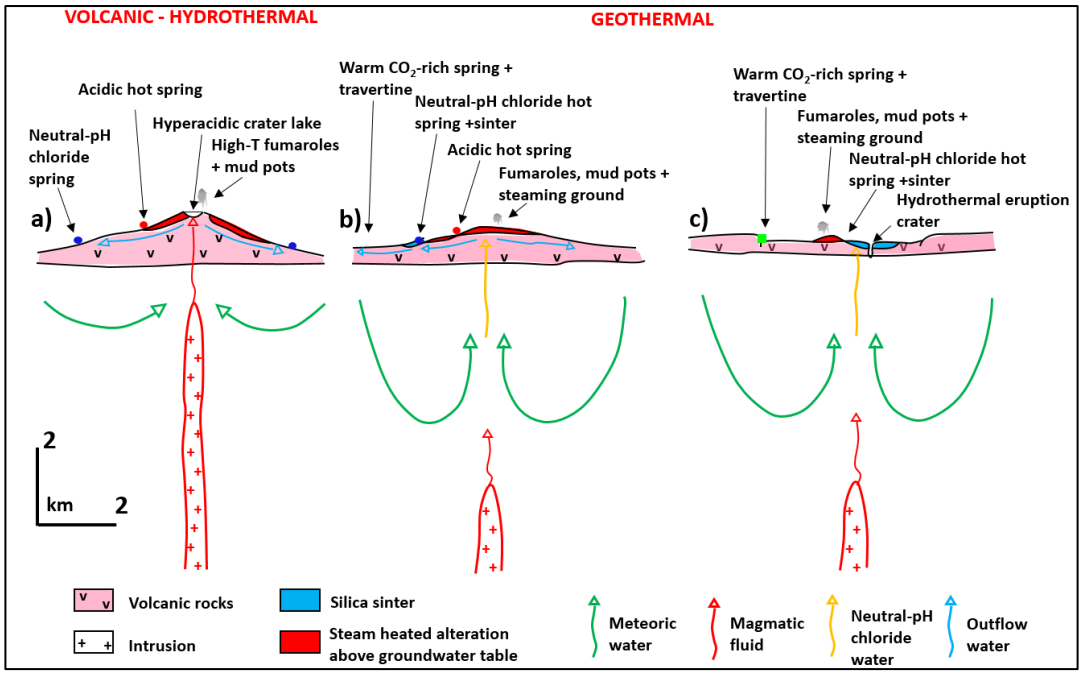

Figure 2.2. Illustrative representation for active and hot hydrothermal systems with their surficial features and roles of different fluid types. a) Upper portions of shallow intrusions represented as volcanic-hydrothermal systems. b) High relief terrain and deep intrusion represented as geothermal systems. c) Low-relief terrain and deep-seated intrusion represented as geothermal systems (Sillitoe, 2015).

The term "epithermal" was initially used by Lindgren (1933) at the beginning of the 20th century to refer to shallow depth of formation of ore mineralization, which is typically hosting Au, Ag, and base metals. Lindgren's interpretation of epithermal systems was a modification after Ransome's (1907) "Goldfield-type" and Emmons's (1918) "alunite-kaolinite-gold type" deposits (Table 2.1). Lindgren (1933) also distinguished epithermal deposits related to shallow volcanic environments in the upper crustal levels (i.e. the epizone) from mesothermal gold systems that form at much greater depths, and from relatively higher temperature fluids.

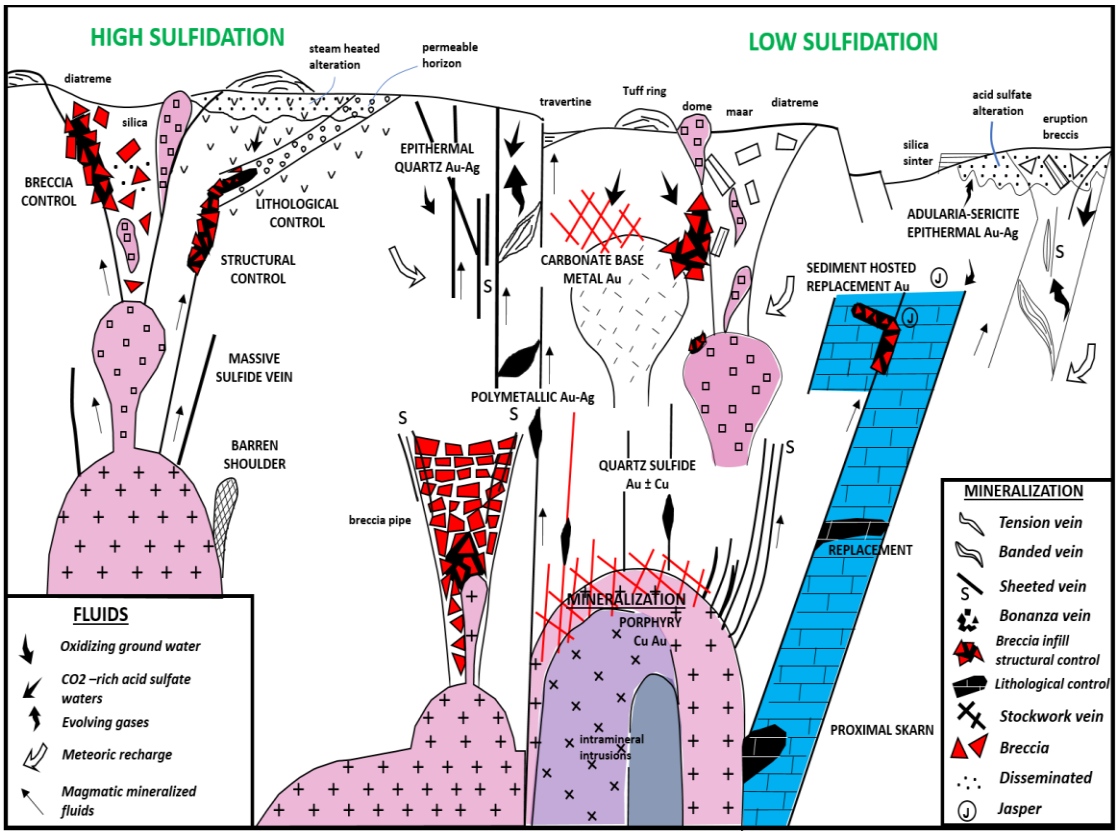

Figure 2.3. Conceptual model for both low- and high-sulfidation epithermal and also porphyry mineralizations at rift and arc magmatic settings (Corbett, 2002).

Table 2.1 . Early classification scheme used for epithermal deposits (Sillitoe & Hedenquist, 2003)

	High sulfidation	**Intermediate sulfidation**	**Low sulfidation**
Ransome (1907)	Goldfield Type		
Emmons (1918)	Alunitic-kaolinitic Au veins	Sericitic Zn-Ag veins	Au-Ag-adularia veins Fluoritic tellurium-adularia Au veins
Lindgren (1933)	Au-alunite deposits	Au-quartz veins in andesite	
		Argentite-Au quartz veins	Au quartz veins in rhyolite
		Argentite veins	Au telluride veins
		Base metal veins	Au selenide veins

Over the past few decades, early models on epithermal deposits have been considerably modified with the help of improved analytical techniques. Consequently, different styles of mineralization showing distinct characteristics were described. Recent studies by Hedenquist et al. (2000) and Sillitoe and Hedenquist (2003) classified epithermal deposit types into three sub-groups as high-, intermediate-, and low-sulfidation types. Principal characteristics of these mineralization styles (Table 2.2) have been developed based on mineralization styles, proximal alteration types, gangue and ore mineral phases, relative sulfidation and oxidation states (fS_2 and fO_2), and metal abundances (Einaudi et al., 2003; Sillitoe and Hedenquist 2003; Sillitoe, 2015). Among these, variations in the sulfur and oxygen fugacities of ore-forming fluids as a function of temperature has the primary control on stabilities of various sulfide and sulfate mineral assemblages. For instance, high-sulfidation epithermal systems are characterized by their oxidized sulfur species such as SO_2, SO_4^{2-}, and HSO^{4-} in ore fluids, whereas reduced sulfur species (e.g., HS^-, H_2S) are stabilized in low-sulfidation epithermal systems (Seward, 1973; White and Hedenquist, 1995; Sillitoe and Hedenquist, 2003).

Table 2.2 Principal field-based characteristcs of sub-types of epithermal deposits (Sillitoe and Hedenquist 2003; Sillitoe, 2015)

Epithermal Type	**High-sulfidation (HS)**		**Intermediate-sulfidation (IS)**	**Low-sulfidation(LS)**	
Main mineralization styles	Steep and shallowly inclined replacement bodies, hydrothermal breccias		Veins, stockworks	Veins, stockworks, disseminated bodies	
Main proximal alteration styles	Silicification, vuggy residual quartz, quartz-alunite		Silicification, quartz-sericite/illite	Silicification, quartz-adularia-illite	
Main gangue minerals	Quartz, alunite, barite		Quartz, calcite, manganoan carbonates, rhodonite, adularia	Quartz, chalcedony, adularia	
Silica gangue	Massive fine-grained silicification and vuggy residual quartz		Vein-filling crustiform and comb quartz	Vein filling crustiform and colloform chalcedony and quartz	
Sulfide abundance	High (10-80 vol.%)		Moderate (5-30 vol.%)	Low (1-5 vol.%)	
Sulfidation-state indicators	Enargite/luzonite/famatinite		Tetrahedrite, chalcopyrite, low-Fe sphalerite	Pyrrhotite, arsenopyrite, high-Fe sphalerite	
Typical metal signature	Au-Ag-Cu ± Bi ± Te		Ag-Au-Zn-Pb-Mn ± Cu	Au ± Ag ± Se ± Mo	
Magma type	Oxidized magma	Reduced magma		Subalkaline magma	Alkaline magma
Genetically related volcanic rocks	Mainly andesite to rhyodacite	Rhyodacite	Principally andesite to rhyodacite but locally rhyolite	Basalt to rhyolite	Alkali basalt to trachyte

2.1.1 High-Sulfidation Epithermal Deposits

High-sulfidation (HS) epithermal deposits are one of the major sub-types of epithermal systems and are important sources of precious metals as well as of copper. HS epithermal deposits are usually characterized by smaller orebodies compared to their low-sulfidation counterparts with few exceptions such as the giant Yanacocha

deposit in Peru and El Indio in Chile (Jannas et al., 1990; Jannas et al., 1999; Teal and Benavides, 2010).

HS epithermal systems are commonly located proximal to a magmatic source supplying heat, volatiles, and metals (Arribas, 1995; Rye et al., 1992; Taylor, 2007). Mineralization typically occurs within andesitic-dacitic volcanic complexes (e.g., stratovolcanoes and dome complexes) often underlain by sub-volcanic intrusions (Sillitoe and Bonham, 1984; Sillitoe and Hedenquist, 2003; Sillitoe, 2015). In some districts HS epithermal systems may develop within the same magmatic complex with underlying porphyry systems with which they are also genetically-related (Hedenquist et al., 1998 and 2000; Vila and Sillitoe, 1991; Rinne et al., 2018). Associated magmatism in such settings is generally calc-alkaline in character with relatively oxidized and water-rich magmas, not only considered as fertile for formation of high-sulfidation epithermal systems but also for development of porphyry-type deposits at depth (Simmons et al., 2005; Sillitoe and Hedenquist, 2003). Tectonic settings of high-sulfidation systems are magmatic arcs generally undergoing neutral to mildy extensional stress state, but few districts (e.g. Lepanto, Philippines and Pascua-Lama, Chile-Argentina) also developed during compression (Sillitoe and Hedenquist, 2003).

Alteration mineralogy with leached silicic host rocks of (i.e., residual vuggy quartz alteration) HS epithermal ores is usually characterized by quartz-alunite-kaolinite± pyrophyllite±dickite halos (Hedenquist et al., 2000; Fig. 2.4). HS epithermal systems are formed from highly-oxidized low pH fluids, creating vuggy silica and quartz-alunite alteration assemblages at early stages of corrosive hydrothermal activity (Stoffregen, 1987; Sillitoe, 2015). Ore mineralogy is commonly constituted by Cu sulfides such as chalcopyrite and enargite, luzonite/famatinite, whereas arsenopyrite and sphalerite are uncommon (White et al., 1995; White and Hedenquist, 1995).

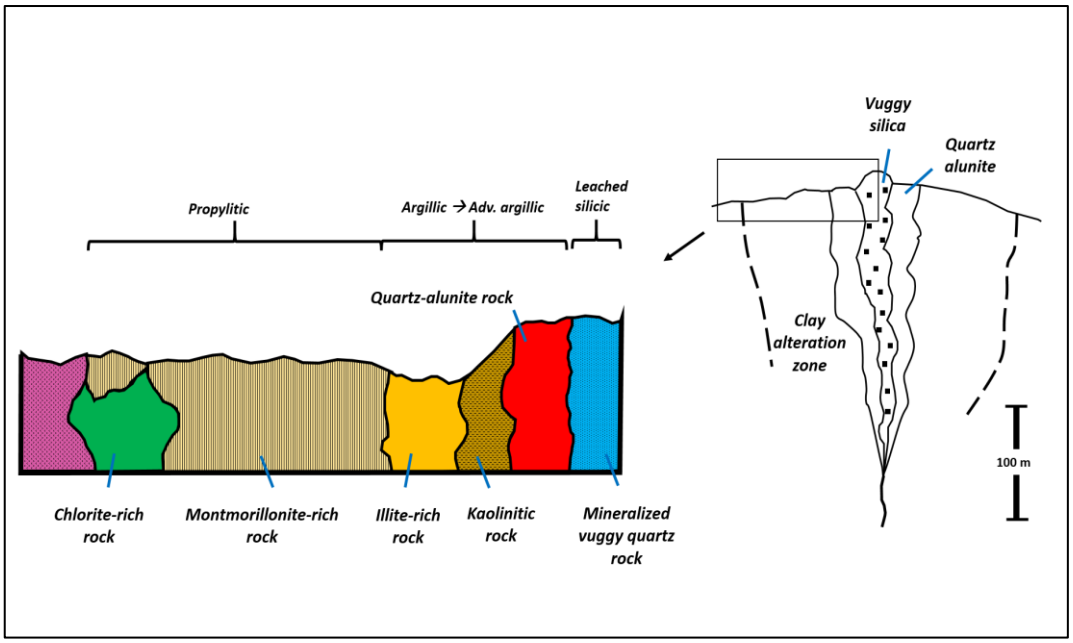

Figure 2.4. Illustration showing cross-sectional view of alteration zonation of a typical high-sulfidation epithermal orebody around a silicic core (Hedenquist et al., 2000; after Stoffregen, 1987).

2.1.2 Low-Sulfidation Epithermal Deposits

Low-sulfidation (LS) epithermal deposits are also generally mined for their precious metal contents, but many of them also have some concentrations of base metals hosted in their sulfide minerals. Proposed tectonic settings for LS epithermal systems are magmatic arcs subjected to extension leading to rifting and post-collisional rifting (Sillitoe and Hedenquist, 2003; Fig. 2.5). Relatively reduced and water-poor magmas, like those of bimodal basalt-rhyolite suites, are dominantly referred to be responsible for LS epithermal deposits in rifted settings (e.g. Mule Canyon, North-Central Nevada; John et al. 2003; Simmons et al., 2005). On the other hand, many LS epithermal systems are also associated with calc-alkaline dacites and rhyolites formed as a result of partial melting of mantle-wedge in continental subduction zones or in late-stage back-arc or post-collisional settings (du Bray, 2017). LS epithermal ores usually ocur as veins, stockworks, and breccias that are generally formed from relatively reduced, and near neutral-pH fluids; and such fluids are largely in

equilibrium with their surrounding host rocks in some cases (Hedenquist et al., 2000).

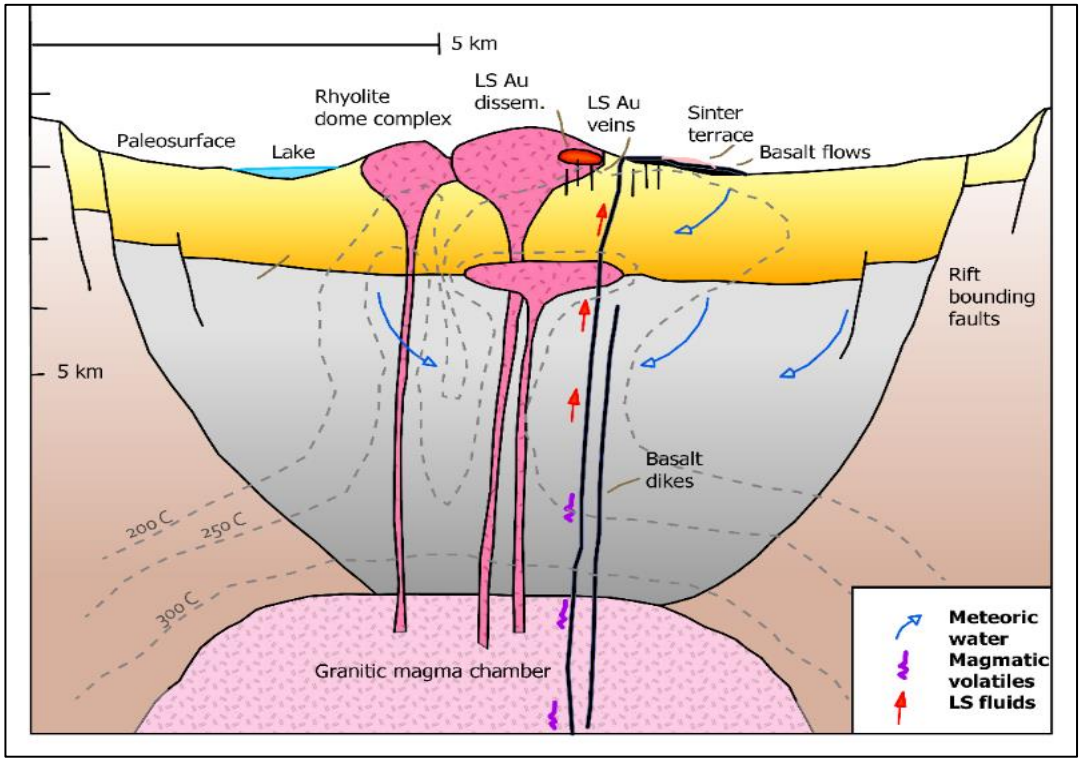

Figure 2.5. Shematic cross-sectional view showing low-sulfidation epithermal mineralization at rifted settings with bimodal volcanism (Sillitoe and Hedenquist, 2003; Taylor, 2007).

Mineralized veins in LS epithermal systems are represented by quartz-adularia-carbonate veins with sulfides, sulfosalts, and selenides, often displaying sericitic or clay-rich alteration halos (Hedenquist et al., 2000; Fig. 2.6). Nevertheless, there are some controls on hypogene alteration mineralogy for LS epithermal systems as to temperature and depth changes (Table 2.3.).

Table 2.3 Depth and temperature controls on hypogene alteration characteristics of low-sulfidation epithermal deposits, (RB): bimodal rhyolite-basalt, (AR): andesite-rhyodacite (Hedenquist, 2000)

Approx. Depth (m)	Paleosurface or paleowater	0-150 m	150-300 m	300-500 m	500-1000 m
Temp (ºC)	100-200	100-200	200-230	230-260	260-300+
Advanced argillic alteration	Steam-heated (kaolinite-alunite) blanket over water table; residual opal	Steam heated (kaolinite-alunite) overprint along fractures	Rare overprint	None	None
Silicic alteration	Sinter around hot springs, horizon of chalcedony at water table	Colloform chalcedony veins, wall-rock silicification	Qtz veins, fine bands open-space filling	Qtz veins w/coarse bands	Minor qtz veins, minimal silicification
Argillic alteration	Kaolinite-smectite	Smectite, mixed illite/smectite; marginal halo to 1000 m depth	Minor illite/smectite to illite	Illite	Illite, illite/smectite halo on margin
Sericitic alteration	None	None	None	Illite ± chlorite	2M mica
Propylitic		Chlorite	Chlorite, trace epidote	Chlorite ± epidote	Epidote
Sulfides (RB)	Pyrite-marcasite at base	Pyrite	Pyrite, arsenopyrite, pyrrhotite, Ag selenides	Pyrite, arsenopyrite, pyrrhotite (Ag selenides)	Minor base metal sulfides, sphalerite-galena-chalcopyrite
Sulfides (AR)	Pyrite-marcasite at base	Pyrite	Tetrahedrite-tennantite	Major base metal sulfides	Base metal sulfides

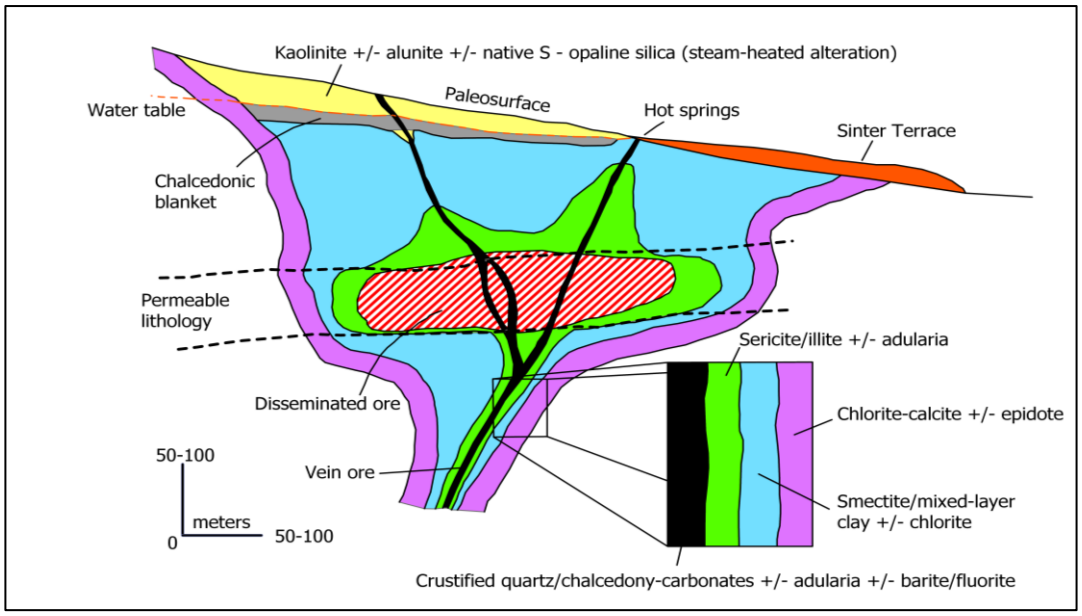

Figure 2.6. Shematic cross-sectional view showing alteration zones and their mineral assemblages of low-sulfidation epithermal mineralization (Hedenquist, 2000).

Boiling is generally regarded as the most effective process that leads to high-grade precious metal deposition in epithermal deposits, particularly in LS-type systems (Reed and Spycher, 1985; Berger and Henley, 1989). Boiling takes place along structurally-controlled vertical to subvertical upflow zones, and is controlled by hydrostatic pressure and temperature conditions (e.g., Reed and Spycher, 1985; Simmons and Browne, 2000; Simmons et al., 2005). As the hydrothermal fluid boils, gases such as CO_2 and H_2S partition into the vapor phase, thereby causing destabilization of gold-bisulfide complexes and an increase in pH of the liquid phase (Seward, 1989; Seward et al., 2014). Consequently, carbonate minerals get stabilized in the form of platy/bladed crystals, and adularia precipitates together with quartz-carbonate±illite assemblages often alongside base metal sulfides in low-sulfidation ore veins (Simmons et al. 2005). In addition to bladed calcite texture, crustiform bands of chalcedony, open space fillings, colloform bands caused by colloidal silica accumulations and hydrothermal brecciations of veins creating some jigsaw patterns can be observable in LS epithermal systems (Lindgren, 1933; Hedenquist et al., 2000). Whereas Ag:Au ratios in HS epithermal deposits are highly variable, low-sulfidation deposits tend to have relatively high Ag:Au ratios (Taylor, 2007).

2.1.3 Intermediate-Sulfidation Epithermal Deposits

Intermediate-sulfidation (IS) epithermal deposits display some characteristics of high- and low-sulfidation epithermal systems. For example, similar to HS epithermal deposits, IS epithermal systems are associated with calc-alkaline andesitic-dacitic volcanism, but their ore mineralogies consisted by chacopyrite-tetrahedrite/tennantite-sphalerite-galena and alteration styles with quartz-adularia-sericite/illite-carbonate alteration are similar to the low-sulfidation epithermal systems (Hedenquist et al., 2000; Sillitoe and Hedenquist, 2003). However, the most distinctive feature of IS epithermal deposits is their higher fluid salinities compared to both HS and LS deposits, which is sometimes responsible for higher concentrations of Ag and particularly of base metals (Hedenquist et al., 2000; Sillitoe and Hedenquist, 2003; Simmons et al., 2005; Wilkinson et al., 2013). Another distinctive feature of these deposits is the higher abundance of barite and rhodochrosite, while chalcedony and adularia are relatively more abundant in LS epithermal deposits (Hedenquist et al., 2000; Fig. 2.7). According to John et al. (1999), these are commonly associated with andesite-rhyodacite volcanoes, and have greater depths of formation compared to LS deposits (Simmons et al., 2005). According to general summary of studies conducted by Sillitoe and Hedenquist (2003) and Einaudi at al. (2003), LS deposits have veins and stockworks as mineral styles, silicification and quartz-sericite/illite alteration minerals, ± tetrathedrite ± tennantite ± chalcopyrite ±low Fe sphalerite as sulfidation indicators with Ag-Au-Zn-Pb-Mn ± Cu as typical metal endowments.

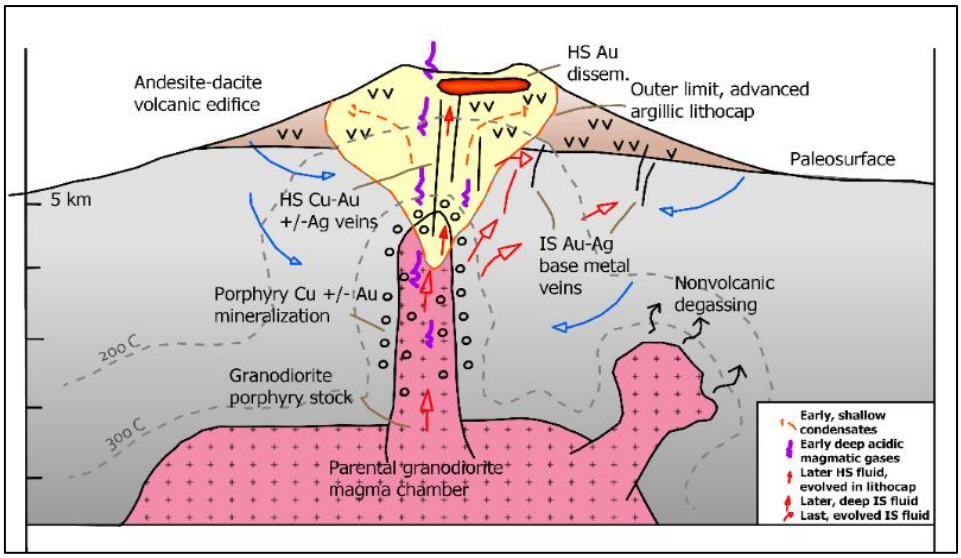

Figure 2.7. Shematic cross-sectional view showing high- and intermediate-sulfidation mineralization at calc-alkaline volcanic arc environment undergoing neutral to mildy extensional tectonism (Sillitoe and Hedenquist, 2003; Taylor, 2007).

2.2 Textural Features of Epithermal Deposits

Epithermal deposits typically form in shallow crustal depths, which undergo brittle deformation. Consequently, most epithermal systems are characterized by distinct open-space filling textures at the macroscopic and microscopic scale. Additionally, quartz and other silica varieties (e.g., chalcedony, cristobalite, opal) are the most abundant gangue minerals in the epithermal environment, with these phases often showing typical textures of epithermal systems. The classification of quartz-dominant ore textures is based on studies conducted since the 1980s (e.g., Sander and Black, 1988; Dong et al. 1995; Moncada et al., 2012). Dong et al. (1995) attempts a genetic sub-division of quartz textures and subdivided them into 3 groups as primary growth textures, recrystallization textures, and replacement textures (Fig. 2.8). Later studies helped improvement and modification of this textural classification of epithermal environments. Also, the textures have been researched in in terms of relations with precious metal concentrations in different deposits (Dowling and Morrison, 1989; Table. 2.4).

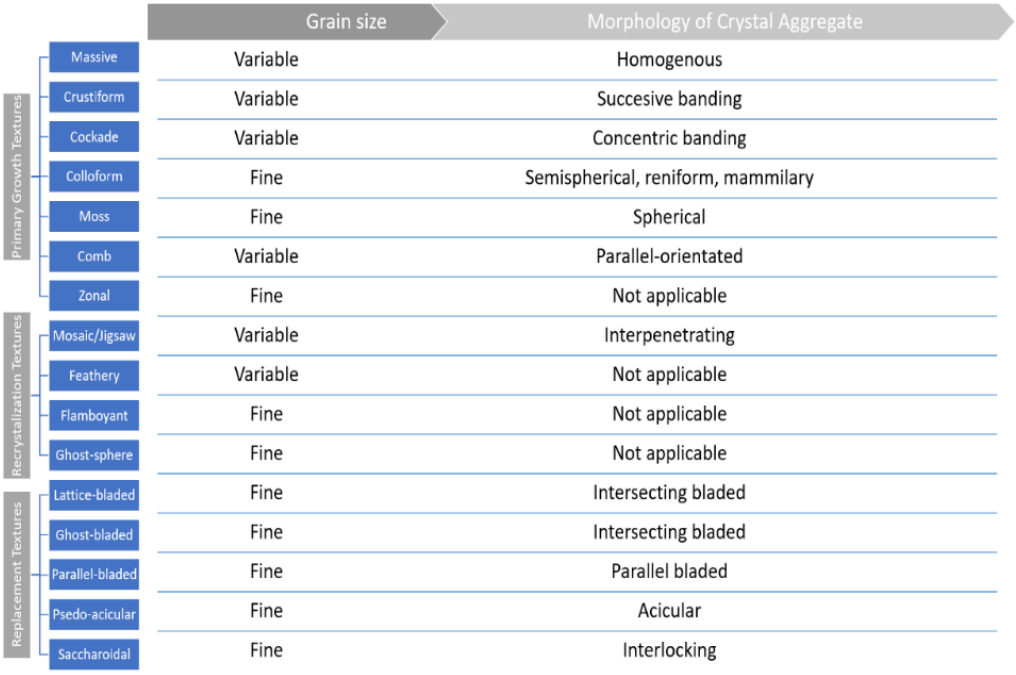

Figure 2.8. Classification board of quartz textures with their grain sized and morphology of crystal aggregates of epithermal veins in Queensland (Dong et al, 1995).

Table 2.4 Quartz texture adundances for Au mineralizing epithermal environments in Queensland (modified from Dowling et al., 1989)

Textural type	**Epithermal Environment**
Comb (coarse)	. .
Comb (medium)	. .
Comb (fine)	. . . .
Banded (crustiform)	. . . .
Banded (colloform)	. . . .
Banded (cockade)	.
Saccharoidal	.
Spider veinlet (comb)	. .
Breccia (infill)	. . . .
Replacement	. . .
". . . ." = dominant variety, ". . ." = abundant variety, ". ." = present, "." = rare)	

Since boiling is one of the most significant processes controlling ore precipitaton and metal tenors, the silica and calcite textures are summarized mainly based on their representations of boiling or non-boiling events. Moncada et al. (2012) summarized the textures of earlier studies considering boiling events, as many subclasses including jigsaw/mosaic, colloform-banded, lattice-bladed calcite with or without replacement by quartz, cockade, and comb quartz (Fig. 2.9). Also, in literature several other textural terms exist such as saccharoidal. Shimizu (2014) expressed that early stages of epithermal ore formation are represented mainly by comb quartz, whereas later stages are represented by comb, microcrystalline and colloform silca textures while fluid conditions were grouped as boiling, gentle boiling and nonboiling in Omu Camp, Hokkaido (Japan).

In the presence of subsequent deformation, however, primary ore textures can be overprinted at both macro- and/or micron-scale by different types of deformational mechanisms (Tobish, 2005).

CHAPTER 3

REGIONAL SETTING, GEOLOGY AND METALLOGENY

3.1 Tectonic Setting of Biga Peninsula

Biga Peninsula in northwestern Turkey constitutes part of a collisional tectonic belt developed following opening and episodic subduction of the Tethyan oceanic basins that once remained between continental fragments derived from Laurasia and Gondwana (Şengör and Yılmaz, 1981; Okay and Tüysüz, 1999). Tectonically, the Biga Peninsula forms part of the Rhodope-Pontide fragment, an approximately 2700-km-long east-west extending continental block constituting the northern Turkish mainland and the southeast Balkans (Fig. 3.1). Rhodope-Pontide fragment is a composite of several smaller fragments including the Rhodope-Strandja Zone, İstanbul Zone and Sakarya Zone (Fig. 3.1; Okay and Tüysüz, 1999, Beccaletto and Jenny, 2004). Although all of these fragments were suggested to have derived from the southern Laurasian margin, these have distinctly different tectonic histories for most of the Paleozoic–Mesozoic (Okay and Tüysüz, 1999; Stampfli, 2000; Moix et al., 2008). By the end of the Mesozoic, these fragments had already been conjoined forming the larger Pontides tectonic entity, when they collided with the southerly Tauride-Anatolide Block to close the intervening Northern Neotethys ocean basin (Stampfli 2000; Stampfli and Borel, 2002; Moix et al., 2008). The İzmir-Ankara-Erzincan Suture Belt represents this collision zone between the Pontides and the Tauride-Anatolide Block and marks the southern margin of the Sakarya Zone (Şengör and Yılmaz, 1981; Okay et al., 1996; Okay and Tüysüz, 1999; Tekin et al., 2002; Çelik et al., 2011).

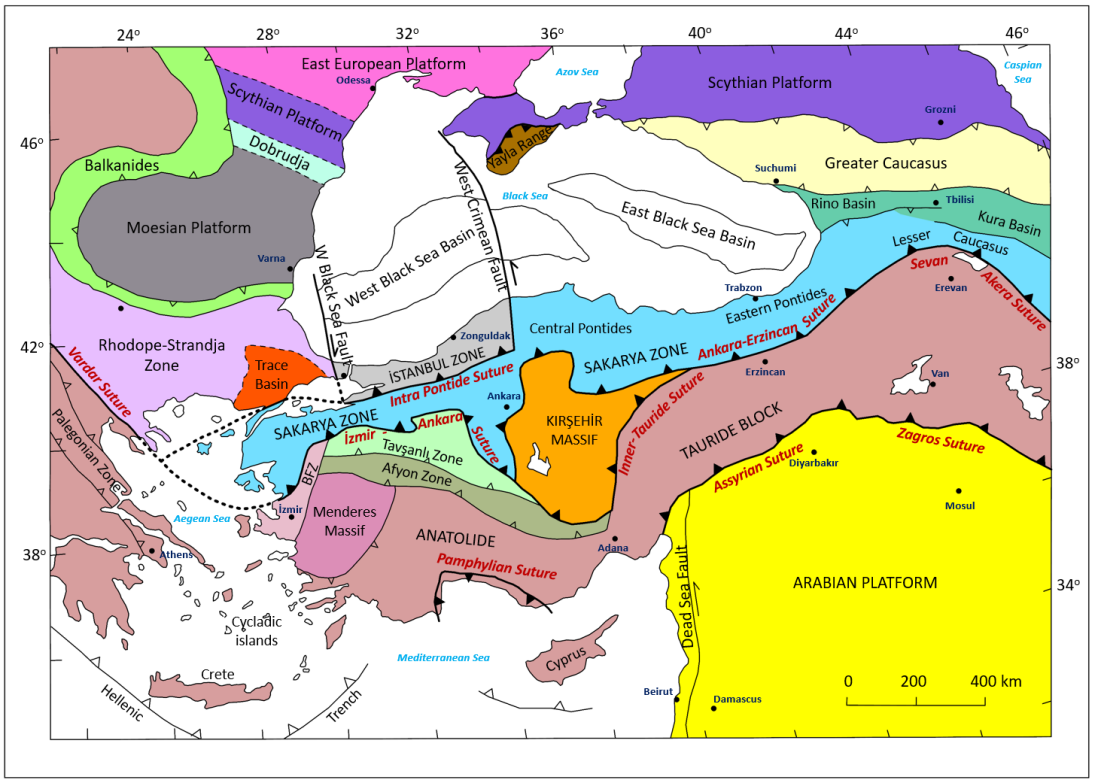

Figure 3.1. Tectonic map of Turkey and its neighboring regions located on Tethyan orogenic belt, showing major stuctures, sutures, and continental blocks including the Rhodope-Strandja Zone, İstanbul Zone and Sakarya Zone (Okay and Tüysüz, 1999).

3.1.1 Tectonic and Structural Evolution of Biga Peninsula

The tectonic evolution of NW Anatolia between the Rhodope-Pontide fragment and the Tauride-Anatolide Block shaped the geology of Biga Peninsula in relation to the opening and closure of Paleotethys and Neotethys oceanic basins. The Paleotethys basin opened between the Hun Supperterrane and northern Gondwana margin during the Late Ordovician–Early Silurian times (Stampfli, 2000; Stampfli and Borel, 2002 Moghadam et al., 2015). Parts of the Pontides (Eastern Pontides, İstanbul, Zonguldak, Sakarya Zones and Karakaya Complex) and Taurides were derived from the initiation of the Paleotethys Ocean at this time (Stampfli and Borel, 2002; Berra and Angiolini, 2014; Moix et al., 2008). Tectonic reconfigurations had continued with Variscan Orogeny, Pangea Formation (collision of Gondwana and Laurasia) and destruction of Paleotethys Ocean following the Late Palezoic period due to

Variscan Orogeny (Stampfli and Borel, 2002; Berra and Angiolini, 2014). Final closure of Paleotethys occurred beginning from the Triassic until the Jurassic with Cimmerian orogenic cycle (Stampfli and Borel, 2002). Contemporaneous with the closure of Paleotethys, Neotethys oceanic basin was started to open from east to west by rifting of Cimmerian continent (including Bolkardağ, Menderes and Geyikdağ) from the northern Gondwana margin around Permian to Early Triassic, with rifting progressed until the earliest Tertiary (Stampfli and Borel, 2012; Moix et al. 2008). Similarly, it is suggested that opening of the Northern Neotethys due to the rifting should have happened during Lower Triassic or earlier (back to as early as the Permian; Sayit et al., 2017; Tekin et al., 2018).

In the Early Jurassic, closure of Paleotethys initiated northward subduction of the Neotethys along the newly accreted margins of Laurasia (including the Pontides) by creating a suture belt (Stampfli and Borel, 2004). The subduction and suturing triggering formation of new oceanic basins like Vardar, İzmir-Ankara-Erzincan and Pindos at around the Late Creataceous (Stampfli and Borel, 2004; Moix et al., 2008). Especially for Biga Peninsula, there are two major tectomagmatic periods, the pre-Cenozoic "amalgamation" and Cenozoic "crustal extension" periods, and as a result of these shortening and extension phases, several major structures subparallel to the neotectonic North Anatolian Fault Zone were formed (Okay et al., 1996; Sanchez et al., 2016).

3.1.1.1 Pre-Cenozoic "Amalgamation" Period

This amalgamation period includes subduction and closure of Paleotethys Ocean from Permian to Middle Triassic, opening of Neotethys Ocean in the Late Permian-Early Triassic, diachronous subduction of the Neotethys under accretionary Laurasian active margin and final closure of the Vardar-Pindos oceans beneath the Rhodope margin and amalgamation of Laurasia and Gondwana (Late Cretaceous) (Moix et al., 2008; Sanchez et al., 2016; Okay et al., 1996; Figs. 3.2). During the Late Cretaceous, calc-alkaline magmatism developed due to northward subduction

of Neotethyan oceanic slab underneath the Pontides (e.g., Okay and Şahintürk, 1997; Okay and Tüysüz, 1999), and crustal thickening and shortening culminated as the Pontide and Anatolide terranes collided to close the Vardar Ocean along the Vardar-İzmir-Ankara Ocean (Northern Neotethys Ocean). Suturing between the Pontides and the Tauride-Anatolide Block was accompanied by obduction of ophiolitic rocks and ophiolitic mélange formation together with nappe emplacement along the Cetmi mélange of the Biga Peninsula (Moix et al. 2008; Sanchez et al., 2016).

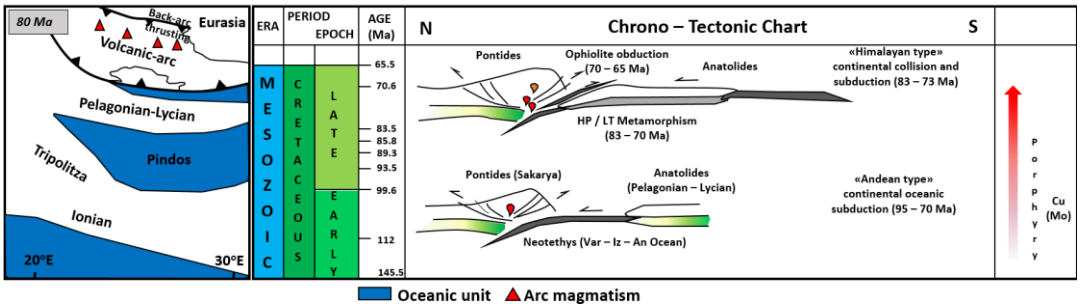

Figure 3.2. Illustration showing pre-Cenozoic amalgamation period between the Pontides and the Tauride-Anatolide Block resulting in continental arc formation, crustal shortening, calc-alkaline magmatism, and associated Cu-Au (Mo) porphyry mineralizations in the Pontides (Ring et al., 2010; Sanchez et al., 2016).

3.1.1.2 Cenozoic "Extension" Period

As post-orogenic extension started in the middle Eocene (*ca.* 45 Ma) in the northwest part of the Aegean, deformation of the Biga Peninsula commenced through extensional faulting, metamorphic core complex exhumation, and graben formation, enhancing magmatism and magmatic-hydrothermal mineralization (Altunkaynak et al., 2012; Sanchez et al., 2016; Brun and Sokoutis, 2010; Figs. 3.3). The major triggering mechanism for such regional-scale extension is suggested to be the gravitational collapse of the thickened crust and/or slab break-off/slab roll-back of the northward subducting African slab due to a decreasing in the subduction rate (Altunkaynak et al., 2012; Sanchez et al., 2016). Therefore, following effects of crustal extension occurred through Cenozoic as summarized by Sanchez et al. (2016) in three distinct periods: (1) post-orogenic regional back-arc extension and basement

exhumation as seen in the Rhodope-Pontide fragment (*ca.* 45 Ma), (2) southward propagation of exhumation towards the Kazdağ (*ca.* 26 Ma) and Menderes Massif (Miocene), and (3) thinning of the western Anatolian and Aegean continental crust, N-directed stretching, and development of basement shear zones resulting in exhumation of metamorphic core complexes and regional extensional fault systems in the Neogene (Fig. 3.3).

Cenozoic magmatism in the Biga Peninsula was derived from extension of syn- and post-orogenic/collisional processes. Cenozoic plutons were emplaced in footwall blocks, while co-magmatic volcanic products were emplaced in extensional basins of hanging-wall blocks (Sanchez et al., 2016).

According to Altunkaynak and Genç (2008), evolution of magma chemistry during the Cenozoic can be described as: (1) calc-alkaline to high-K calc-alkaline magmatism during the middle Eocene–Early Miocene (coincident with slab break-off and resulting astenospheric upwelling causing melting of previously metasomatized mantle lithosphere of previous subduction events), (2) crustally-contaminated shoshonitic magmatism between the Early and Middle Miocene (coincident with the exhumation and uplift of the Kazdağ Metamorphic Massif), and (3) mildly-alkaline to alkaline magmatism between Middle and Late Miocene (Fig. 3.5).

The temporal development of Cenozoic magmatism in Biga Peninsula is shown in Figs. 3.5 and 3.6 and in Table 3.1. There is an overall agreement in southward migration of magmatism over time and an increase in magma alkalinity (Delaloye and Bingöl, 2000; Altunkaynak and Genç, 2008; Dilek and Altunkaynak, 2009; Altunkaynak et al., 2012).

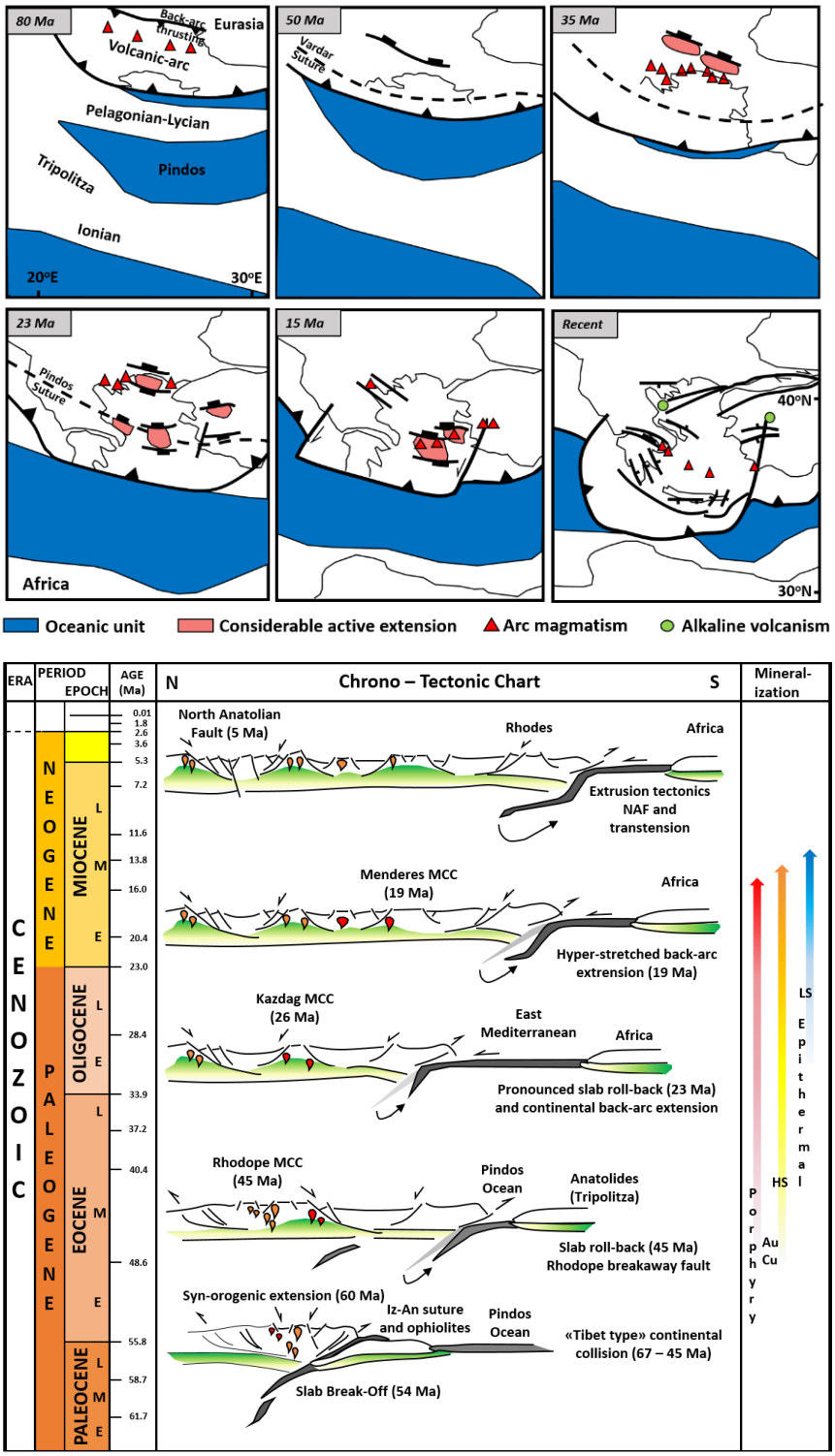

Figure 3.3. Illustration showing Cenozoic extensional period and associated calc-alkaline to alkaline magmatism and related Cu-Au (Mo) porphyry and high sulfidation-epithermal Au mineralizations in the Biga Peninsula (Ring et al., 2010; Sanchez et al., 2016).

3.2 Biga Peninsula Geology

Biga Peninsula is located within the westernmost part of the Sakarya Zone of the Rhodope-Pontide fragment (Beccaletto and Jenny, 2004; Fig. 3.1). Its basement is characterized by Paleozoic metamorphic complexes (e.g., Kazdağ Massif) and metamorphosed products of Paleotethyan subduction-accretion complexes (e.g., Karakaya Complex; Bingöl et al., 1975; Okay et al., 1990). These are overlain by Cretaceous ophiolite blocks and ophiolitic mélange of the Izmir-Ankara-Erzincan Suture Belt (e.g., Çetmi mélange), as well as by Late Mesozoic–Late Cenozoic igneous and sedimentary rocks (Moix et al., 2008). A recent study by Tunç et al., 2012, however, argued that there is no tectonic (Paleo- or Neo-Tethyan) suture between the Sakarya and Rhodope zones. Rather, both were affected by tectono-thermal events during the Variscan Orogeny since the pre-Permian stratigraphy of the northern and southern metamorphic basement units show close similarities (Tunç et al., 2012).

3.2.1 Geological Units of Biga Peninsula

3.2.1.1 Metamorphic Basement and Opholitic Units

Two main NE-trending metamorphic zones were described to occupy the basement of Sakarya and Rhodope-Strandja Zones within the Biga Peninsula. The first metamorphic zone crops out in the southeast, and include the Kazdağ Group and the Karakaya Complex (Fig. 3.4). The second metamorphic assemblage occurs in the northwest, and includes the Ezine Zone and the Çamlıca Metamorphics (Yiğit, 2012; Okay et al., 1990; Beccaletto and Jenny, 2004; Fig. 3.4). The Kazdağ Massif, also referred to as the Kazdağ Group or Kazdağ Metamorphic Core Complex, is composed of Paleozoic meta-ophiolite and gneiss intercalating with marble and amphibolite lithologies (Bingöl et al., 1975; Okay and Satir, 2000a; Bonev and Beccaletto, 2007). The Kazdağ Massif is exposed as a prominent topographic high,

forming the core of an ENE-trending horst block (Sanchez et al., 2016). These high grade metamorphic rocks structurally include high double-plunging anticlinorium or NE-NW-oriented topographic dome resulted from core complex exhumation (Okay and Satir, 2000a; Bonev and Beccaletto, 2007; Yiğit, 2012). Exhumation of the massif led to formation of a couple of opposing detachments during the Early–Middle Miocene (Cavazza et al., 2009).

The Karakaya Complex is composed of strongly deformed and partly metamorphosed Permo–Triassic rocks representing a subduction-accretion complex of the Paleo-Tethys Ocean. It comprises greenschist and blueschist facies metamorphic lithologies in its lower and upper sections, respectively (Okay and Göncüoğlu, 2004). However, Sayıt and Göncüoğlu (2013) proposed that mafic rocks of the Karakaya Complex shares similar style of metamorphism and tectonic setting (Sayıt and Göncüoğlu, 2013). Ezine Zone, formerly known as the Karadağ Unit (Okay et al., 1991), is also named as the Ezine Group and crops out to the west and northwest of Ezine. It consists of Permo–Triassic greenschist facies metasedimentary rocks emplaced northward on top of the Rhodope margin due to compressive regime resulted in opening of the Maliac/Meliata Ocean opening. The Ezine Group is also considered as both eastern and western flanks of Çamlıca and Kemer metamorphics (Beccaletto and Jenny, 2004). It is overlain by the Denizgören ophiolite, which is an amphibolitic metamorphic basement (Beccaletto and Jenny, 2004). Çamlıca Metamorphics and Kemer mica schists, forming parts of the Rhodope metamorphic complex, include Paleozoic metasedimentary rocks outcropping as quartz-mica schists, gneiss with lenses of calc-schist, marble, quartzite, metabasite, slivers of harzburgite and amphibolite (Okay and Satir, 2000b). It constitutes another ENE-trending horst block of metamorphic basement rocks in the Biga Peninsula in addition to the Kazdağ Massif (Sanchez et al., 2016). Previously these units were considered to have formed in response to high-pressure, low-temperature metamorphism (Okay and Satir, 2000b). However, recent studies suggested that Çamlıca metamorphics only experienced medium-grade greenschist facies metamorphism and contains lenses of eclogites and blueschists that recorded

high-grade metamorphism, which were emplaced as tectonic slices following metamorphism of the Çamlıca metamorphic unit (Şengün et al., 2011).

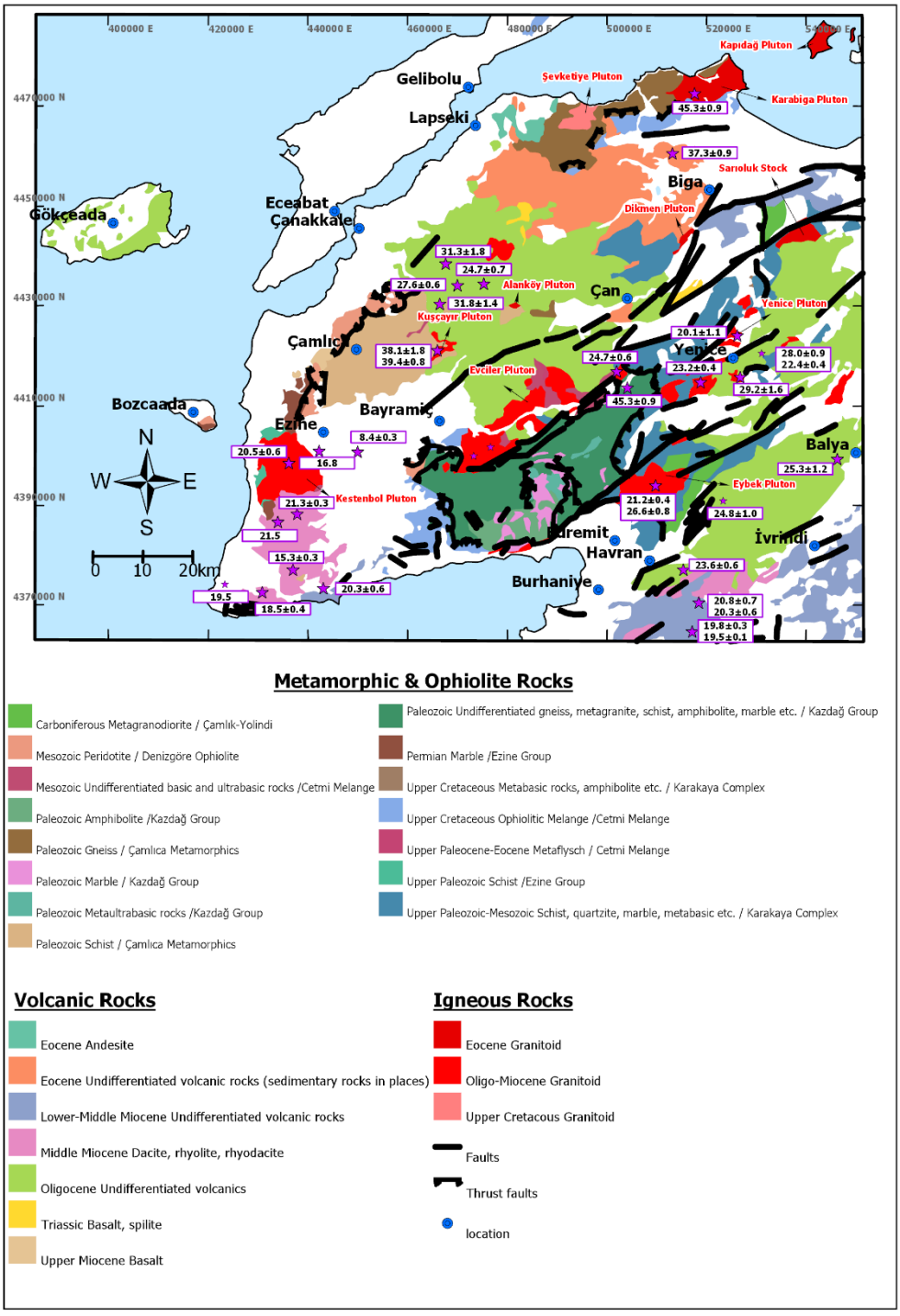

Figure 3.4. Regional geological map of the Biga Peninsula. Age data of some of the igneous centers are also shown (Altunkaynak and Genç, 2008; Yiğit, 2012).

3.2.1.2 Sedimentary Units

Non-metamorphosed sedimentary units of pre-Cenozoic age have limited exposure in the Biga Peninsula, and these are mainly represented by Jurassic platform sequences unconformably overlying the Karakaya Complex, and weakly-deformed pelagic limestones (Fig. 3.4; Dönmez et al., 2005). Cenozoic sedimentary successions, on the other hand, are considerably more widespread, and these were mainly developed in four distinct periods as suggested by Siyako et al. (1989). From oldest to youngest, these periods are: (1) the latest Createcous to early Eocene, (2) middle Eocene to Oligocene, (3) Miocene, and (4) Pliocene to Recent (Fig. 3.5).

Oldest sedimentary units have been rarely exposed throughout the Biga Peninsula. Pre-Cenozoic sedimentary rocks are mainly Jurassic platform sequences, which are unconformably overlying the Karakaya Complex and other basement units, and mainly include sedimentary stratas of unmetamorphosed and weakly-deformed pelagic carbonates (Siyako et al., 1989; Dönmez et al., 2005). According to Okay et al. (2010), the Pre-Cenozoic carbonate-dominated and clastic-calciturbiditic sequences deposited on top of the Çetmi Mélange in Gelibolu and in the Thrace region in the NW Biga Peninsula.

The Middle Miocene to Oligocene sedimentary units are represented by a thick clastic sequence; however, Oligocene sequences have been mostly eroded due to exhumation events during the Late Oligocene (Siyako et al., 1989). Later in the Late Miocene shale, tuff, siltstone, and lignite sequences deposited together with synchronous calc-alkaline volcanism, and by post-volcanic shallow marine sandstones deposited at the post-volcanic stage (Siyako et al., 1989). This clarifies that Oligocene aged volcanic rocks are overlain by Miocene volcanics and intercalations of lacustrine sedimentary rocks and coal (Ercan et al., 1999). Finally, lacustrine carbonates and fluvial sediments including conglomerates, sandstone and shale, deposited as young cover units in the region.

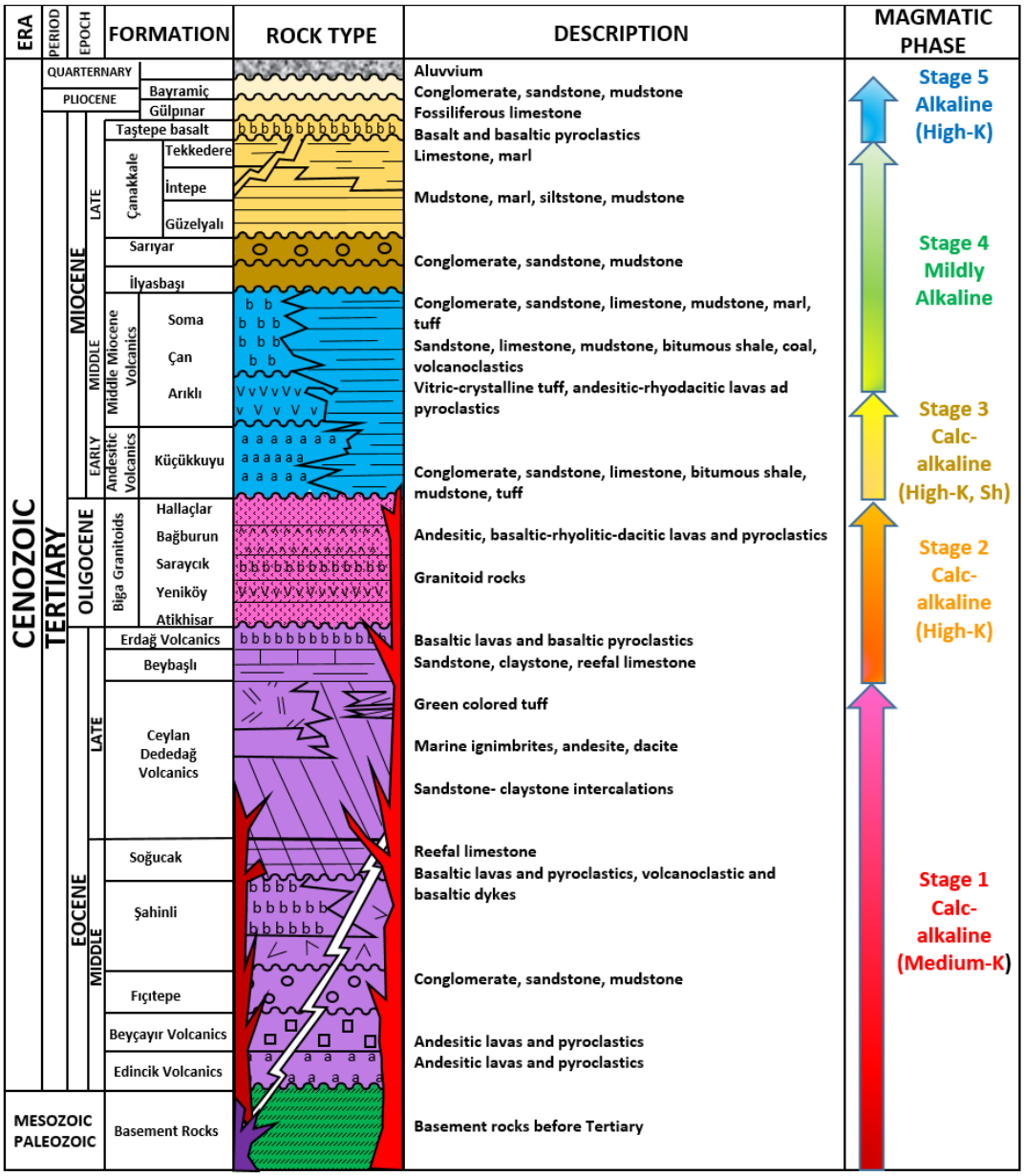

Figure 3.5. Generalized vertical section of the Biga Peninsula (Dönmez et al., 2005; Sanchez et al., 2016; Günaydın, 2017). (Abbreviations: Sh = Shoshonitic)

3.2.1.3 Cenozoic Magmatic Units

In the Biga Peninsula, magmatic rocks of particularly Cenozoic age widely crop out and these are responsible from formation of the majority of regional base and precious metal deposits (Yiğit, 2012; Kuşcu et al., 2013; Smith et al., 2014; Sanchez et al., 2016). Magmatic rocks display a broad range of compositions and geochemical variations among these generally reflect different stages of tectonic evolution (from subduction to post-subduction) and/or deformation cycles (extensional/compressional and strike-slip-dominated) in northwest Anatolia (Brun and Sokotuis, 2007; Sanchez et al., 2016). Sanchez et al. (2016) demonstrated the spatial relationship between plutons and major NNE- and SSE-trending structures based mainly on geomorphology and aeromagnetic data (Fig. 3.6).

Rare Late Cretaceous magmatic products are generally restricted to the north of Biga Peninsula, but these are relatively more common in the Strandja Massif farther north. The Late Cretaceous Şevketiye pluton (71.9±7.8 Ma; Delaloye and Bingöl, 2000) was interpreted to have formed in a continental arc setting during northward subduction of the Northern Neotethys Ocean (Karacık et al., 2008; Stampfli and Borel, 2004).

Following the collision between the Rhodope-Pontide fragment and the Tauride-Anatolide Block by the end of the Cretaceous, post-subduction magmatism in the Biga Peninsula commenced in the middle Eocene (~50 Ma) and continued at least until the Early Miocene (~20 Ma). Detailed information for Cenozoic magmatism in Biga Peninsula can be summarized as below;

- Middle to late Eocene magmatic units dominate the northern Biga Peninsula. Magmatic products of this stage crop out as Dikmen (51.9±1.9 Ma; Yiğit, 2012) and Karabiga (52.7±1.9 Ma to 45.3±0.9 Ma; Delaloye and Bingöl, 2000; Beccaletto et al., 2007), Kapıdağ (42.2±1.0 Ma to 36.1±0.8 Ma; Delaloye and Bingöl, 2000) plutons. Eocene plutonism was accompanied by synchronous volcanism including Edincik-Beyçayır Volcanics, Şahinli-

Fıçıtepe-Soğucak-Ceylan Formations, Ceylan-Erdağ Volcanics and Beybaşlı Formation constitute andesitic-rhyolitic-basaltic lavas, pyroclastics and volcanoclastics intercalating with clastics, turbidites, coal units and limestone sequences (Dönmez et al., 2005).

- Central parts of the Biga Peninsulla comprise Oligocene–Miocene magmatic units, which are represented by Yenice (29.2±1.6 Ma to 20.7±1.1 Ma; Delaloye and Bingöl, 2000), Eybek (26.6±0.8 Ma to 21.1±0.4 Ma; Delaloye and Bingöl, 2000; Altunkaynak and Genç, 2008), Evciler (28.0±0.1 Ma to 24.8±0.1 Ma; Altunkaynak and Genç, 2008), Kestenbol (22.8±0.2 Ma to 22.3±0.2 Ma; Altunkaynak and Genç, 2008) and Alanköy (32.7±0.7 Ma; Yiğit, 2012) plutons. Oligocene to Miocene plutonism was also accompanied by synchronous volcanism including Saraycık-Hallaçlar-Yeniköy-Atikhisar-Behramkale Volcanics, Bağburun Formation and Yürekli dacite constitutes andesitic-basaltic-rhyolitic-dacitic lavas and pyroclastics (Dönmez et al., 2005)
- As a product of Early Miocene plutonism in Biga, Kozak Pluton (37.6±3.3 Ma to 19.6±0.4 Ma; Delaloye and Bingöl, 2000) is shown at southern part of Biga Peninsula (Figs. 3.4 and 3.6). Miocene plutonism was also accompanied by synchronous volcanism constituting Hüseyinfakı-Ayvacık Volcanics, Babadere Dacite, Işıkeli Rhyolite, Çambalak Ignimbrite and Çanakkale formation including basaltic-andesitic ignimbrites-tuffs-rhyolites, alkaline and basaltic lavas and pyroclastics intercalating with lacustrine-shallow marine sedimentary lithologies and continental clastics (Dönmez et al., 2005).

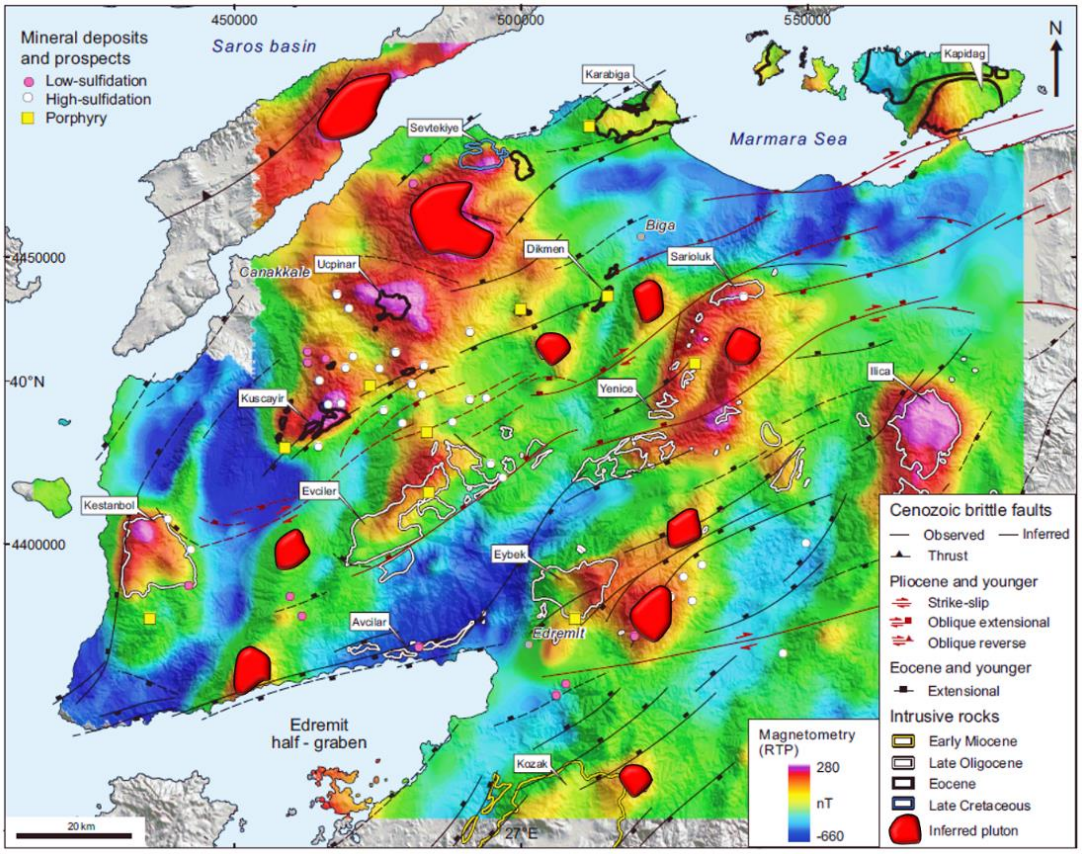

Figure 3.6. Regional aeromagnetic map showing outcropping and inferred concealed plutonic systems in the Biga Peninsula (Sanchez et al., 2016).

Table 3.1 Geochronological data from intermediate to intermediate to felsic plutonic rocks of Biga Peninsula.

Pluton	Mineral	Method	Age (Ma)	Epoch	*Reference*
Şevketiye E	Muscovite	K-Ar	71.9±1.8	Late Cretaceous	*Delaloye and Bingöl, 2000*
Kapıdağ N	Biotite	K-Ar	39.9 ±0.8	Eocene	*Delaloye and Bingöl, 2000*
	Hornblende	K-Ar	42.2 ±1.0	Eocene	*Delaloye and Bingöl, 2000*
	Biotite	K-Ar	38.3 ±0.8	Eocene	*Delaloye and Bingöl, 2000*
Kapıdağ S	Biotite	K-Ar	38.2±0.8	Eocene	*Delaloye and Bingöl, 2000*
	Biotite	K-Ar	36.1±0.8	Eocene	*Delaloye and Bingöl, 2000*
Karabiga	Biotite	K-Ar	45.3±0.9	Eocene	*Delaloye and Bingöl, 2000*
	Xenotime	U-Pb	52.7±.1.9	Eocene	*Beccaletto et al., 2007*
Kozak	Orthoclase	K-Ar	37.6±3.3	Eocene	*Delaloye and Bingöl, 2000*
	Orthoclase	K-Ar	24.2±1.1	Oligocene	*Delaloye and Bingöl, 2000*
	Biotite	K-Ar	23.3±0.5	Oligocene	*Delaloye and Bingöl, 2000*
	Hornblende	K-Ar	21.9±0.5	Miocene	*Delaloye and Bingöl, 2000*
	Biotite	K-Ar	19.6±0.4	Miocene	*Delaloye and Bingöl, 2000*
	Biotite	K-Ar	22.1±0.4	Miocene	*Delaloye and Bingöl, 2000*
	Hornblende	K-Ar	25.7±0.5	Oligocene	*Delaloye and Bingöl, 2000*
Kuşçayır	Hornblende	K-Ar	38.1±1.8	Eocene	*Delaloye and Bingöl, 2000*
	Hornblende	K-Ar	35.7±0.8	Eocene	*Delaloye and Bingöl, 2000*
	Hornblende	K-Ar	39.4±0.8	Eocene	*Delaloye and Bingöl, 2000*
	Zircon	U-Pb	41.1±0.52	Eocene	*Smith et al., 2016*
Eybek	Biotite	K-Ar	26.6±0.8	Oligocene	*Delaloye and Bingöl, 2000*
	Biotite	K-Ar	21.1±0.4	Oligocene	*Delaloye and Bingöl, 2000*
	Hornblende	K-Ar	21.2±0.6	Oligocene	*Delaloye and Bingöl, 2000*
	Biotite	K-Ar	24.1±0.5	Oligocene	*Delaloye and Bingöl, 2000*
	Hornblende	K-Ar	23.9±0.5	Oligocene	*Delaloye and Bingöl, 2000*

Pluton	Mineral	Method	Age (Ma)	Epoch	*Reference*
	Zircon	U-Pb	23.94±0.31	Oligocene	*Altunkaynak and Genç, 2008*
Evciler	Hornblende	Ar-Ar	28.0±0.1	Oligocene	*Altunkaynak and Genç, 2008*
	Hornblende	Ar-Ar	27.7±0.1	Oligocene	*Altunkaynak and Genç, 2008*
	Biotite	Ar-Ar	24.8±0.1	Oligocene	*Altunkaynak and Genç, 2008*
	Biotite	Ar-Ar	24.8±0.1	Oligocene	*Altunkaynak and Genç, 2008*
Kestenbol	Hornblende	Ar-Ar	22.8±0.2	Miocene	*Altunkaynak and Genç, 2008*
	Biotite	Ar-Ar	22.3±0.2	Miocene	*Altunkaynak and Genç, 2008*
Yenice E	Biotite	K-Ar	29.2±1.6	Oligocene	*Delaloye and Bingöl, 2000*
	Biotite	K-Ar	23.5±0.6	Oligocene	*Delaloye and Bingöl, 2000*
	Biotite	K-Ar	24.8±0.6	Oligocene	*Delaloye and Bingöl, 2000*
Yenice N	Biotite	K-Ar	22.6±0.5	Miocene	*Delaloye and Bingöl, 2000*
	Hornblende	K-Ar	20.1±1.1	Miocene	*Delaloye and Bingöl, 2000*
Yenice S	Biotite	K-Ar	22.0±0.5	Miocene	*Delaloye and Bingöl, 2000*
	Biotite	K-Ar	23.2±0.4	Oligo-Miocene	*Delaloye and Bingöl, 2000*
	Biotite	K-Ar	24.5±0.5	Oligocene	*Delaloye and Bingöl, 2000*
	Chlorite	K-Ar	20.9±0.5	Miocene	*Delaloye and Bingöl, 2000*
	Hornblende	K-Ar	47.6±1.4	Eocene	*Delaloye and Bingöl, 2000*
Alanköy	Hornblende	K-Ar	32.7±0.7	Oligocene	*Yiğit, 2012*

3.3 Metallogeny of the Biga Peninsula

The Tethyan-Eurasian Metallogenic Belt is one of the world's richest mineral belts and hosts numerous metallic deposits that formed during opening and closure of different Tethyan oceanic basins (Jankovic, 1977; von Quadt et al., 2005; Hou et al., 2007; Yiğit, 2009; Richards, 2014; Moritz et al, 2016). Deposits along this belt, also including Turkey, usually occur in clusters that define various mineral provinces, subprovinces, and districts. The Biga Peninsula is one of the most significant sub-provinces and comprises a large number of small- to large-sized base and precious metal deposits as well as numerous prospects (Fig. 3.7). As indicated previously, these mineral systems are related with certain tectonomagmatic phases that mainly developed during Cenozoic syn- and post-orogenic extension and resulting magmatism in northwest Turkey (Brun and Sokotuis, 2007; Sanchez et al., 2016).

Cenozoic ore deposits in Biga Peninsula are generally magmatic-hydrothermal in origin and mineralization styles vary from intrusion-related porphyry Cu±Au±Mo and skarn/carbonate-replacement Pb-Zn±Au±Ag deposits to epithermal Au–Ag±Cu±Pb±Zn deposits (Fig. 3.7). Two productive magmatic periods were identified during the middle Eocene (~45 Ma: between 52 - 36 Ma) and in the late Oligocene (~30 Ma: between 33 - 24 Ma) that sourced majority of the economic deposits mainly including porphyry Cu-Au and epithermal Au-Ag±Cu systems (Yiğit, 2012; ; Leroux, 2016; Smith et al, 2016; Kuşcu et al., 2019).

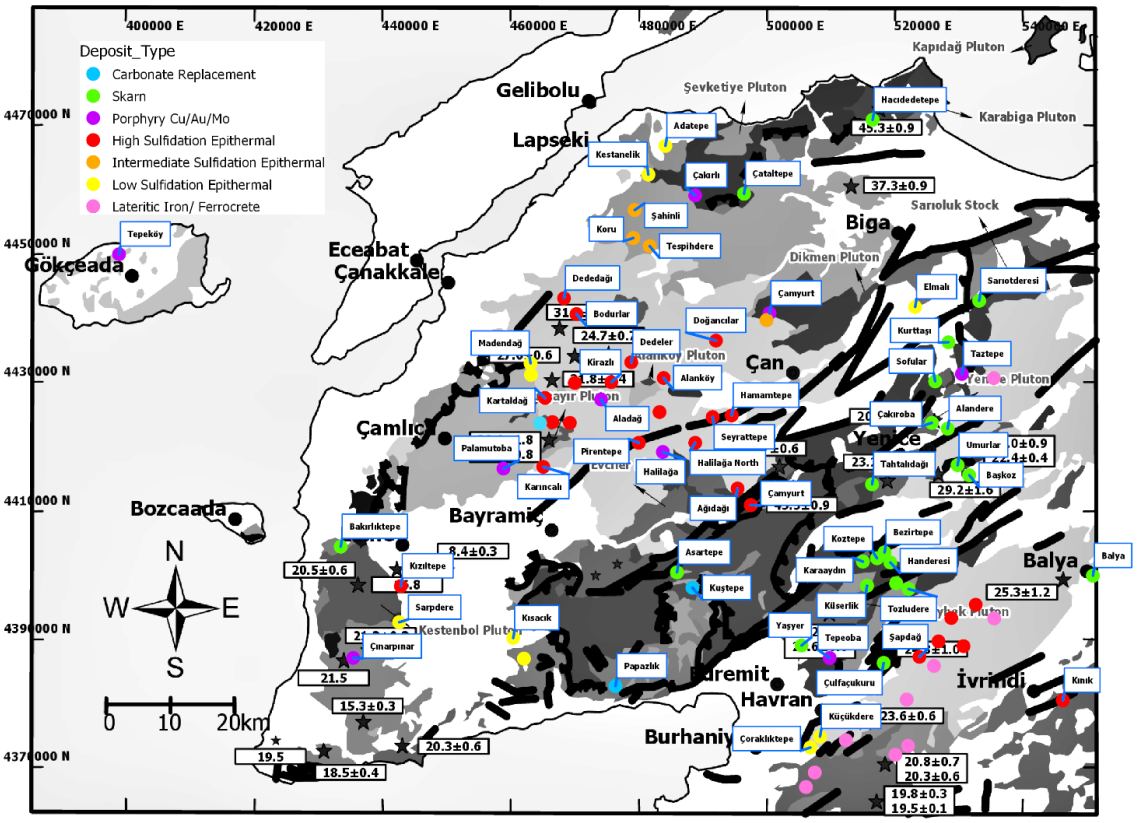

Figure 3.7. Distribution of major magmatic-hydrothermal deposits and prospects in Biga Peninsula (adapted from Yiğit 2012)

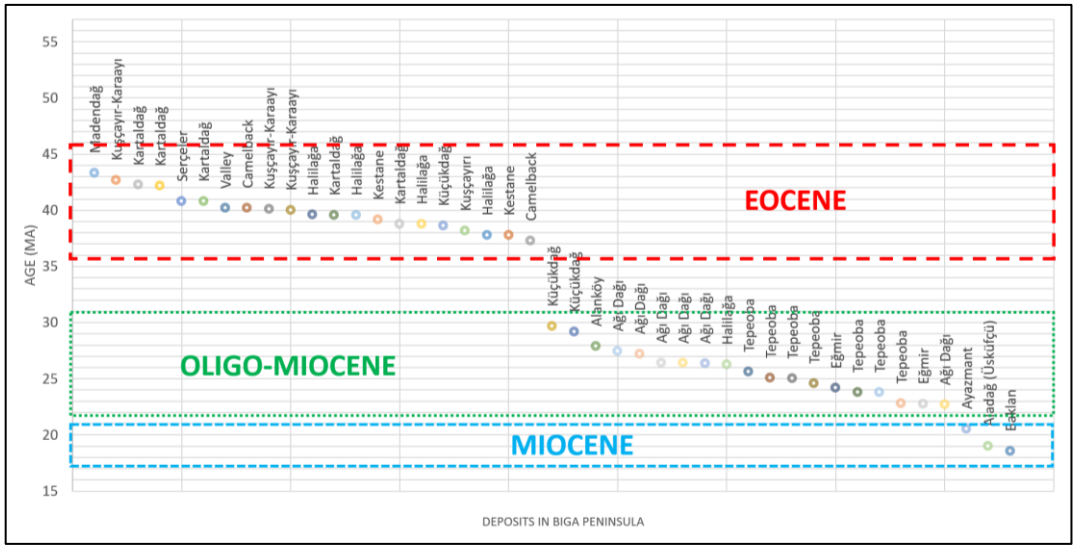

Figure 3.8. Age distribution of some important mineral deposits/prospects of the Biga Peninsula. Data sources provided in Table 3.2.

3.3.1 Epithermal deposits of the Biga Peninsula

Epithermal deposits in Biga Peninsula are concentrated mostly in the Oligocene (e.g. Küçükdağ and Ağı Dağı); however, some of the important epithermal systems were formed during the Eocene (e.g., Lapseki, Kartaldağ, and Madendağ; Yiğit, 2012; Ünal-İmer et al., 2013). Most of the regionally-significant epithermal deposits are located within the central part of the Biga Peninsula (e.g., Kirazlı and Halilağa North), whereas several systems occur in the north (e.g., Lapseki Au, Tespihdere, Şahinli Au-Ag/Karatepe and Sırakayalar) and in the south (e.g., Küçükdere and Kısacık) of Biga Peninsula (Yiğit, 2012).

Lapseki Au deposit is one of the significant low-sulfidation Au epithermal deposits located in NW Biga Peninsula. Mineralization at Lapseki is associated with quartz veins up to about 14 meters thick, outcropping in a 2 km^2 area, and hosted by Paleozoic mica schist and Eocene andesitic subvolcanics (Gülyüz et al., 2018 and 2020). According to Sanchez et al. (2016), the deposit formed during the early stages of extensional tectonics, under a tectonic regime that possibly contributed to structural permeability and vein formation. Gülyüz et al. (2018) demonstrated that co-seismic rupturing and fracturing enhanced permeability, resulting in the formation of E–W-trending veins along lateral faults and extensional fractures, and along NE-SW-trending veins together with cataclastic and chaotic breccias of vein infill. Sheeted quartz veins in the mineralized area (the Topyurt, K3, K2, K1, KK1, KK2, KK3, KK4, and Karatepe veins) display typical colloform, comb to cockade, crustiform, pseudobladed, and saccharoidal quartz textures as filling or replacement textural categories (Gülyüz et al., 2020).

Two adjacent epithermal systems, the Madendağ LS and Kartaldağ HS epithermal systems, are hosted in middle Eocene dacite porphyry and Paleozoic mica schists, respectively (Ünal-İmer et al., 2013). Ünal-İmer et al. (2013) indicated that Kartaldağ deposit has a core of quartz-pyrite zone covered by a quartz-alunite-pyrophyllite zone together with chlorite/smectite-illite±kaolinite marginal alteration, whereas Madendağ deposit represents more limited host rock alteration as sericite-

illite-kaolinite and quartz-pyrite. According to this study, Madendağ deposit is characterized by quartz textures typical of LS epithermal systems such as colloform, comb, and banded quartz veins. A temporal and spatial relationship between these two distinct mineralization systems have been proposed by Unal-Imer et al(2013) based on overlapping $^{40}Ar/^{39}Ar$ ages of hornblende from Kartaldağ deposit (42.19±0.45 Ma and 40.80±0.36 Ma) and hydrothermal K-feldspar from Madendağ (43.34±0.85 Ma; Ünal-İmer et al., 2013).

Şahinli, Tespihdere and Koru deposits are considered as intermediate-sulfidation epithermal Au-base metal deposits (Yılmaz et al., 2010; Yiğit, 2012). Şahinli is hosted by andesitic and dacitic volcanic rocks of possible Eocene age, which have been intruded by andesite porphyry. Mineralization is characterized by quartz veins containing stockwork and breccia zones, and silicification and argillic alteration with assemblages of illite/muscovite and illite/smectite are related with base and precious metals. Advanced argillic alteration is probably barren (Yılmaz et al., 2010). Tesbihdere is an intermediate-sulfidation epithermal system with Cu-Pb-Zn-Ag-Au mineralization, and the host rocks are rhyolitic and dacitic pyroclastic rocks (Oligocene calc-alkaline rocks as studied by Çiçek and Oyman, 2016) (Bozkaya et al., 2014). The vein and stockwork stye mineralization, and also exhibits brecciated matrix. Tesbihdere has extensive and widespread argillic alteration with presence of quartz, kaolinite, illite-smectite and alunite, in addition to silicic and sericitic alterations. Main gangue minerals are calcite, quartz and barite, and sulfide minerals are primary chalcopyrite, galena and pyrite, sphalerite with less amounts tetrahedrite, chalcocite, covellite, goethite, digenite (Bozkaya et al., 2014). Koru Pb-Zn-Ag-Au deposit has different mineralization zones as Eskikışla and Tahtalıkuyu with many small zones (Çiçek and Oyman, 2016). It is hosted by Oligocene aged calcalkaline rocks, and it is associated with veins, stockworks, breccias with sphalerite, galena, pyrite and chalcopyrite accompanying quartz, barite and calcite (Çiçek and Oyman, 2016).

Küçükdağ Au-Ag deposit is located at the NE of the TV Tower property, and it is a high-sulfidation epithermal system containing Au-Ag-Cu (Au and Cu is overlain by

Ag-blanket; Smith et al., 2014). Gold mineralization is hosted by a massive lithic lapilli-bearing tuff unit and silver mineralization is constrained to an overlying lacustrine sequence capped by andesite breccias; also, copper is distributed throughout the gold and silver zones (Smith et al., 2014). Mineralization is primarily located in the hanging-wall block of a N-dipping extensional fault, and the footwall block is almost barren (Smith et al., 2014). Also, Cu and Au mineralization is focused in and around hydrothermal breaccia pipe which is controlled by NE-NW trending structures (Sanchez et al., 2016). Au mineralization is related with both tectonic and hydrothermal breccias, vuggy quartz and veins. Alteration minerals are mainly alunite and dickite, and the sulfide minerals are pyrite, enargite, covellite, silver minerals, Te-mineral and native gold. Ag mineralization is associated by silicification, very fine grained pyrite, marcasite and enargite (Smith et al., 2014).

3.3.2 Porphyry Deposits in Biga Peninsula

Porphyry deposits in Biga Peninsula, some of them can be temporally and spatially associated with HS epithermal deposits (e.g. Halilağa District including Ağı Dağı), are economically very important and this makes them very appealing (Yiğit, 2012; Kuşcu et al., 2019). Porphyry systems are generally restricted by ENE-E trending normal faults (formed due to crustal extension in Cenozoic), and the faults stand as controlling factor for emplacement of porphyry deposits is Biga Peninsula (Sanchez et al., 2016; Kuşçu et al., 2019). As with the timing of magmatism in the Biga Peninsula, ages of regional porphyry systems also get younger from north towards south (e.g. Halilağa, Tepeoba and Baklan; Table. 3.2).

The Halilağa property includes some major structures that are related to and part of North Anatolian Fault Zone. These are controlled by ENE-WSW transtension faults; however, local transpressional faultings in the area result in local exhumation of the Kestane porphyry and older lithologies and series of ENE-trending horst and grabens (Cunningham-Dunlop, 2011). In other words, there are two normal faults at south and north of the Kestane porphyry with almost E-W trending. Kestane porphyry is

located between Künk lithocap to south and Pirentepe lithocap to the northwest (Sanchez et al., 2016). Mineralization is hosted by Oligocene aged quartz-feldspar-hornblende porphyry rocks, andesitic flows and tuffs (Yiğit, 2012). A 4 km X 2 km alteration zone was developed in relation to the porphyry system. It is affected by strong potassic alteration with highest Au and Cu grades associated with early biotite, chalcopyrite, magnetite and quartz veining. Potassic alteration is overprinted by weaker phyllic alteration consisting sericite, pyrite and quarz, and phyllic alteration is commonly overprinted by supergene argillic alteration at Künk Tepe with kaolin and smectites of altered feldspar and silica replaced by groundmass (Cunningham-Dunlop, 2011). Mineralization contains mainly pyrite, chalcopyrite and magnetite with some minor chalcocite, molybdenite and visible disseminated Cu. Moreover, mineralization of the porphyry is related with majority of stockwork veins, disseminations and quartz veins as ore textures (Yiğit, 2012). Most quartz veins are B-type and D-type, and A-type veinlets are rare in the outcrop (Cunningham-Dunlop, 2011). The age of Kestane porphyry mineralization is 39.56±0.21 Ma (Eocene) according to Re-Os dating of molybdenite in the quartz veins (Brunetti et al., 2016).

Table 3.2 Geochronological data of major porphyry and epithermal deposits and/or prospsects, NW of Turkey (in Biga Peninsula)

Name	Mineralization Style	Method	Mineral	Age (Ma)	Error (Ma)	Reference
Madendağ	Low/Intermediate-sulfidation epithermal	Ar-Ar	K-feldspar	43.34	0.85	Ünal-İmer et al., 2013
Kuşçayır-Karaayı	Porphyry	Ar-Ar	Biotite	42.68	0.25	Kuşcu et al., 2019
Kartaldağ	High-sulfidation epithermal	Ar-Ar	Biotite	42.27	0.96	Ünal, 2010; Ünal-İmer et al., 2013
Kartaldağ	High-sulfidation epithermal	Ar-Ar	Biotite	42.19	0.45	Ünal, 2010; Ünal-İmer et al., 2013
Serçeler	High-sulfidation epithermal	Ar-Ar	Hornblende	40.8	0.36	Kuşcu et al., 2019
Kartaldağ	High-sulfidation epithermal	Ar-Ar	Hornblende	40.8	0.36	Ünal-İmer et al., 2013

Name	Mineralization Style	Method	Mineral	Age (Ma)	Error (Ma)	Reference
Valley	Porphyry	U-Pb	Zircon	40.2	0.37	Brunetti, 2016
Camelback	Porphyry	U-Pb	Zircon	40.2	0.34	Brunetti, 2016
Kuşçayır-Karaayı	Porphyry	Ar-Ar	Hornblende	40.11	0.28	Kuşcu et al., 2019
Kuşçayır-Karaayı	Porphyry	Ar-Ar	Sericite	39.99	0.27	Kuşcu et al., 2019
Halilağa	Porphyry	Re-Os	Molybdenite	39.6	0.21	Brunetti, 2016
Kartaldağ	High-sulfidation epithermal	Ar-Ar	Sericite	39.57	0.47	Ünal, 2010
Halilağa	Porphyry	Re-Os	Molybdenite	39.56	0.21	Brunetti, 2016
Kestane	Porphyry	U-Pb	Zircon	39.19	0.47	Brunetti, 2016
Kartaldağ	High-sulfidation epithermal	Ar-Ar	Alunite, trace of quartz	38.8	0.7	Yiğit, 2012
Halilağa	Porphyry	U-Pb	Zircon	38.8	0.3	Brunetti, 2016
Küçükdağ	High-sulfidation epithermal	U-Pb	Zircon	38.62	0.45	Brunetti, 2016
Kuşçayırı	Porphyry	Ar-Ar	~50% alunite, ~50% quartz + goethite	38.2	0.5	Yiğit, 2012
Halilağa	Porphyry	U-Pb	Zircon	37.8	0.36	Brunetti, 2016
Kestane	Porphyry	U-Pb	Zircon	37.79	0.36	Brunetti, 2016
Camelback	Porphyry	U-Pb	Zircon	37.3	0.89	Brunetti, 2016
Küçükdağ	High-sulfidation epithermal	Ar-Ar	Alunite	29.7	0.42	Brunetti, 2016
Küçükdağ	High-sulfidation epithermal	Ar-Ar	Alunite	29.2	0.33	Brunetti, 2016
Alanköy	High-sulfidation epithermal and Porphyry	Ar-Ar	~50% alunite, ~50% quartz + goethite	27.9	0.2	Yiğit, 2012
Ağı Dağı	High-sulfidation epithermal	Ar-Ar	Sericite	27.48	0.34	Kuşcu et al., 2019
Ağı Dağı	High-sulfidation epithermal	Ar-Ar	Biotite	27.2	0.18	Kuşcu et al., 2019

Name	Mineralization Style	Method	Mineral	Age (Ma)	Error (Ma)	Reference
Ağı Dağı	High-sulfidation epithermal	Ar-Ar	Biotite	26.42	0.15	Kuşcu et al., 2019
Ağı Dağı	High-sulfidation epithermal	Ar-Ar	~70% alunite, ~30% quartz	26.4	0.3	Yiğit, 2012
Ağı Dağı	High-sulfidation epithermal	Ar-Ar	Sericite	26.36	0.16	Kuşcu et al., 2019
Halilağa	Porphyry	Ar-Ar	Sericite	26.27	0.19	Kuşcu et al., 2019
Tepeoba	Porphyry	Re-Os	Molybdenite	25.62	0.09	Murakami et al., 2005
Tepeoba	Porphyry	Re-Os	Molybdenite	25.11	0.14	Murakami et al., 2005
Tepeoba	Porphyry	Re-Os	Molybdenite	25.03	0.14	Murakami et al., 2005
Tepeoba	Porphyry	Ar-Ar	Muscovite	24.6	1.4	Murakami et al., 2005
Eğmir	High-sulfidation epithermal and Porphyry	Ar-Ar	Biotite	24.18	0.21	Kuşcu et al., 2019
Tepeoba	Porphyry	Ar-Ar	Phologopite	23.8	1.2	Murakami et al., 2005
Tepeoba	Porphyry	Ar-Ar	Phologopite	23.8	1.4	Murakami et al., 2005
Tepeoba	Porphyry	Ar-Ar	Muscovite	22.8	1.4	Murakami et al., 2005
Eğmir	High-sulfidation epithermal and Porphyry	Ar-Ar	Sericite	22.77	0.16	Kuşcu et al., 2019
Ağı Dağı	High-sulfidation epithermal	Ar-Ar	Biotite	22.7	1	Kuşcu et al., 2019
Ayazmant	Skarn	Ar-Ar	Hornblende	20.55	0.33	Kuşcu et al., 2019
Aladağ (Üsküfçü)	Porphyry, Skarn	Ar-Ar	Hornblende	19	1	Kuşcu et al., 2019
Baklan	Porphyry	Ar-Ar	Biotite	18.56	0.11	Kuşcu et al., 2019

CHAPTER 4

GEOLOGY OF ŞAHİNLİ (SIRAKAYALAR AND KARATEPE) LOW SULFIDATION EPITHERMAL AU-AG DEPOSIT

The Sırakayalar and Karatepe Au-Ag deposits are located in Lapseki area (Çanakkale) within NW Biga Peninsula, about 4 km NE of the town of Şahinli (Fig. 1.1). Gold-silver mineralization in the study area occurs mainly within quartz veins in two separate zones, the Karatepe Sector and the Sırakayalar Sector (Fig. 4.1). These mineralized zones occupy the western and eastern flanks of a NW-trending steeply-incised valley, respectively. A third zone (named as Kovanlik; Fig. 4.1) situated immediately to the west of the Karatepe vein system lies along the border with the adjacent Lapseki gold mine, and was therefore not included in this study.

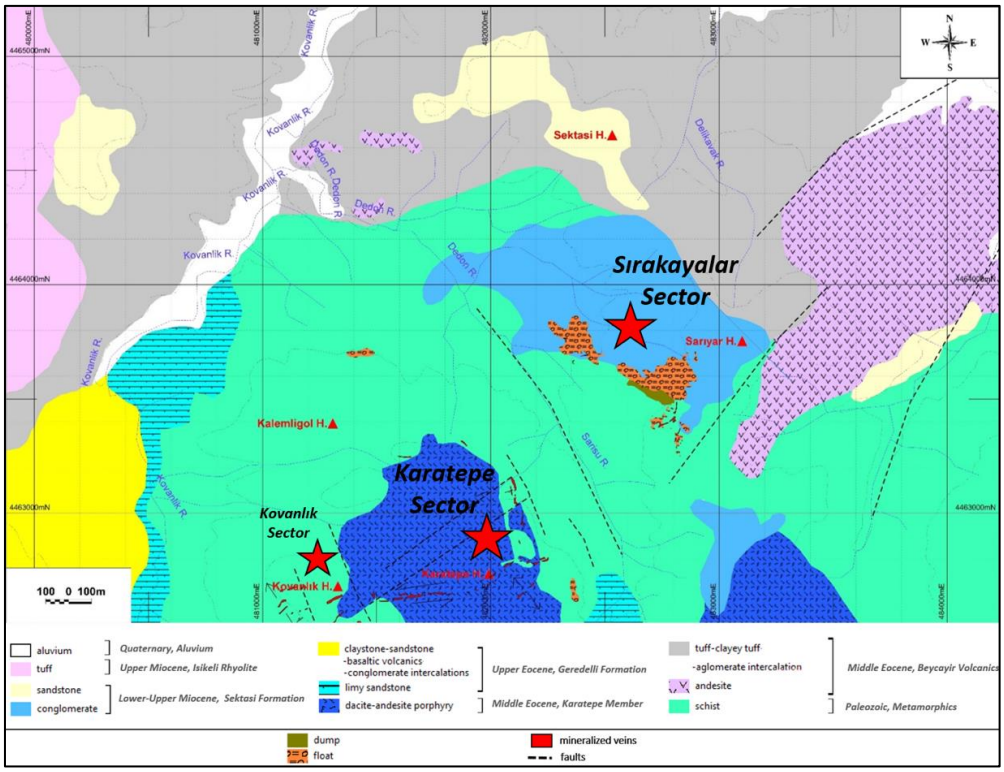

Figure 4.1. Geological map of the study area showing major lithological units, NW-SE and NE-SW probable faults seen as dashed lines (modified from original map prepared by ESAN geologists based on earlier work by MTA; southern part of the map modified using information from Gülyüz, 2017).

A large portion of the study area is covered by dense vegetation, hampering detailed surface mapping, particularly in the Karatepe Sector in the west. Here, rock exposures are generally limited to drill roads, whereas in the Sırakayalar Sector basement rocks crop out to the east of the mineralized area. Descriptions of major lithologies and structures provided below are therefore largely based on drill hole data combined with surface geological data obtained during company mapping.

Figure 4.2. General view of mineralized zones in the study area. a) View of Karatepe and Sırakayalar mineralized zones/sectors, b) View of the Karatepe Sector from Sırakayalar Sector. Karatepe Hill comprises schists of the Çamlıca Metamorphics and cross-cutting dacite porphyry, both cross-cut by mineralized quartz veins. c) Oxidized float material (red) characterizing the shallow levels of the Sırakayalar Sector. The float material contains broken vein fragments and overlies schists of the Çamlıca Metamorphics.

4.1 Lithological Units

Graphitic mica schists of the Çamlıca metamorphics (Okay and Satır, 2000b) constitute the local basement in the study area. This unit is widely exposed in the Karatepe Sector in the west, whereas in the Sırakayalar Sector it is partly covered by talus material (Figs. 4.1 and 4.2). Mica schists are highly deformed both in the outcrop and also in drill core. These are characterized by a mineral assemblage of quartz, muscovite, biotite, and graphite with lesser pyrite. The mica schists are suggested to have derived from the Rhodope Massif in the north (Okay and Satır, 2000b). Although its exact age is unknown, phengite Rb-Sr ages of ~69 Ma (Okay and Satır, 2000b) indicate that the Çamlıca Metamorphics have undergone peak regional metamorphism at the end of the Cretaceous.

In the Karatepe Sector, mica schists have been cross-cut by a moderately- to strongly-altered porphyritic unit called as the Karatepe Member (Fig. 4.1), which regionally correlates with the Eocene Beyçayır volcanics and other olcanic units in the Lapseki area (42–38 Ma; Altunkaynak and Genç, 2008; Erenoğlu et al., 2022). This unit, likely representing a sub-volcanic stock, is intensely-altered but the original igneous textures as well as some of the primary mineral phases are locally preserved. Due to significant alteration, an attempt was made to classify the sub-volcanic unit based on immobile element concentrations (Nb/Y vs. Zr/Ti plot of Pearce, 1996). Results from 21 samples from six drillholes indicated dacitic to rhyolitic compositions for the Karatepe Member (Fig. 4.3; Table 4.1).

Least-altered samples of rhyolite-dacite porphyry comprise large phenocrysts of plagioclase, amphibole, and minor K-feldspar and quartz set in a fine-grained groundmass of plagioclase and quartz with biotite (Figs. 4.4 and. 4.5). Magnetite was observed as a common microphenocrysts phase both in the groundmass and as inclusions in hornblende (Fig. 4.6), whereas zircon and apatite occur as accessory minerals. Presence of hornblende and biotite indicates that dacite-rhyolite porphyry was formed from hydrous magmas with >4 wt.% H_2O (Loucks, 2014). Common

presence of magnetite phenocrysts (Fig. 4.6), on the other hand, reflects relatively oxidized nature of the source magmas.

Table 4.1. Immobile element (Nb, Ti, Y, and Zr) concentrations of 21 samples from different depth intervals from the Karatepe drill holes.

Drill hole	Depth From (m)	Depth to (m)	Nb (ppm)	Ti (wt.%)	Y (ppm)	Zr (ppm)	Zr/Ti	Nb/Y
SHD-031B1	113.00	114.50	0.1	0.006	9.12	6.40	0.1067	0.0110
SHD-031B1	129.50	131.00	0.09	0.007	8.52	5.90	0.0843	0.0106
SHD-031B1	150.00	151.50	0.09	0.005	8.52	6.60	0.1320	0.0106
SHD-031B1	142.50	144.00	0.08	0.005	7.63	4.50	0.0900	0.0105
SHD-031B1	131.00	133.00	0.09	0.005	8.73	5.80	0.1160	0.0103
SHD-031B1	122.00	123.50	0.09	0.005	8.91	5.90	0.1180	0.0101
SHD-031B1	84.00	85.50	0.07	0.005	6.98	4.80	0.0960	0.0100
SHD-033D1	169.50	170.50	0.12	0.005	5.90	4.40	0.0880	0.0203
SHD-033D1	162.50	164.00	0.1	0.006	8.73	6.20	0.1033	0.0115
SHD-033D1	144.00	145.50	0.09	0.005	8.09	5.80	0.1160	0.0111
SHD-033D1	161.00	162.50	0.09	0.006	8.60	5.40	0.0900	0.0105
SHD-100A	50.00	51.50	0.12	0.005	10.30	9.40	0.1880	0.0117
SHD-100A	51.50	53.50	0.09	0.005	7.86	10.40	0.2080	0.0115
SHD-101B	0.00	3.00	0.13	0.006	9.35	5.70	0.0950	0.0139
SHD-102B	115.50	117.00	0.11	0.005	8.83	8.00	0.1600	0.0125
SHD-102B	216.00	217.00	0.09	0.005	7.89	3.50	0.0700	0.0114
SHD-102B	120.00	121.50	0.11	0.006	10.05	7.10	0.1183	0.0109
SHD-102B	125.00	126.00	0.1	0.005	9.35	6.00	0.1200	0.0107
SHD-112A	185.50	186.50	0.07	0.005	4.61	4.30	0.0860	0.0152
SHD-114A	87.00	89.00	0.06	0.005	4.99	5.50	0.1100	0.0120
SHD-114A	91.00	93.00	0.06	0.005	5.09	6.80	0.1360	0.0118

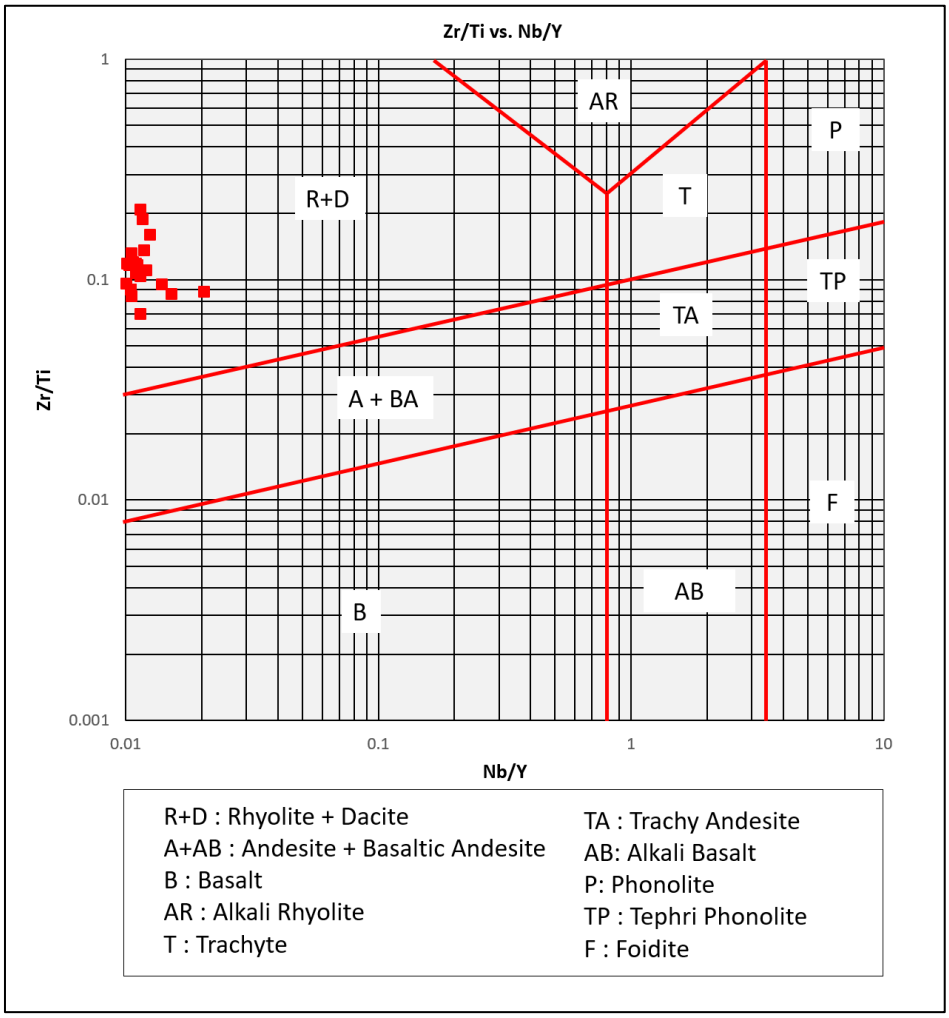

Figure 4.3. Zr/Ti vs. Nb/Y diagram (after Pearce, 1996) of moderately- to strongly-altered porphyritic rocks from drill core from the Karatepe Sector.

Figure 4.4. Least-altered samples of porphyritic unit in Karatepe Sector comprises large phenocrysts of plagioclase, amphibole, and minor K-feldspar and quartz set in a fine-grained groundmass of plagioclase and quartz. a) 440.20 to 444.60 m interval of dacite from SHD-107A drillhole, b) hand sample of least-altered dacite porphyry from the Karatepe Sector (481963E, 4463053N, 295 meters a.s.l.).

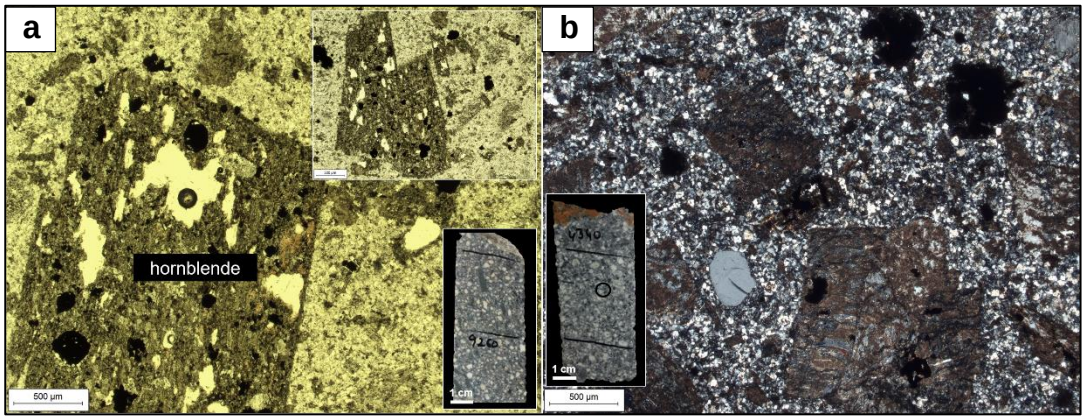

Figure 4.5. Microphotographs showing main minerals and textural features of least-altered porphyry unit (sample S138-9260) of the Karatepe Member, a) PPL, TL image showing large phenocrysts of euhedral horblende showing minor chloritization. Magnetite occurs as inclusions within hornblende, b) XPL, TL image of the same sample showing large phenocrysts of plagioclase (strongly altered to sericite), amphibole, and minor K-feldspar and quartz set in a fine-grained groundmass of plagioclase and quartz. (Abbreviations: TL = transmitted light; XPL = cross polarized)

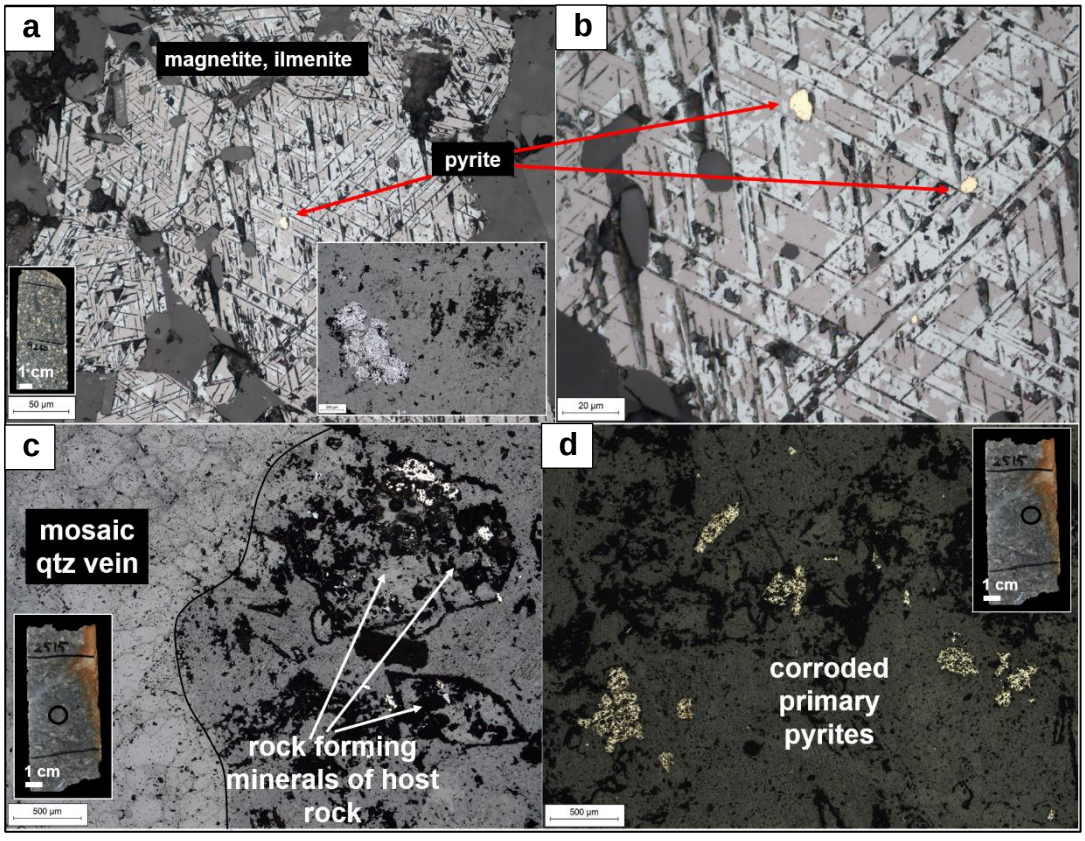

Figure 4.6. Microphotographs (RL, PPL images) showing porphyritic unit of the Karatepe Member, a) and b) S138-9260 sample showing magnetite with octahedral cleavage and exsolutions of possible ilmenite. Minute inclusions of pyrite are present in magnetite, c) and d) S138-2515 sample showing

porphyritic unit of the Karatepe Member cut by a quartz vein, containing primary minerals such as amphibole ±titanite bearing corroded pyrites. (Abbreviations: qtz = quartz; RL = reflected light; PPL = plane polarized light)

Graphitic mica schist of the Çamlıca Metamorphics as well as cross-cutting igneous lithologies of the Karatepe Member and Beyçayır Volcanics have been unconformably overlain by dominantly conglomerate and sandstone units of Sektaşı Formation in the northern part of the study area (Figs. 4.1 and 4.7). In the central part of the study area, a 0.25 km^2 area immediately east of the NW-trending valley is covered by talus and quartz float which hosts the Sırakayalar mineralization (Fig. 4.8). The widespread talus cover at Sırakayalar also consists of quartz vein fragments (up to approximately 2 meters in size) as well as fragments of mica schist and the porphyritic unit. These variably-sized vein and wall-rock fragments are cemented by a fine-grained wad that contains Fe-oxide and clays, which gives it a distinct red color in the surface (Fig. 4.2c). The transition from talus to the underlying mica schist is characterized by a damage zone which is not obvious at the surface. This zone consists of highly-deformed and partially brecciated schist as well as deformed mineralized veins (Fig. 4.9) that are occasionally boudinaged. This zone also marks the transition from oxide-rich material within the talus to sulfide zone preserved within the mica schist. Below the damage zone, mica schist contains pyrite and arsenopyrite.

Figure 4.7. Alternations of conglomerate and sandstone of the Sektaşı Formation (drill hole SHD-273A; 72.30-79.80 m).

Figure 4.8. Typical appearance of talus material comprising the shallow levels of the Sırakayalar Sector. Talus includes fragmented quartz-rich veins as well as fragments of schist (sch) and andesite (and) cemented by fine-grained hematite and clay, a) talus interval in drill hole SHD-249A (40.50–43.50 m), b) large vein fragment in talus in drill hole SHD-227B (9.00 – 12.00 m), c) andesite fragments in talus in drill hole SHD-227B (26.80 – 29.70 m).

Figure 4.9. Damage zone at the transition between talus and the basement graphitic schist unt in Sırakayalar, a) highly-deformed and locally clay-rich graphite-mica schist in drill hole SHD-236 (76.00 – 80.00 m), b) mineralized vein emplaced within highly-deformed graphite -mica schist in drill hole SHD-249A (73.00 – 76.50 m).

Both syn- and post-mineralization deformation has affected the lthological units and the Au-Ag mineralized veins in Şahinli. In the Karatepe Sector, schist and dacite porphyry contacts have been intensely sheared, and the veins also have undergone shear-related deformation by low-angle normal faults. (Figs. 4.10-4.12).

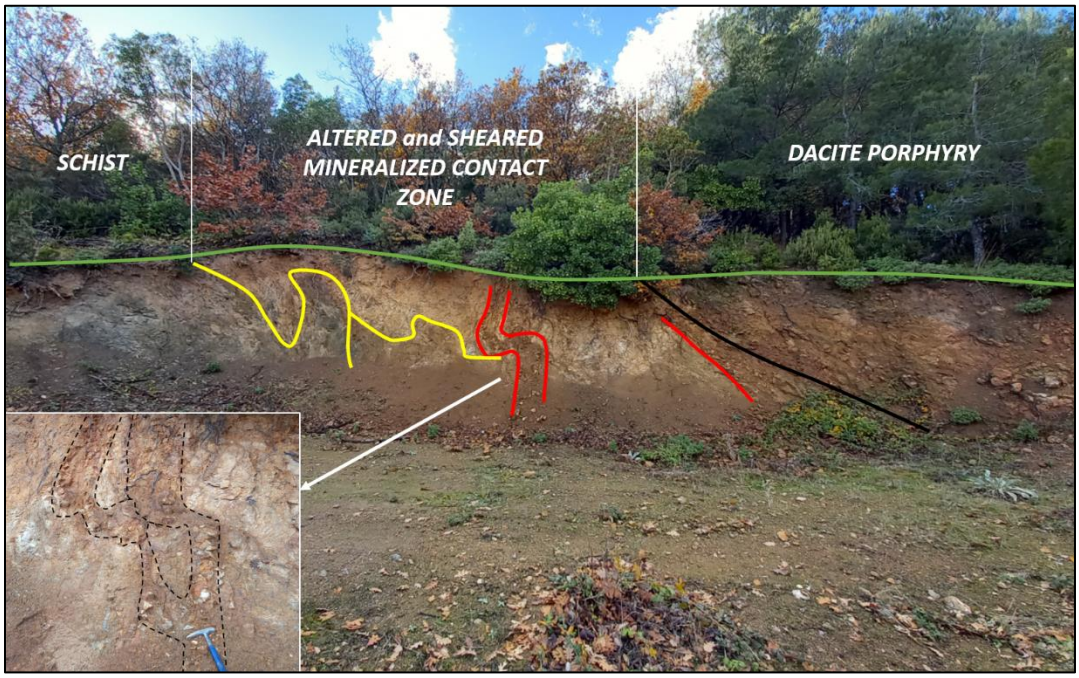

Figure 4.10. Sheared and altered zone between rhyolite-dacite porphyry and schist in Karatepe Zone (482140E, 4462831N, 359 m elevation; UTM Zone 35S).

Figure 4.11. Dacite porphyry and schist sheared high to modarete angle normal faults in Karatepe Zone (482050E, 4463024N, 306 m elevation; UTM Zone 35S).

Figure 4.12. Sheared and altered dacite porphyry in Karatepe Zone (481971E, 4463049N, 294 m elevation; UTM Zone 35S).

4.2 Mineralized Veins

4.2.1 Mineralized Veins in Karatepe

The Karatepe Sector comprises a series of structurally-controlled NNW–SSE (called as N-S, in this study) and E–W-trending (Fig. 4.13, steeply-dipping (ENE to S) quartz veins hosted within dacite porphyry and mica schist (Figs. 4.14 and 4.15). At the surface quartz veins are 0.5 to 15 meters thick and have strike lengths of approximately 200 to 300 meters (Fig. 4.1). Episodic hydrothermal activity in Karatepe resulted in development of a variety of vein textures developed over several distinct paragenetic stages. These include early mosaic/jigsaw-saccharoidal veins to later crustiform-comb, and cockade textures, and finally to amethystic quartz mostly occurring in comb-textured veins (Fig. 4.16). Although gold-silver mineralization was encountered in close spatial association with several of these paragenetic stages, massive dark gray quartz veins with native gold, electrum, pyrite, and arsenopyrite contain the highest grade intervals (>5.0 g/t Au). Highlighted intervals having combinations of saccharoidal, cockade, comb and crustiform, comb, mosaic/jigsaw, plumose quartz textures show arsenopyrite, electrum, pyrite, gold in pyrite and gold as quartz infill.

Quartz veins that macroscopically appear as massive veins are observed to be mainly composed of saccharoidal and mosaic quartz under the microscope. Mosaic quartz is associated with a wide range of Au and Ag contents varying from <0.1 ppm to >5 ppm Au (Figs. 4.17 and 4.18). Also, highest Ag grades were encountered in veins displaying massive quartz textures (Fig. 4.18). Cockade, comb and stockworking quartz veinlets, on the other hand, are generally associated with lower Au grades (<1.5 g/t Au; Fig. 4.19 b-d).

Figure 4.13. Steeply-dipping E-W trending vein (482169E, 4462785N, 363 m elevation; UTM Zone 35S).

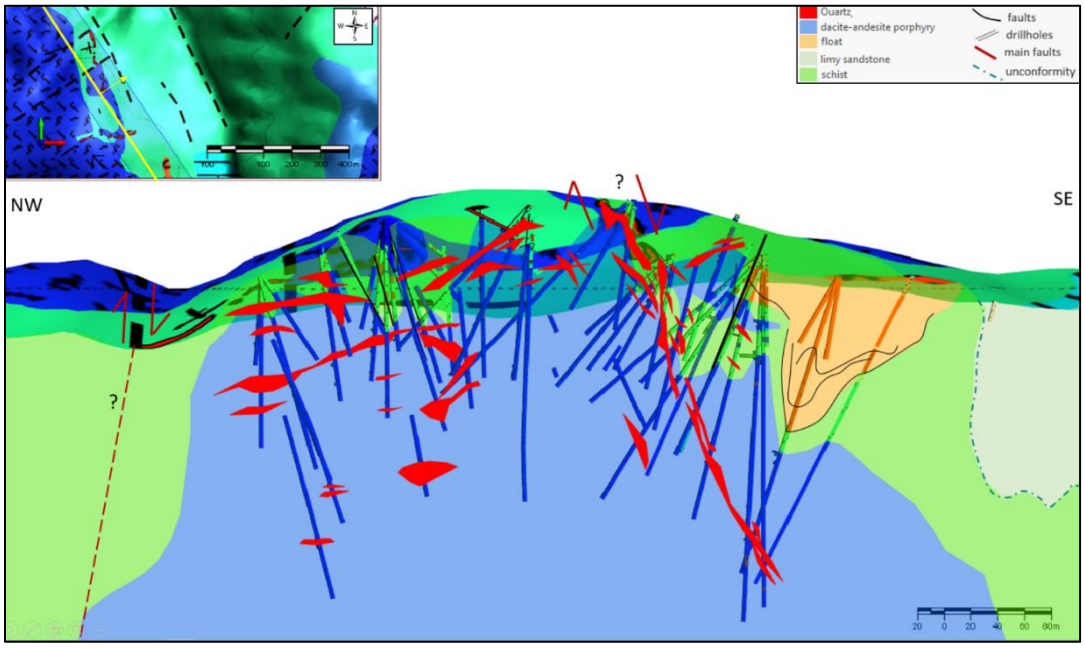

Figure 4.14. NW-SE cross-sectional view from Karatepe Zone, showing quartz veins within the host rocks.

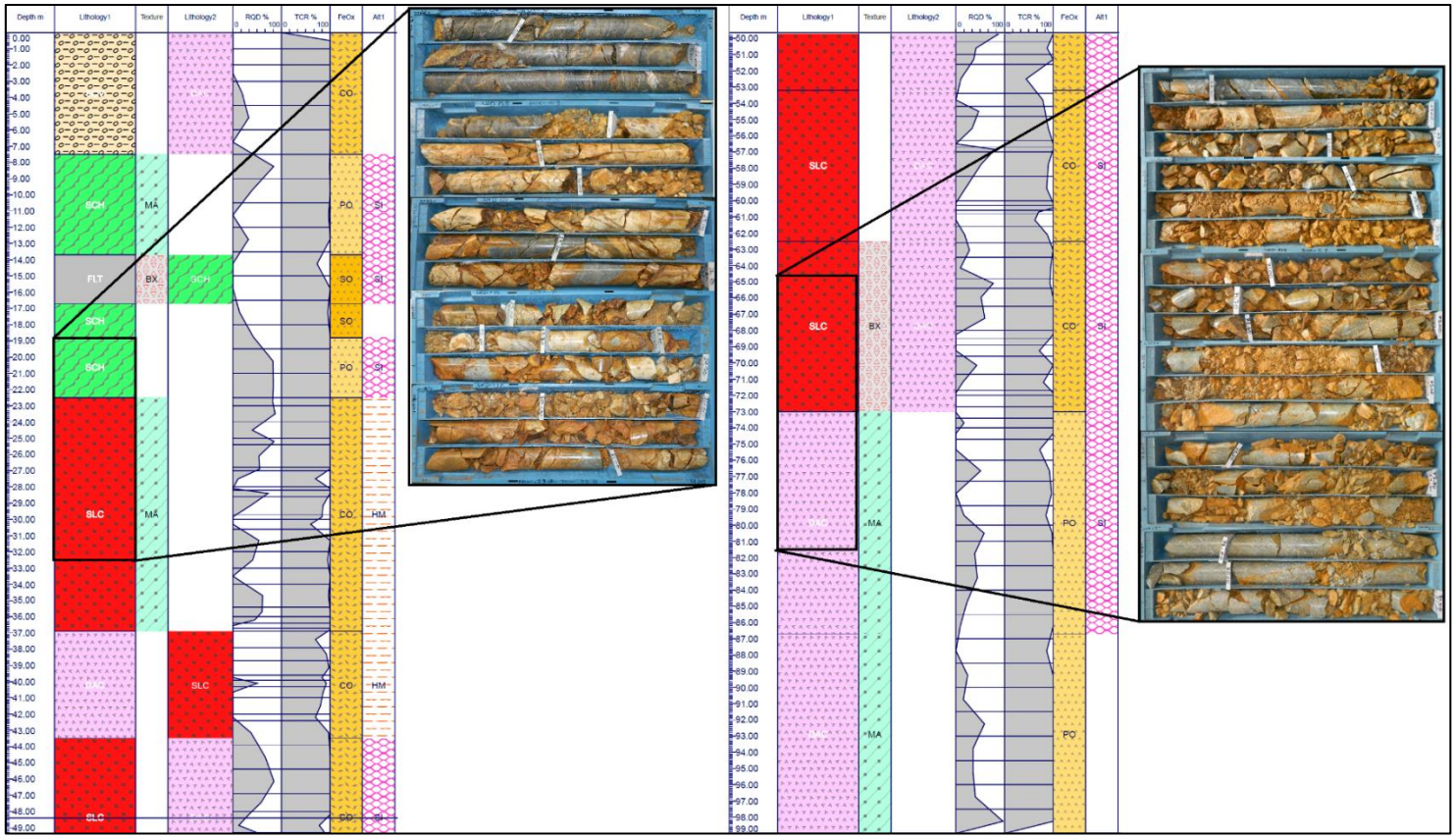

Figure 4.15. Strip-log for SHD-138, SCV (Sedimentary cover), SCH (Schist), FLT(Fault), SLC (Quartz Vein), DAC (Dacite), MA (Massive),BX (Brecciated), CO (Completely Oxidized), PO (Partially Oxidized), SO (Strongly Oxidized), UO (Unoxidized), SI (Silicification), HM (Hematized). RQD (Rock Quality Designation), TCR (Total Core Recovery).

Figure 4.16. Macro-scale epithermal textures in quartz veins from from Karatepe Zone.

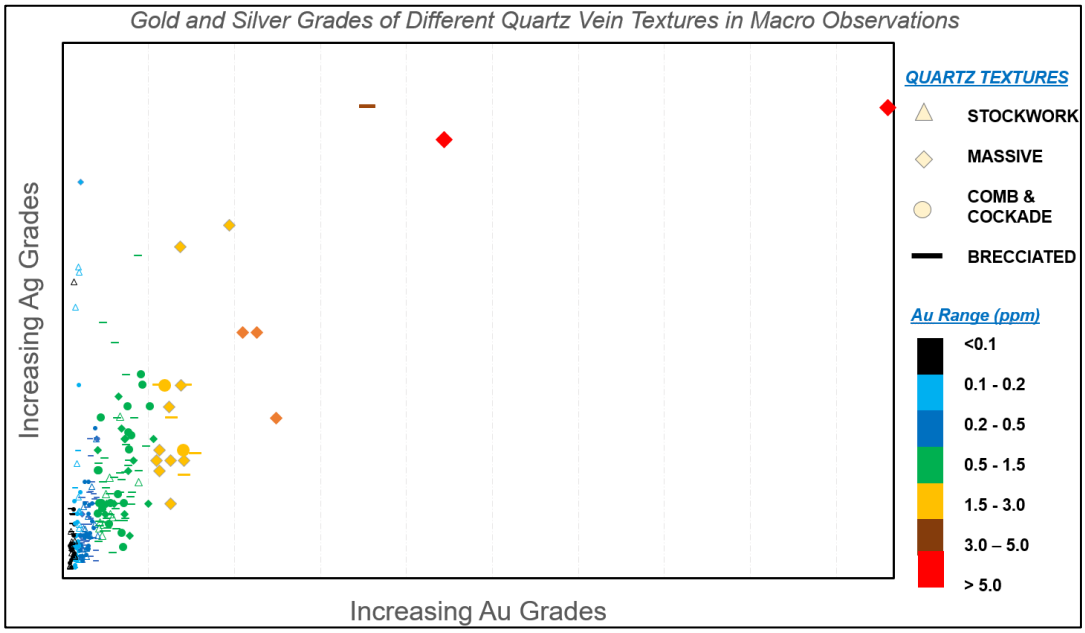

Figure 4.17. Relationship between Au and Ag grades and observed macroscopic quartz vein textures for samples selected from 38 drillholes and 391 vein intervals from the Karatepe Sector.

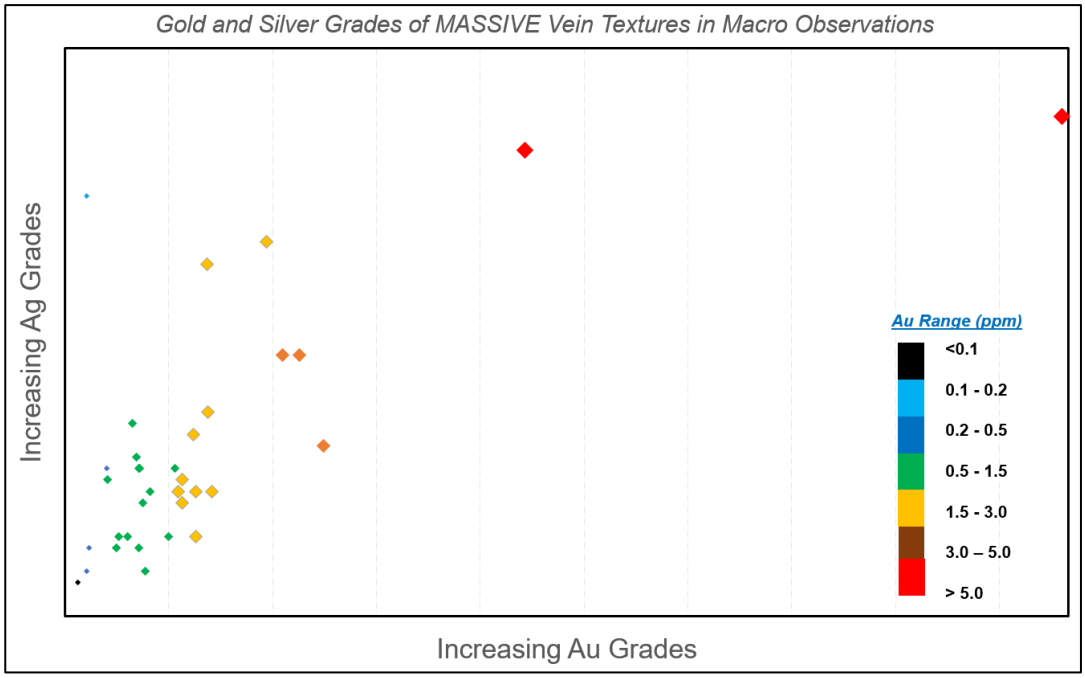

Figure 4.18. Au and Ag grades of massive crystalline quartz vein textures in macro-scales, samples selected from the drillholes of Karatepe Zone

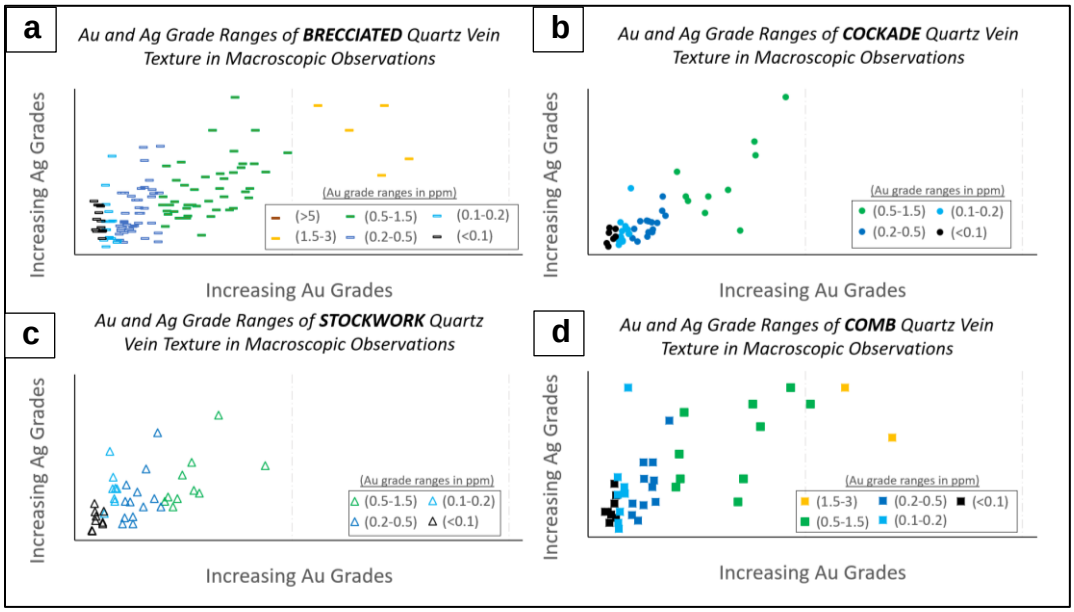

Figure 4.19. Relationship between Au and Ag grades and macro-scale quartz vein textures. Samples selected from the drillholes of Karatepe Zone a) for brecciated quartz vein, b) cockade quartz vein, c) stockwork quartz veins/veinlets, d) comb quartz vein.

Episodic deformation seems to be one of the key controlling factors on mineralization in the study area since their effects can be observed even in micro-scales of mineralized intervals. Macro-scale and petrographic observations indicated that brecciation developed in all hydrothermal stages in Karatepe, and are associated with both low and medium gold grades (<0.1 g/t up to 3/0 g/t Au; Fig. 4.19a). Also in addition, the orientation of the veins in Karatepe is similar with the mineralized of the adjacent Lapseki Au deposit in the south, which were suggested to have formed due to repeated vein reactivation during multiple cycles of deformation and associated hydrofracturing (Gülyüz et al., 2018); this brings that Karatepe mineralized vein system should be formed in repeated reactivation resulted in deformation which triggers permeable pathways of Au and Ag mineralization, like in Kestanelik epithermal vein system of Lapseki Au deposit.

4.2.1.1 Microscopic Quartz Textures in Karatepe

Steeply dipping, NE-SW- and E-W-trending veins from Karatepe Sector display a great variety of mesoscopic and microscopic quartz textures that often display overprinting relationships Additionally, textural variation was also observed throughout different hydrothermal stages and with respect to depth of formation (from surface down to 125 m depth, in this study). Therefore, the samples collected from mineralized veins show various quartz textures (Fig. 4.20). They were observed on samples collected from SHD-154 (elevation: 392 m a.s.l) drill hole and from SHD-138 drill hole (elevation: 332 m a.s.l.).

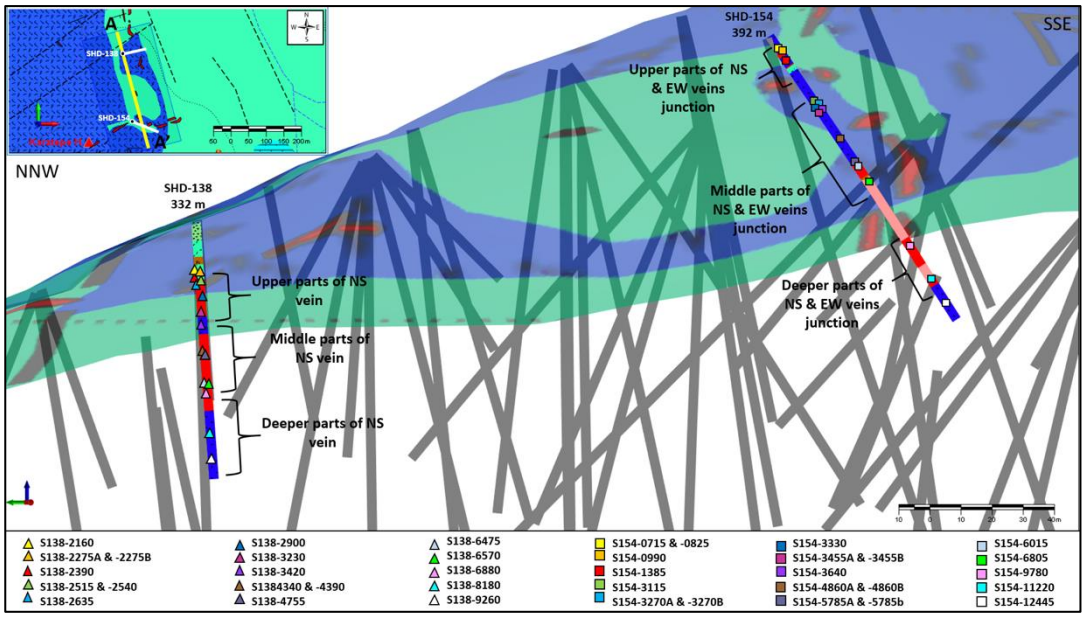

Figure 4.20. NNW-SSE cross-section view showing examined drillholes (SHD-138 and SHD-154) sample locations from the epithermal veins (at NNW-SSE/considered as N-S vein and at junction of E-W and NE-SW vein) and their wall-rocks (predominantly dacite porphyry and schist).

Karatepe quartz textures are characterized by early primary quartz, whereas others include recrystallized and replacement-type quartz (e.g., crustiform, mosaic/jigsaw and saccharoidal, respectively). Paragenetic relationships among these were established from cross-cutting relationships observed both at the drill core and also during petrographic studies.

Quartz textures at Karatepe have been broadly classified into three paragenetic stages as: (1) massive crystalline quartz, (2) comb-crustiform quartz, and finally (3) cockade-comb quartz (Fig. 4.21). Additionally, all paragenetic stages are accompanied by brecciation, and some samples show at least two separate phases of breccia formation (Fig. 4.21).

Higher grade (>3 g/t Au) zones at Karatepe are consistently associated with early crystalline quartz (Figs. 4.17 and 4.18), including mosaic and/or jigsaw textured quartz as well as saccharodial quartz. These textures are commonly observed in isolated veins, but their stockwork veinlets also occur occasionally. Other quartz phases, on the other hand, generally contain relatively lower Au and Ag grades (<3 g/t Au, mostly <1 g/t Au; Fig. 4.19).

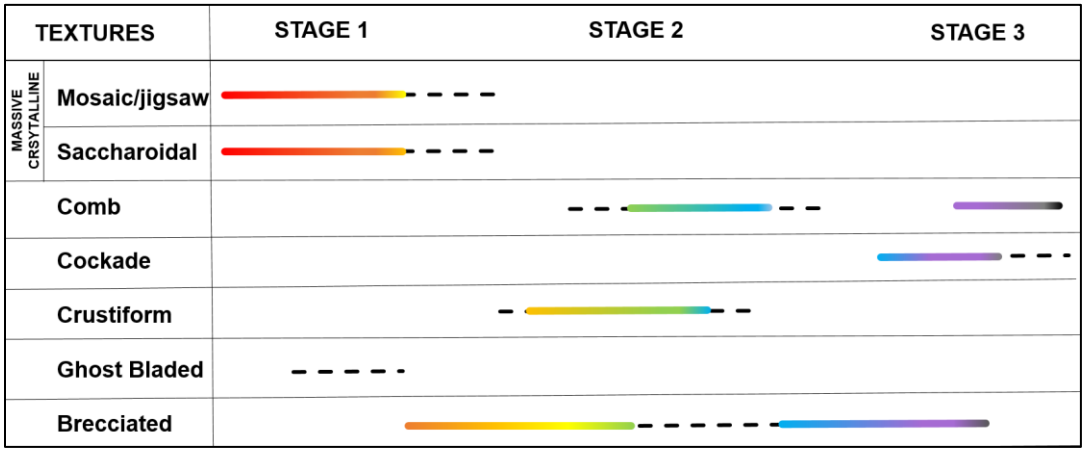

Figure 4.21. Paragenetic relationship among different quartz textures at the Karatepe Sector.

Stage 1: Massive Crystalline Mosaic/Jigsaw to Saccharoidal Quartz

Karetepe quartz veins with massive appearance at the hand specimen can be mostly characterized by the appearance of microscopic vein textures with mosaic/jigsaw and saccharoidal quartz vein fill. Mosaic/jigsaw quartz textures can be observed as aggregates of crystalline quartz as interpenetrating quartz grain boundaries with various grain sizes (from finely-crystalline to coarse quartz; Fig. 4.22). Saccharoidal quartz was observed as loosely packed and randomly distributed fine-grained anhedral quartz aggregates (Figs. 4.23b–d). Saccharoidal quartz is often closely related with fine- to medium-grained mosaic/jigsaw textures both spatially and temporally. That is, they can be generally seen in moderate depths (between 30 and 90 m depth) and rarely in deeper intervals. These were later overprinted by brecciation and comb quartz (Figs. 4.22e, 4.22f, 4.23b, 4.23d, 4.24a, 4.25a and 4.25d).

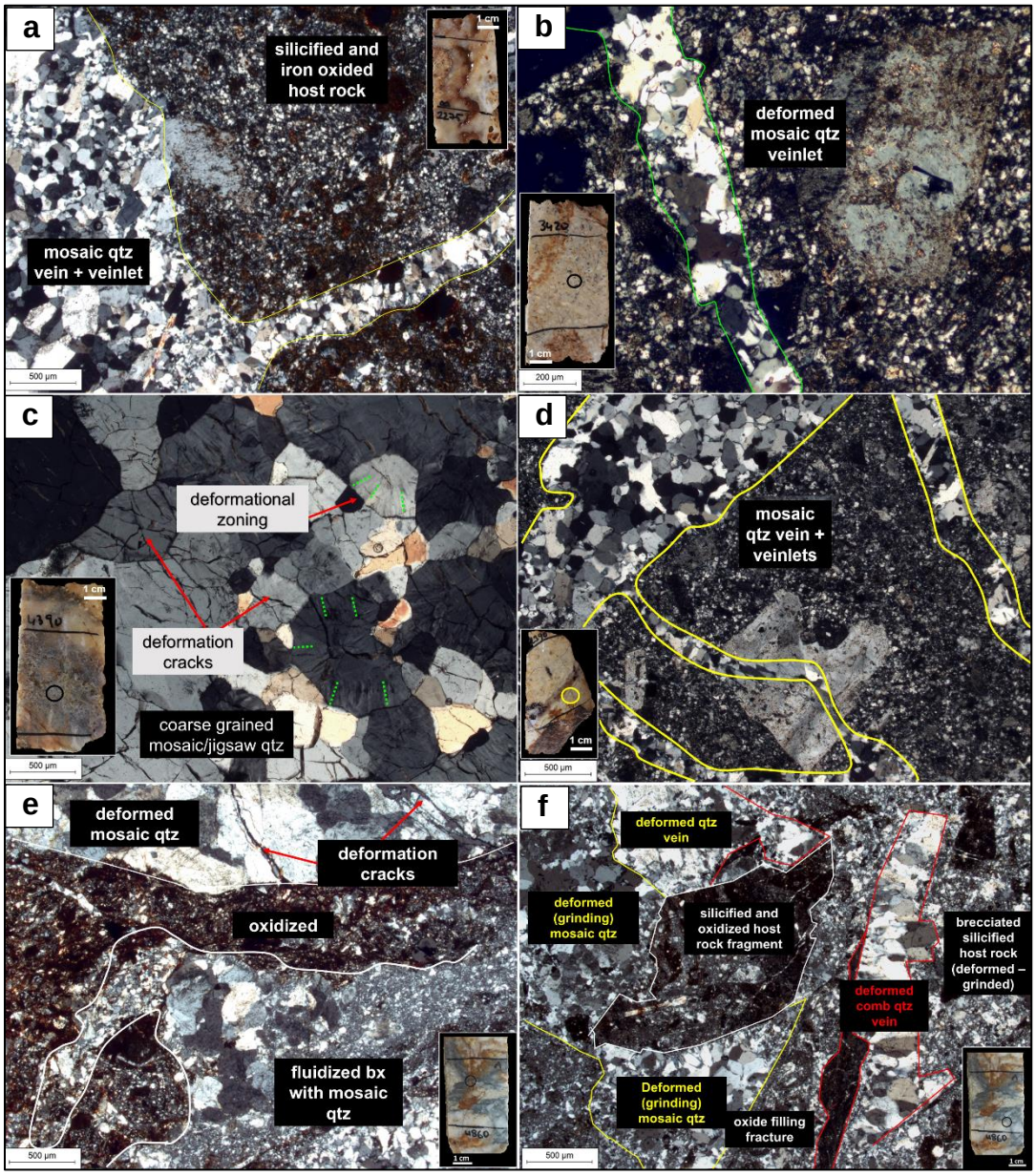

Figure 4.22. Microphotographs (XPL, TL image) of mosaic/jigsaw quartz textures. a) Fine- to medium-grained mosaic quartz vein cross-cutting silicified porphyry (drill hole SHD-138, 22.75 m depth), b) Mosaic quartz vein fill in silicified porphyry (drill hole SHD-138, 34.20 m depth), c) Deformed and partly cracked coarse-grained mosaic/jigsaw quartz (drill hole SHD-138, 43.90 m depth), d) Fine- to medium-grained, weakly-stockworking mosaic/jigsaw quartz vein infill cross-cutting silicified porphyry (drill hole SHD-138, 23.90 m depth), e) Fluidized breccia with highly-deformed mosaic quartz and surrounding fine-grained matrix containing Fe-hydroxides (drill hole SHD-154, 48.60 m depth), f) Same sample as (e) showing mosaic/jigsaw quartz in fluidized breccia. (Abbreviations: qtz = quartz; TL = transmitted light; XPL = cross polarized light).

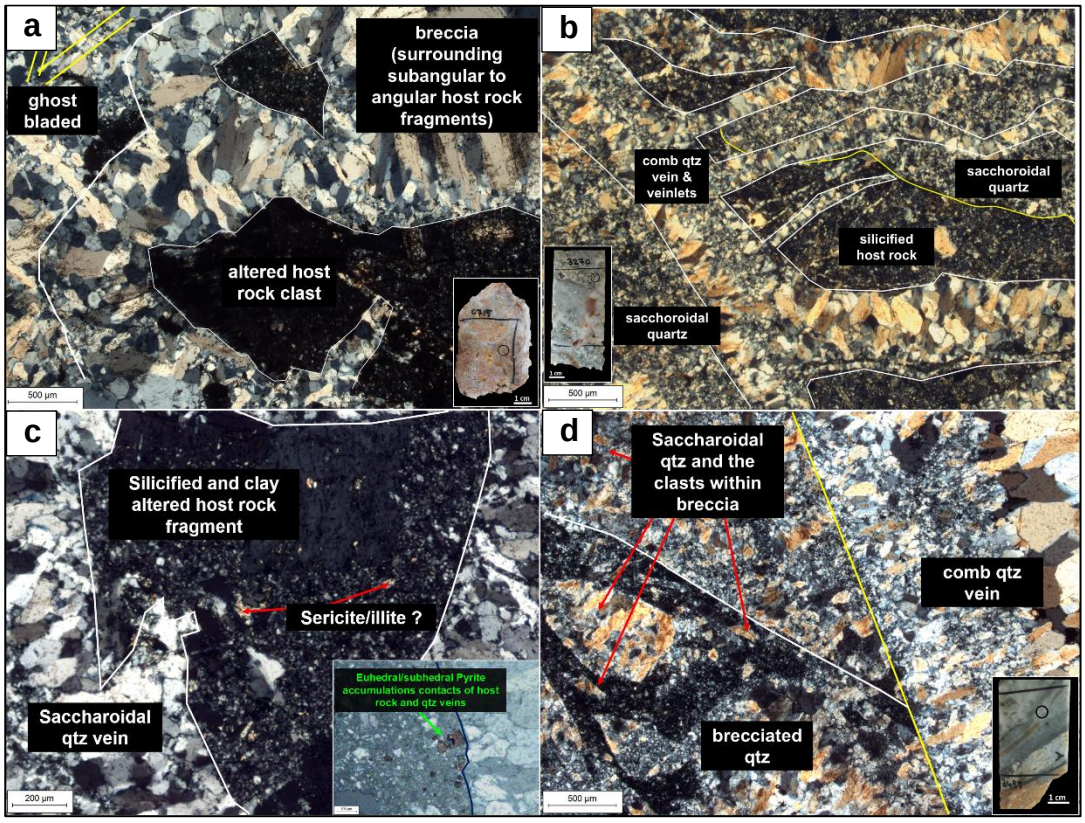

Figure 4.23. Microphotographs (XPL, TL image) of ghost-bladed and saccharoidal quartz textures. a) Weakly-developed ghost-bladed quartz (Stage 1; look at other quartz textures topic) overprinted by paragenetically late hydothermal breccia of Stages 1-2 (drill hole SHD-154, 07.15 m depth), b) Saccharoidal quartz (Stage 1) in silicified porphyry cut by comb quartz of Stage 2 (drill hole SHD-154, 32.70 m depth, c) Saccharoidal quartz (Stage 1) surrounding silica-clay altered porphyry fragment (drill hole SHD-154, 34.55 m depth), d) Early fine- to medium-grained saccharoidal quartz (Stage 1) brecciated and later cut by comb quartz vein of Stages 2-3 (drill hole SHD-154, 34.55 m depth). (Abbreviations: qtz = quartz; TL = transmitted light; XPL = cross polarized light).

Stage 2: Crustiform to Comb Quartz

In the Karatepe Sector, Stage 2 mineralization is represented by crustiform to comb quartz developed (1) as vein fill, or (2) as bands surrounding brecciated clasts of either altered wall-rocks or fragments of saccharoidal to mosaic/jigsaw quartz of Stage 1. Crustiform texture is characterized by successive bands consisting of euhedral to subhedral prismatic crystals of quartz with varying grain sizes (Figs. 4.25 a, b, d). Thicknesses of crustiform-banded or comb quartz veins are highly variable and range between 0.5 and 5 mm. This texture is best developed at shallow to medium depths of the Karatepe Sector. Comb quartz typically occupies the outer

crustiform bands, where it was observed to have developed symmetrically along vein margins (Fig. 4.26). Crustiform and comb texture have been locally overprinted by a later stage of deformation that has led to development of open-space fractures in Karatepe.

Stage 3: Cockade to Comb Quartz

Cockade texture was developed from shallow to medium depths (from surface levels to 50 m depth) and represents the latest stage of hydrothermal activity in the Karatepe Sector (Figs. 4.25c, e, f). These contain well-developed concentric bands surrounding quartz fragments of Stages 1 and 2 as well as fragments of altered wall-rocks and host rock fragments, particularly along the E-W-trending veins (Fig. 4.1). Amethystic purple quartz is a common component of cockade structures, and is likely a product of higher temperature conditions of the epithermal system. Intervals with cockade textures lack sulfide minerals and other ore mineral phases (e.g., native Au and electrum), and as such these are not associated with significant Au and Ag grades.

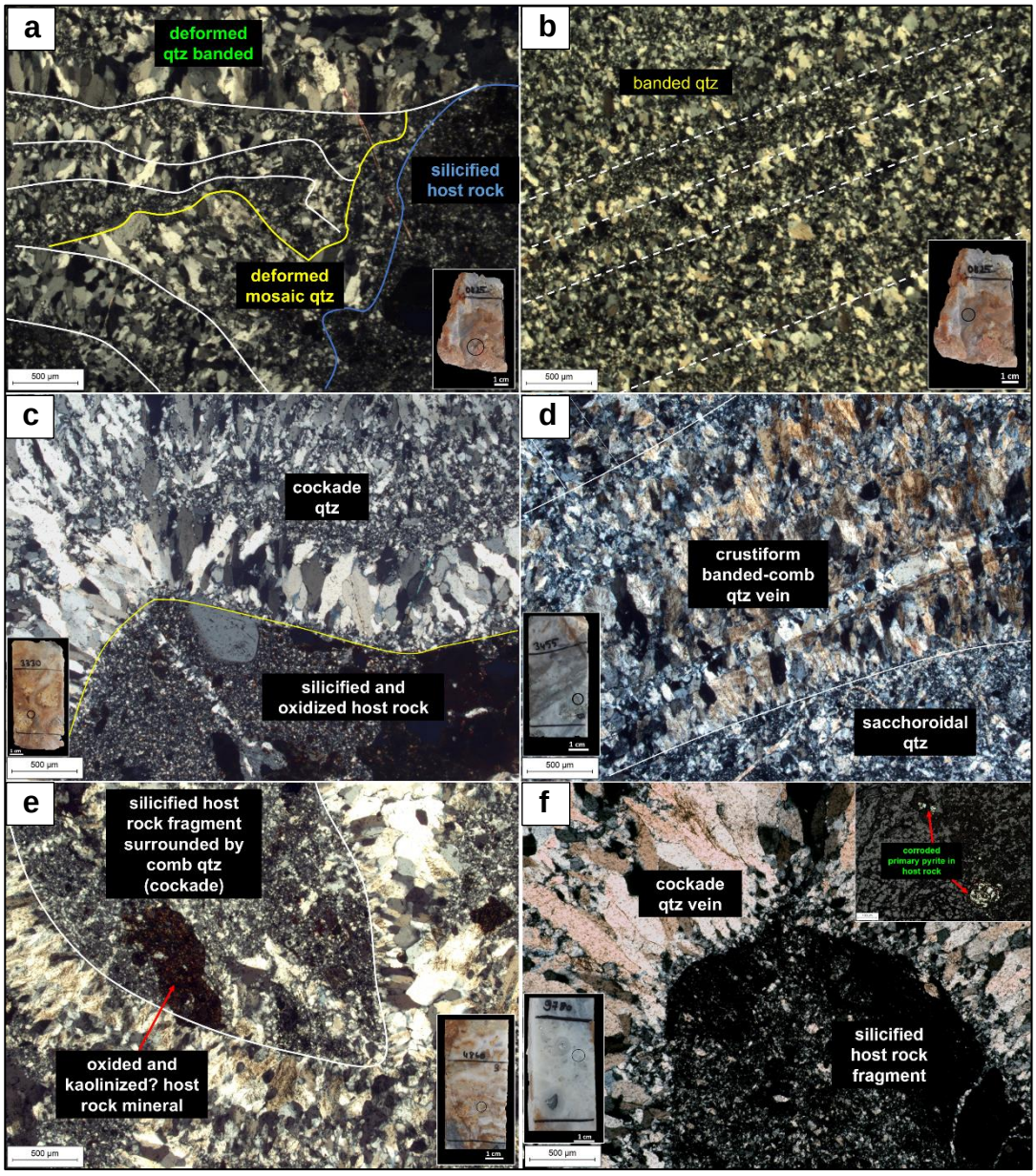

Figure 4.24. Microphotographs of crustiform and cockade quartz textures from selected samples of SHD-154 drill hole (XPL, TL image), a) Brecciation results in not only breccia clasts of subrounded to rounded host rock but also crustiform textured quartz vein (Stage 2) formed as a previous phase (drill hole SHD-154, 08.25 m depth), b) Crustiform texture (Stage 2) in an angular breccia clast of quartz vein (drill hole SHD-154, 08.25 m depth), c) Cockade quartz texture (Stage 3) surrounding an altered host rock fragment (drill hole SHD-154, 33.30 m depth), d) Crustiform texture (Stage 2) as gray quartz veinlet cutting (Stage 1) saccharoidal quartz (drill hole SHD-154, 34.45 m depth), e) Cockade quartz texture (Stage 3) surrounding silicified and clay altered host rock fragment (drill hole SHD-154, 48.60 m depth), f) Cockade texture (Stage 3) surrounding almost totally silicified host rock fragment (drill hole SHD-154, 97.80 m depth). (Abbreviations: qtz = quartz; TL = transmitted light; XPL = cross polarized light).

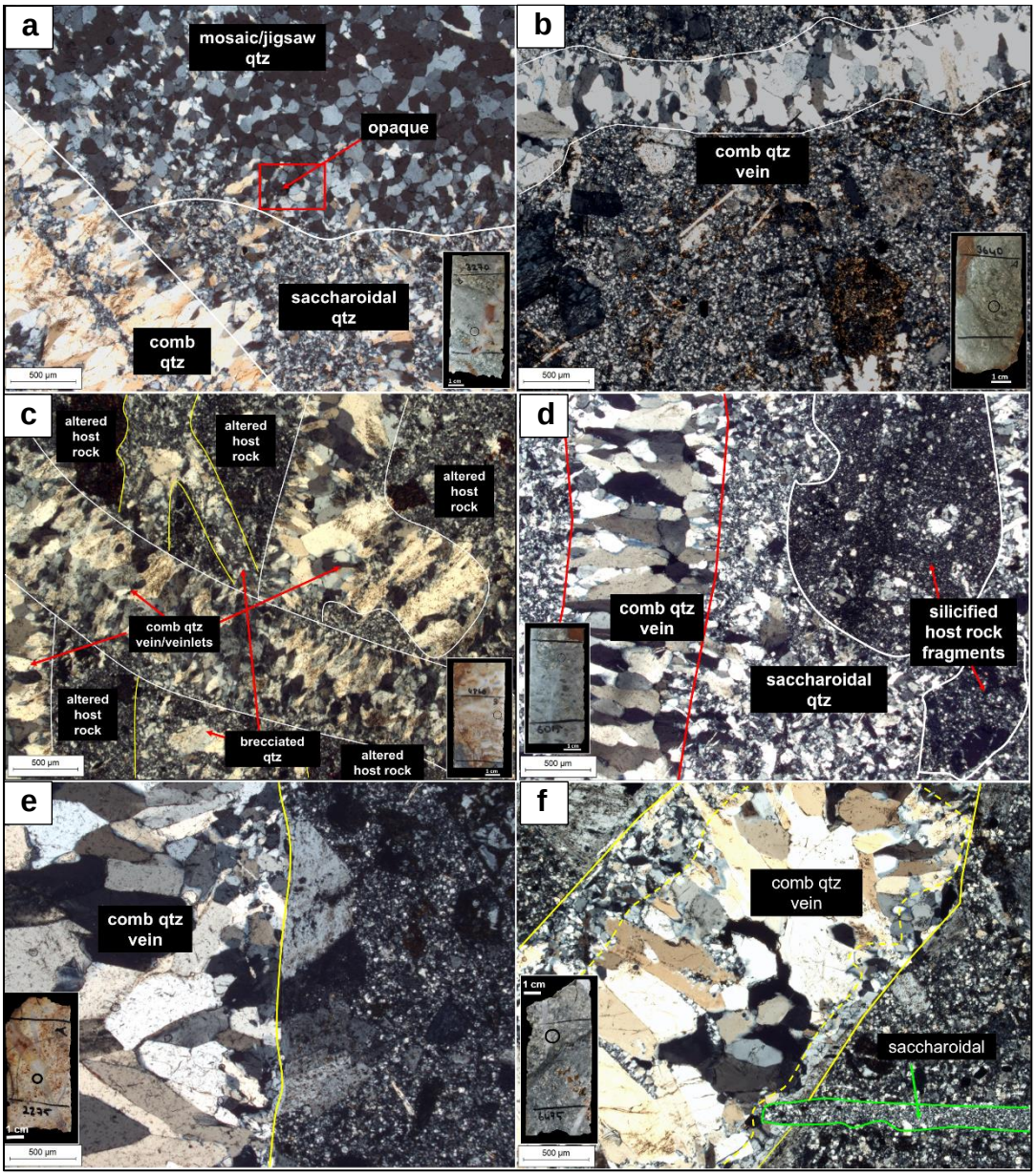

Figure 4.25. Microphotographs containing comb quartz textures together with other textures from selected samples of SHD-154 and SHD-138 drill holes (XPL, TL images), a) Late (Stage 2-3) phase brittle/straight comb textured quartz vein cutting through previous (Stage 1) sacchroidal and mosaic/jigsaw textured quartz phases (drill hole SHD-154, 32.70 m depth b) Comb to mosaic (Stage 1-2) textured quartz veinlet cutting altered host rock (drill hole SHD-154, 36.40 m depth) c) Several brittle to ductile comb quartz vein (Stage 2) cutting by brittle/straight comb vein (Stage 3) indicating later phase (drill hole SHD-154, 48.60 m depth) d) (Stage 3) brittle/straight comb quartz textured vein with coarse crystals cutting through previous medium grained (Stage 1) saccharoidal textured, brecciated vein (drill hole SHD-154, 60.15 m depth) e) Brittle/straight comb quartz vein (Stage 3) cutting through mostly clay altered and silicified host rock (drill hole SHD-138, 22.75 m depth) f) Coarse grained brittle/straight comb texture (Stage 3) quartz vein as previous phase than fine saccharoidal textured quartz phase (drill hole SHD-138, 64.75 m depth). (Abbreviations: qtz = quartz; TL = transmitted light; XPL = cross polarized light).

Brecciated Quartz (Stage 1-2, Stage 2-3)

Brecciated textures were encountered from surface to the deepest levels of mineralized veins. These mostly contain clasts of massive crystalline veins with saccharoidal and mosaic/jigsaw quartz as well ascomb textures since these are the early to medium stages of mineralization related with those textured quartz (Stages 1-2; Figs. 4.23d and 4.26). Therefore, brecciated textures may be responsible to have highlighted Au and Ag grades together with low to moderate grades of them. Early brecciation was followed by late stage brecciation is also following by a second brecciation event (Stages 2-3) containing the fragments of the early brecciation phase (Fig. 4.26). Also, brittle and ductile developed during brecciation events. These features could not be added to any stages for brecciations; however, it can be understood that not only multi-phases single type brecciation events stand for the mineralized vein but also different type of brecciation events as fluidized and brittle forms (Figs. 4.22e and 4.22f).

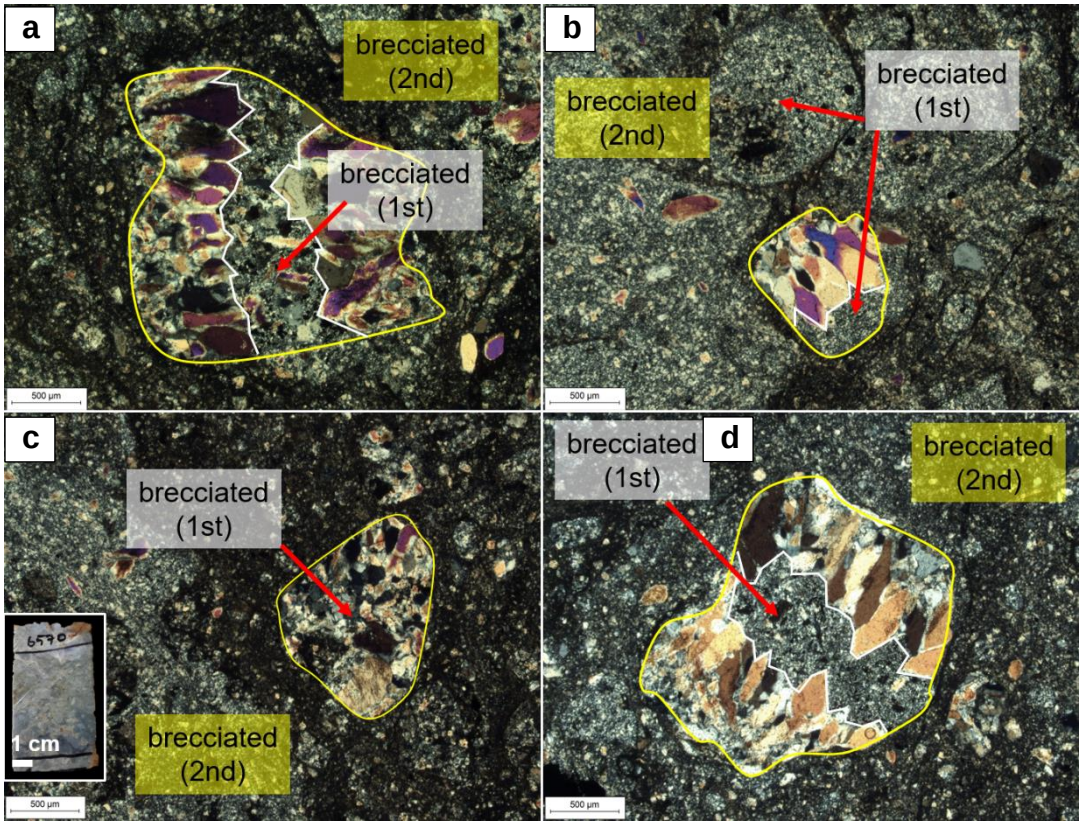

Figure 4.26. a), b), c) and d) Microphotographs showing at 2 different brecciation phases (XPL, TL image). (Abbreviations: TL = transmitted light; XPL = cross polarized light).

Other Quartz Textures

In addition to the aforementioned major quartz phases controlling the mineralization, there are also some other quartz textures which were identified as feathery, ghost bladed and plumose textures. The plumose quartz texture was observed as growing throughout vugs/cavities can be observed at moderate depths of the system of the Karatepe Sector (Fig. 4.27). In epithermal systems, hydrothermal fluids may partially to completely fill existing vugs formed vugs. The feathery quartz texture is well developed on the margins of a quartz crystal as splintery appearance, and it is rarely observed throughout the entire system (Fig 4.28). Ghost bladed quartz is a replacement texture style, and is rarely seen in the shallower parts of the Karatepe vein system (Fig. 4.24a).

These textures can be observed in micro-scales as accompanying the main textures of quartz stages; however, they can not be specifically linked with any of the main paragenetic stages.

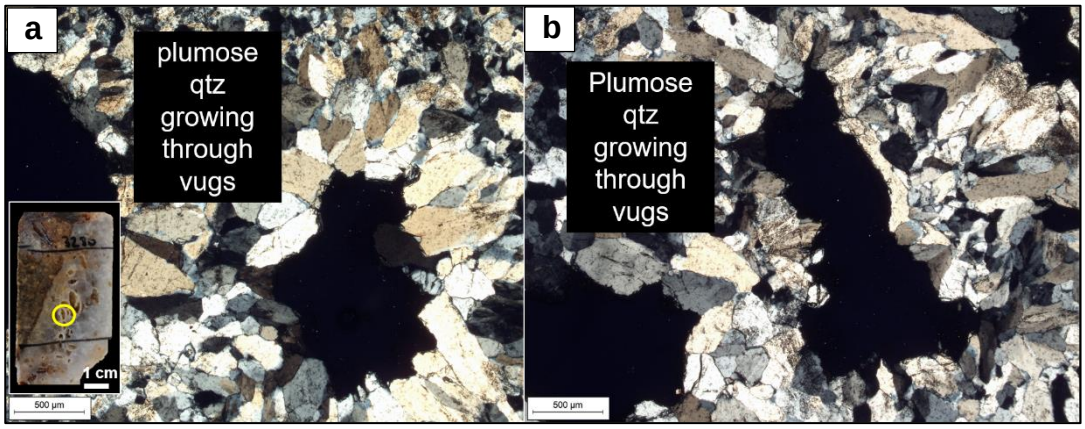

Figure 4.27. Microphotographs (XPL, TL image) of open-space filling plumose quartz textures from sample S138-3230 obtained from Karatepe (drill hole SHD-138, 32.30 m depth) a) plumose quartz lining vugs or b) open fractures. (Abbreviations: qtz = quartz; TL = transmitted light; XPL = cross polarized light).

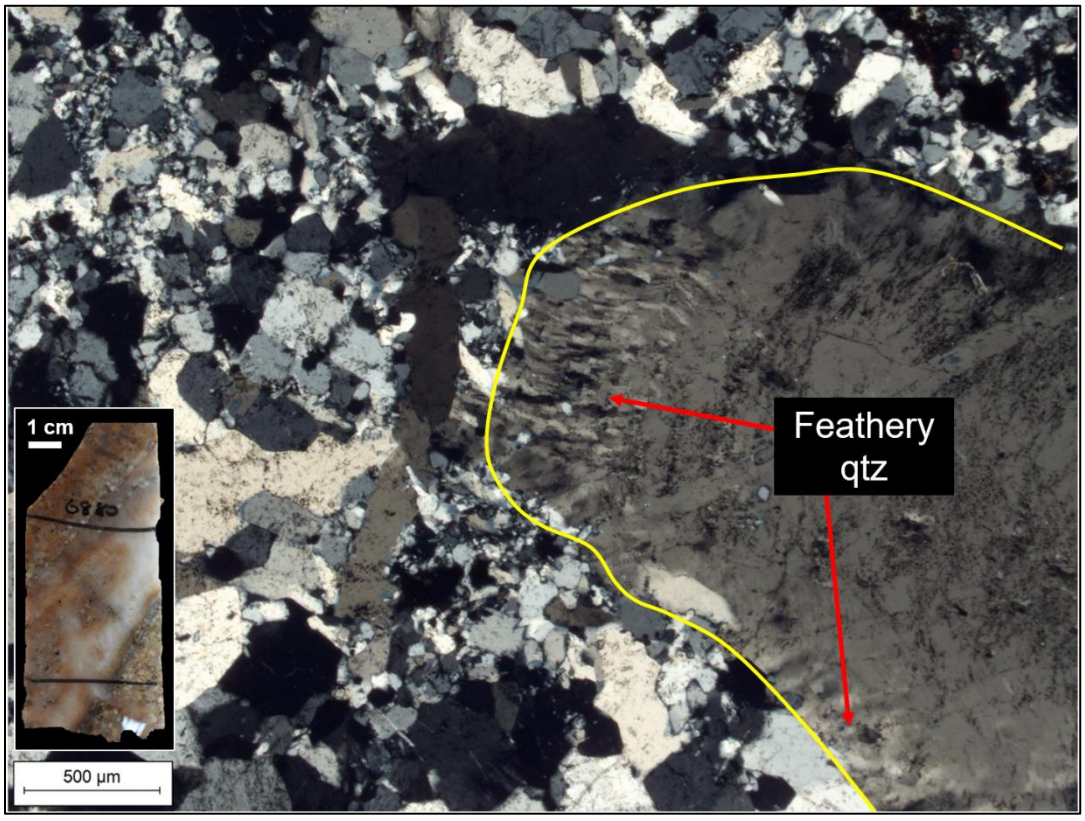

Figure 4.28. Microphotograph (XPL, TL image) of vein quartz showing feathery texture developed on the margins of a quartz crystal with splintery appearance (drill hole SHD-138, 68.80 m depth). (Abbreviations: qtz = quartz; TL = transmitted light; XPL = cross polarized light).

Micro-scale Evidence of Deformation in Karatepe

Micro-scale observations of siliceous veins and breccias from Karatepe revealed strong deformation textures such as deformational cracks, crystal grindings (i.e. cataclastic textures) and deformational zoning of quartz in addition to brecciation (Figs. 26, 29 and 30). At least one or two brecciation events were be identified by microscopic observations; however, more episodic deformational events in micro-scales related with the main deformational events should be deduced since they can be observed from the earliest to the latest quartz phases related with the mineralization.

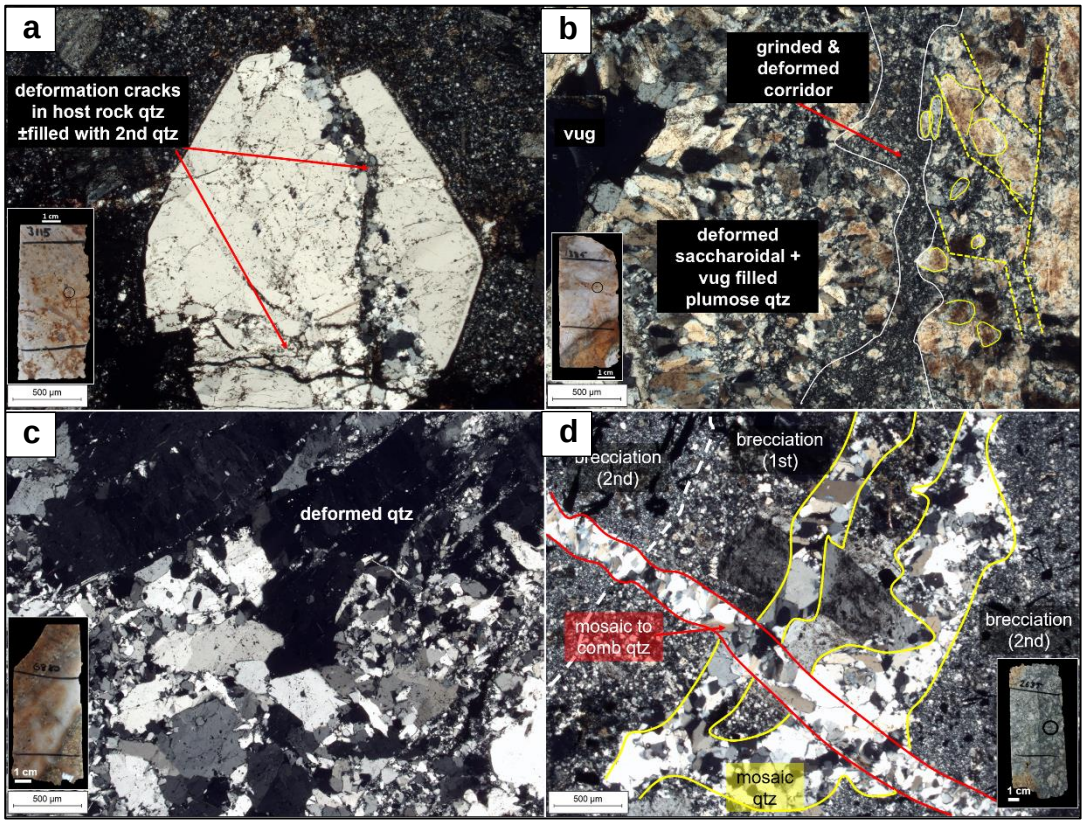

Figure 4.29. Microphotographs (XPL, TL image) of deformation related textures from Karatepe. a) Fractured igneous quartz in altered porphyry with hydrothermal quartz infill (drill hole SHD-154, 31.15 m depth), b) Cataclasized and brecciated saccharoidal quartz (Stage 1). Fine-grained quartz developed due to pulverization during brecciation. Vug to the left is partially filled by plumose quartz (drill hole SHD-154, 13.85 m depths), c) Brittle deformation and weak cataclasite development in massive quartz (drill hole SHD-138, 68.80 m depth), d) 2-phase (fine and medium matrixed) brecciation (Stage1) cut by mosaic/jigsaw veintlets (Stage 1) (drill hole SHD-138, 26.35 m depth). (Abbreviations: qtz = quartz; TL = transmitted light; XPL = cross polarized light).

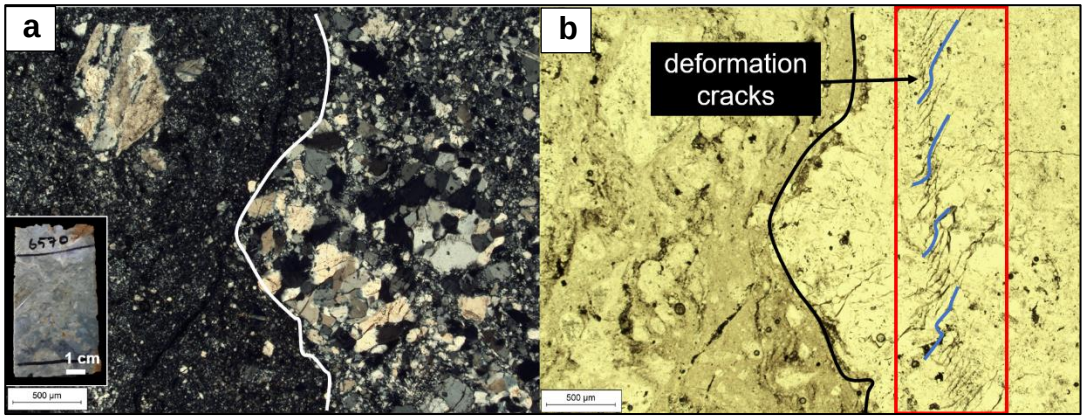

Figure 4.30. Microphotographs of fluidized breccia (drill hole SHD-138, 65.70 m depth). a) Breccia clast dominated by mosaic quartz in silicified porphyry surrounded by a fine-grained matrix (TL, XPL

image), b) micro-cracks developed in mosaic quartz from the same sample (TL, PPL). Abbreviations: TL = transmitted light; XPL = cross polarized light; PPL = plane polarized light).

4.2.2 Mineralized Veins in Sırakayalar

Sırakayalar Sector is located approximately 800 meters northwest of Karatepe, from which it is separated by a steep and possibly structurally-controlled N-S valley (Fig. 4.1). Sırakayalar orebody is distinct from the Karatepe veins as mineralized veins are highly-disrupted due to episodic and repetitive faulting. Consequently, fragments of mineralized veins are now contained within a fine-grained float/talus material characterized predominantly by Fe-oxides and clay (Fig. 4.2c).

Figure 4.31. Outcrop of a rootless siliceous vein block dipping towards SE sitting atop the basement graphitic schist and float/talus material in Sırakayalar (482840E, 446337N, 352 m a.s.l.). This block is thougt to represent the primary mineralized veins in Sırakayalar, which are now strongly disrupted and displaced.

At Sırakayalar, primary mineralization is restricted to a small area, where old mine workings are present (Fig. 4.31). A number of old galleries were intersected during exploration drilling (Fig. 4.32). Although most of the Sırakayalar vein system has

been displaced, there are a few boulder sized large siliceous blocks to the south of the talus-rich zone that remain relatively intact. A variety of epithermal-style textures were observed in these siliceous fragments including banded veins, brecciates, and bladed texture (Fig. 4.33). The siliceous fragments have been drill tested by ESAN, but drill holes did not intersect any vein material below depths of 50 meters (Fig. 4.32). As such, these are regarded as rootless veins remnant from the primary mineralization. Rootless veins are generally highly-deformed and disrupted; however, they are observed as dipping towards ESE and SE directions (Fig. 4.32).

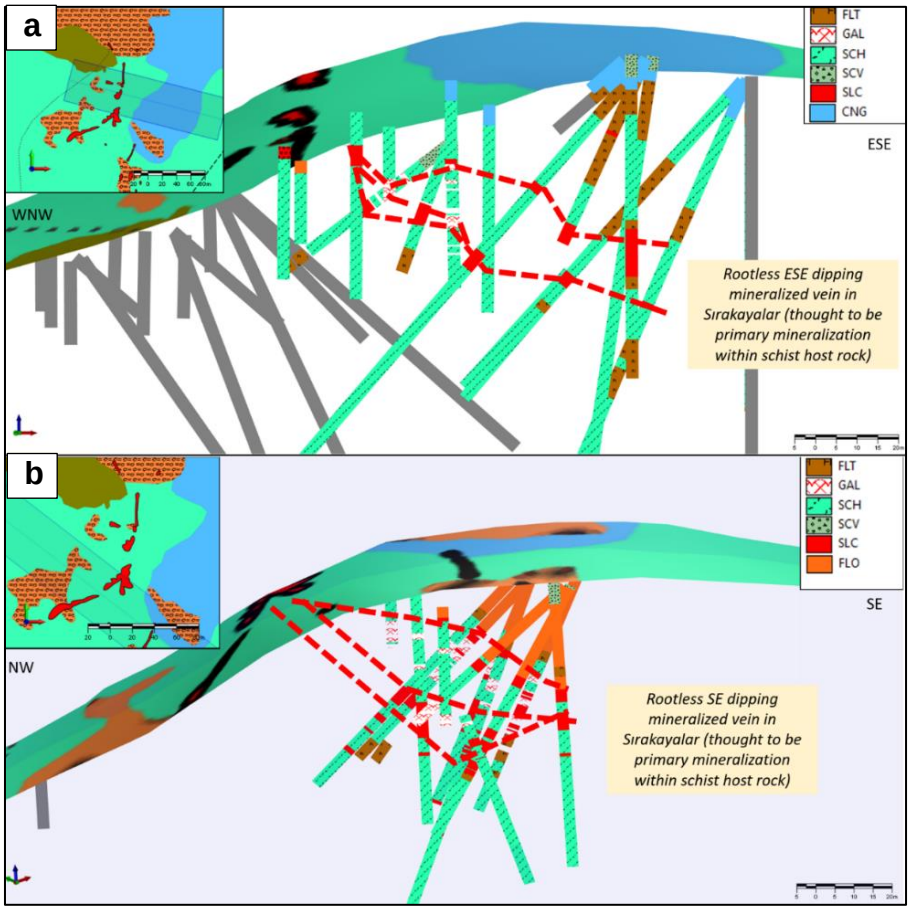

Figure 4.32. Cross-sectional views of the Sırakayalar Sector showing rootless ESE- and SE-dipping boomerang-shaped, mineralized quartz vein within graphitic mica schists. a) WNW-ESE cross-section at the northern part of the vein, b) NW-SE cross-section at the southern part of the vein. Drill holes traces are also shown. Inset shows plan views for each figure.

Figure 4.33. Boulders of mineralized veins displaying epithermal textures within the float/talus material of the Sırakayalar Sector.

An Fe-oxide and clay-rich talus matrix surrounds the disrupted fragments of epithermal veins (Fig. 4.33) that vary in size from a few centimeters up to one meter. Apart from the mineralized vein clasts, fragments of metamorphic and igneous rocks are also present in this material. In Sırakayalar, transportation of the mineralized venis are thought to have occured towards NW and NNE directions when general trend of preserved float/talus zone is considered in that area (Fig. 4.34). An approximately 30- to 50-meters-thick talus zone in this sector is followed by schist basement rocks (Fig. 4.35). The transition from the talus zone to the underlying metamorphic basement is abrupt and is marked by a highly-deformed interval (up to 20 meters) that can be called as a "damage zone". The talus material and the graphitic-muscovitic schists along this boundary are strongly tectonized; both lithologies are highly-sheared, brecciated, with well developed fault gouge (Fig. 4.36). Consequently, core recoveries are quite low. Brecciated material locally includes fragments of vein quartz (Figs. 4.9b and 4.36). This suggests that the contact between talus and schist is not only tectonic in nature, but it also may have facilitated emplacement of some of the epithermal veins at Sırakayalar. Mineralized veins also appear below the talus-schist contact for about 15 meters, following which schist is barren of any economic mineralization.

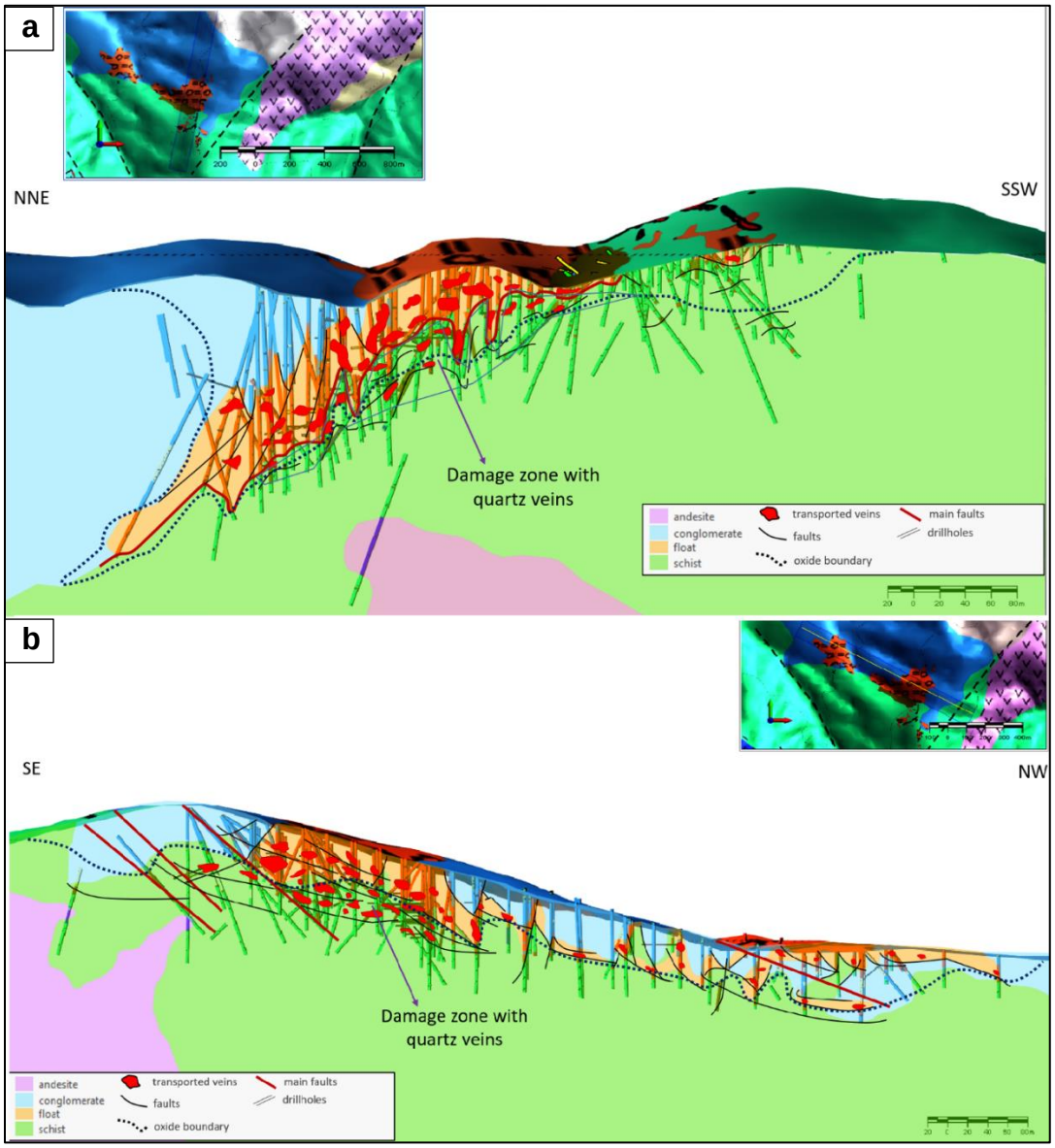

Figure 4.34. a) NNE-SSW and b) SE-NW cross-sectional views of the Sırakayalar Sector showing float/talus material containing mineralized quartz veins and the underlying basement metamorphic units. Shallowly-dipping faults cross-cut both the talus and the metamorphic basement, and controlled transportation of mineralized veins towards NE directions.

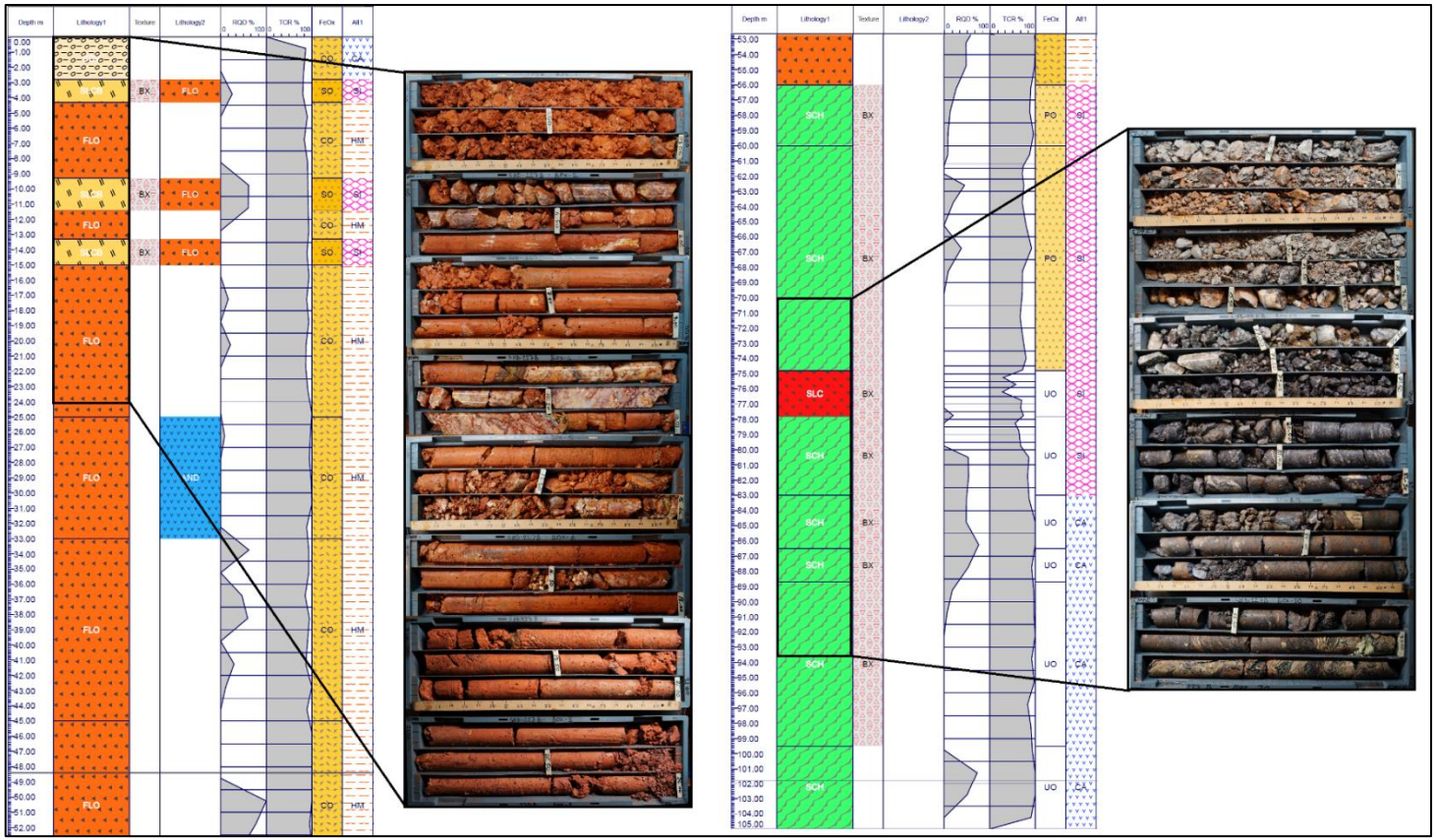

Figure 4.35. Strip-log for SHD-227B, SCV (Sedimentary cover), SCH (Schist), FLO(Talus), SLCB (Quartz Vein Block), BX (Brecciated), CO (Completely Oxidized), PO (Partially Oxidized), SO (Strongly Oxidized), UO (Unoxidized), SI (Silicification), HM (Hematized), CA (Carbonated), RQD (Rock Quality Designation), TCR (Total Core Recovery).

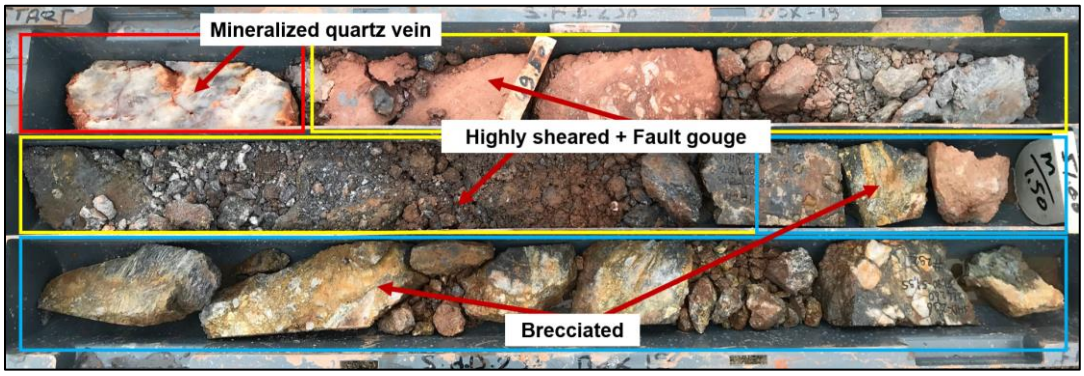

Figure 4.36. A core box photograph from SHD-236 (49.00-52.00 m) showing strongly tectonized damage zone between oxidized talus zone and graphitic schist with mineralized veins bearing, highly sheared, fault gouge and brecciated intervals.

Mineralized veins at Sırakayalar show many similarities with Karatepe in terms of ore and gangue mineralogy and textural characteristics suggesting contemporaneous formation. Episodic hydrothermal activity in Sırakayalar resulted in development of a variety of vein textures from early massive crystalline to later bladed, crustiform and banded-colloform, brecciated, comb, and cockade textures. Although gold-silver mineralization was encountered in most paragenetic stages, intervals with increasing sulfide contents (mainly as pyrite and arsenopyrite) contain the highest grade intervals.

Drill core observations combined with assay results revealed that significant Au and Ag concentrations are mainly associated with paragenetic stages characterized by bladed, brecciated, colloform-banded, and crustiform quartz textures. However, massive crystalline textures observed at the macroscopic scale (identified as sacchraoidal and mosaic/jigsaw textures petrographically) are generally associated with relatively lower Au and Ag grades (Fig. 4.37).

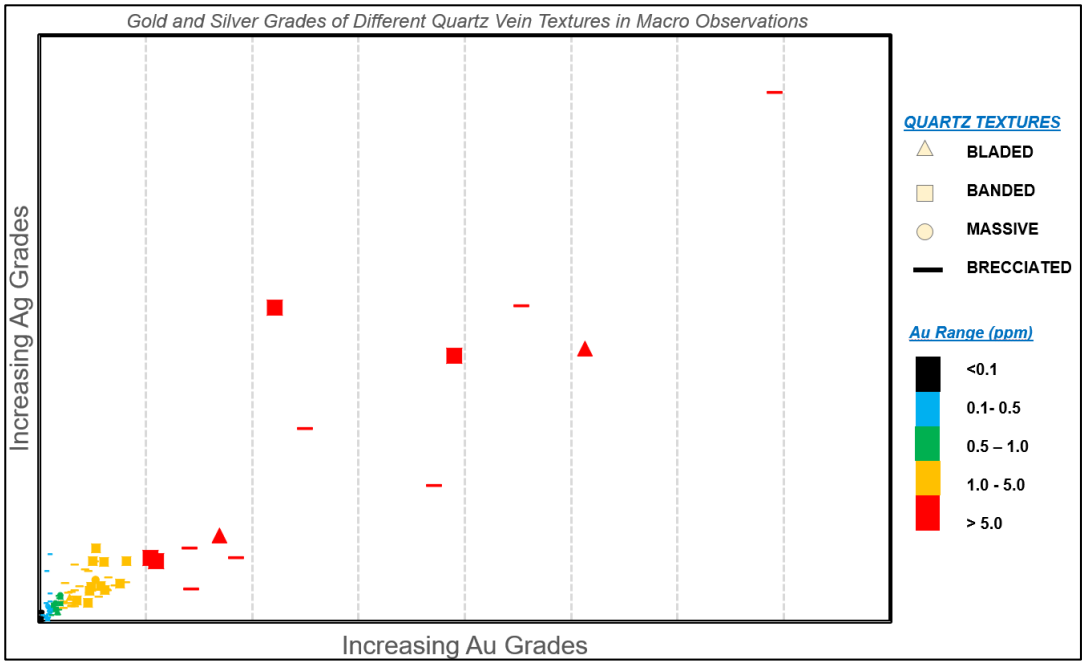

Figure 4.37. Relationship between Au and Ag grades and macro-textures of quartz veins from the Sırakayalar Sector as observed along 55 drill holes with 268 intervals.

4.2.2.1 Microscopic Quartz Textures in Sırakayalar

Most of the mineralization at the Sırakayalar Sector includes transported material with quartz vein and wall-rock fragments, i.e. hydrothermal veins are not in situ. Although quartz veins could not be observed in their original formation environment, a variety of epithermal-style quartz-dominant vein textures can still be well observed (Fig. 4.38). In addition, the faulted contact between the shallow talus material and underlying schists, and the upper levels of the schists contain Au and Ag mineralization. Despite its eroded and strongly-deformed nature, mineralization is mostly unoxidized and is represented by sulfide-bearing zones within quartz-rich veins and breccias (Fig. 4.39). Drill core investigations and sampling were performed on drill holes SHD-249A, SHD-277B, SHD-236, and SHD-143 (Fig. 4.40), and sampling was mainly focused on the talus zone with transported quartz veins, as well as on the sulfide mineralized damage zone.

Quartz textures at Sırakayalar have been broadly classified into three paragenetic stages as: (1) massive crsytalline to bladed quartz and brecciated quartz, (2) crustiform-comb quartz, and finally (3) cockade-comb quartz (Fig. 4.41).

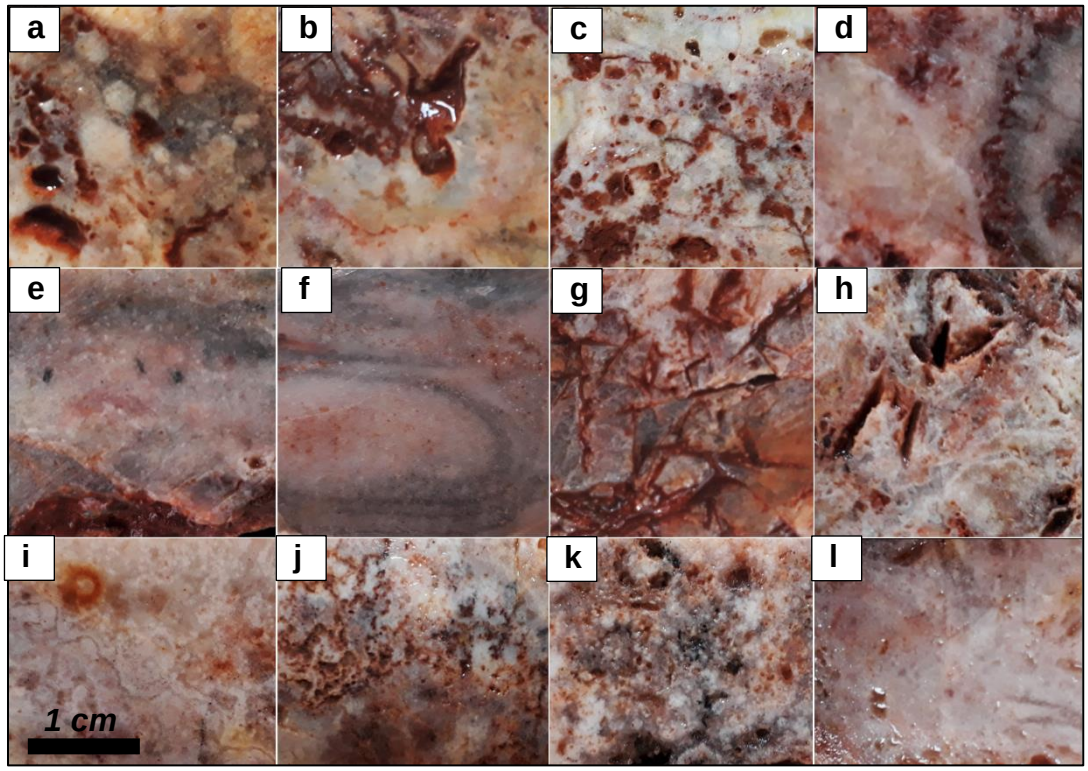

Figure 4.38. Photographs of core samples showing details of various quartz textures from quartz vein fragments within the talus zone at Sırakayalar. a) Brecciated vein (drill hole SHD-227B, 11.00 m depth), b) Partly oxidized vein displaying lattice-bladed texture (drill hole S227B, 11.00 m depth)s, c) Massive crystalline texture with vugs (SHD-227B, 13.60 m depth), d) S236-2300 sample showing massive crystalline texture, e) Massive crystalline texture (SHD-236, 25.70 m depth), f) Massive and sulfidic banded quartz texture with disseminated pyrite mineralization (SHD-236, 27.35 m depth), g) Lattice-bladed texture (SHD-236, 34.90 m depth), h) Bladed texture (SHD-143, 50.05 m depth) i) S143-5580 sample showing colloform banded texture, j) Saccharoidal texture (SHD-143, 55.80 m depth), k) S143-5770 sample showing sacchraoidal texture, l) Ghost-bladed and massive crystalline textures (SHD-143, 49.00 m depth).

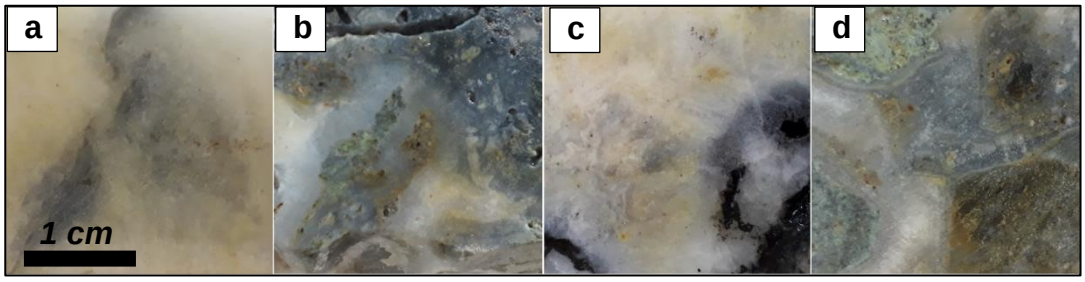

Figure 4.39. Photographs of core samples showing different quartz textures from Sırakayalar quartz veins within unoxidized damage zone a) Massive crystalline texture (SHD-227B, 75.60 m depth), b) Brecciated texture (SHD-227B, 76.75 m depth), c) Massive crystalline and ghost bladed textures (SHD-236, 67.70 m depth), d) Brecciated and cockade textures (SHD-227B, 75.70 m depth).

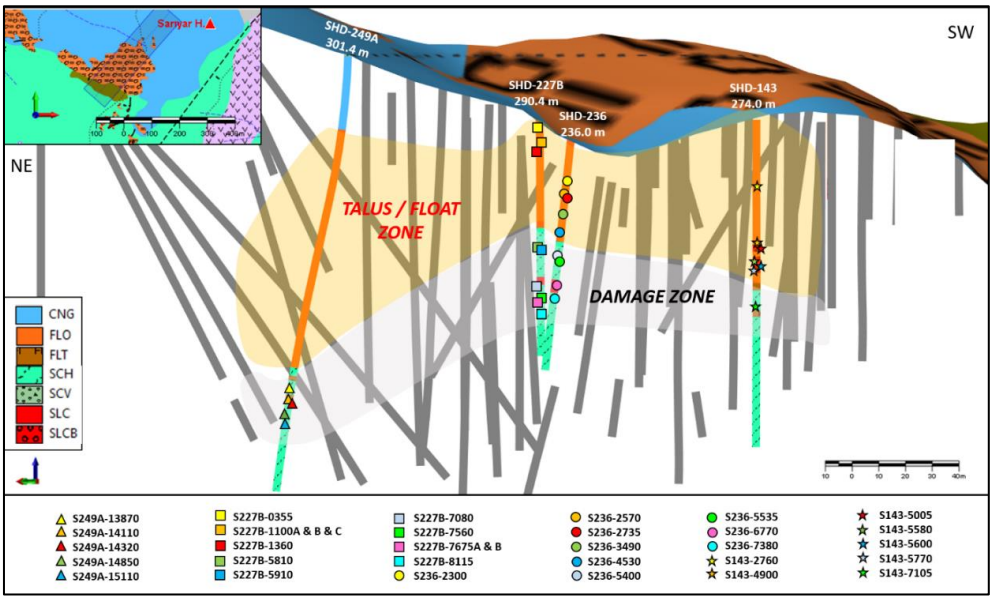

Figure 4.40. NE-SW cross-section view showing examined drillholes (SHD-249A, SHD-227B, SHD-236 and SHD-143) sample locations from talus/float zone and damage zone in Sırakayalar area.

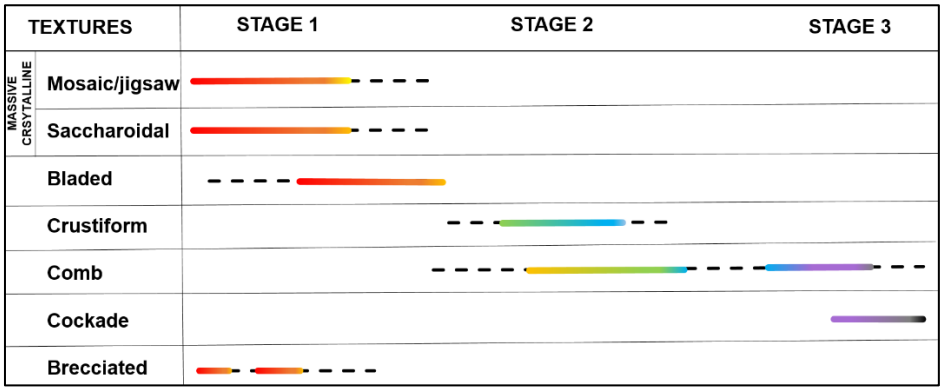

Figure 4.41. Quartz stages controlling the mineralization in Sırayalar Sector.

Stage 1: Massive Crsytalline to Bladed Quartz

Similar to the Karatepe Sector, the earliest paragenetic stage at Sırakayalar is represented by sacchraoidal and mosaic/jigsaw quartz, which appears as massive siliceous veins at the drill core. Mosaic/jigsaw texture is characterized by aggregates of crystalline quartz that diplays interpenetrating quartz grain boundaries (Figs. 4.42a and 4.42b). In the veins, mosaic/jigsaw quartz is generally medium-grained. Saccharoidal quartz, on the other hand, was observed as sugary, massive quartz, and is characterized by replacement of earlier quartz in mineralized veins (Fig. 4.43). These occur as fine- to medium-grained quartz crystals in the veins. Some saccharoidal quartz was also identified as vug infill, a common occurrence in the Sırakayalar Sector. Various forms of bladed texture are present at Sırakayalar including lattice-, ghost- and parallel-bladed quartz. Ghost-bladed quartz is represented by aggregates of quartz crystals with superimposed blades, where quartz occupies laths of earlier bladed calcite (Figs. 4.44 and 4.45). Lattice-bladed quartz was observed as intersecting symmetrical seams of quartz crystals with sharp boundaries (Fig. 4.46), whereas aggregates of parallel laths of quartz characterize the parallel-bladed quartz (Fig. 4.45b). Pseudo-acicular or radiated quartz forming arrays of acicular quartz crystals (Fig. 4.47) is a relatively less common type of bladed texture at Sırakayalar.

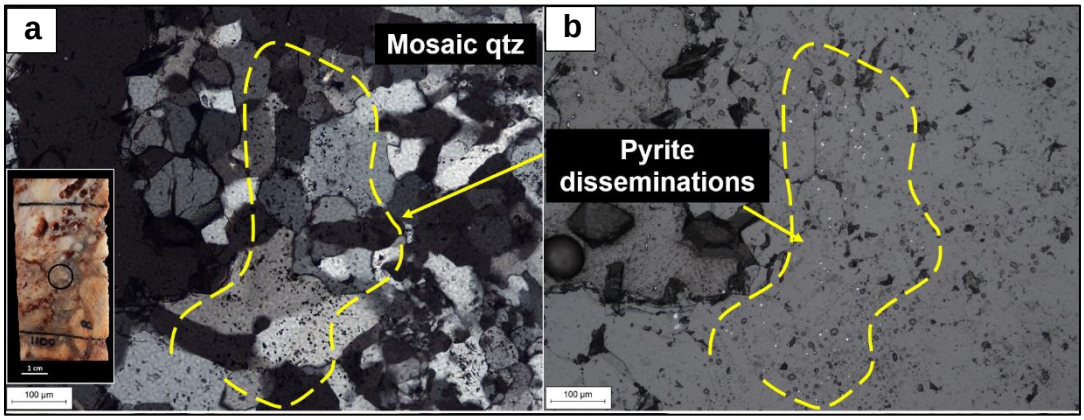

Figure 4.42. Microphotographs showing a) and b) Mosaic quartz with fine-grained disseminated pyrite (drill hole SHD-227B, 11.00 m depth); TL, XPL and RL, PPL images, respectively). (Abbreviations: qtz = quartz; TL = transmitted light; XPL = cross polarized light; RL = reflected light; PPL = plane polarized light).

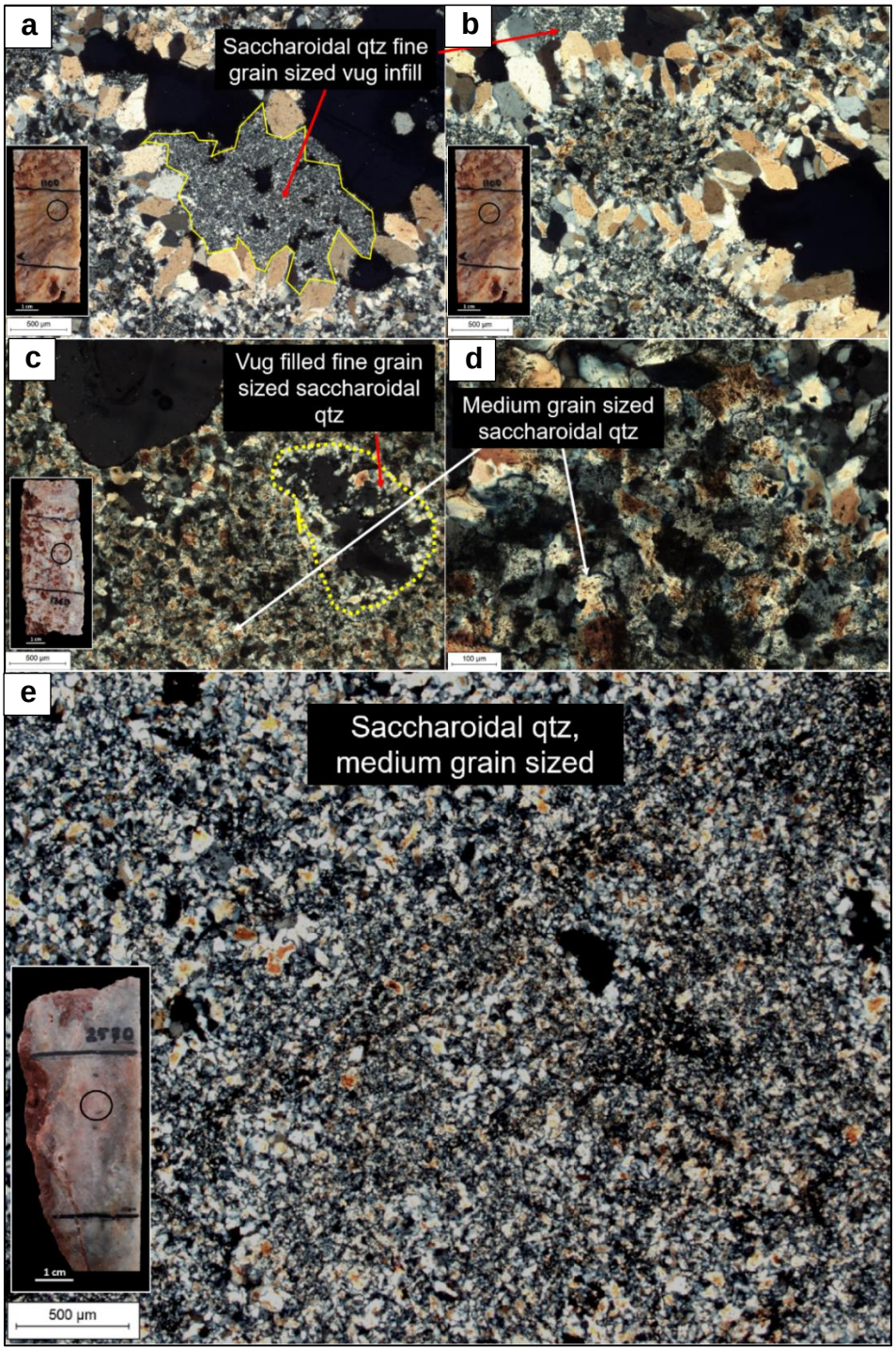

Figure 4.43.Microphotographs of saccharoidal quartz textures from selected samples (TL, XPL images) a) and b) showing vug filled fine grain sized saccharoidal quartz textures (drill hole SHD-227B, 11.00 m depth), c) and d) showing fine and medium grain sized saccharoidal quatz textures (drill hole SHD-227B, 13.60 m depth), d) showing medium sized saccharoidal quartz texture (drill hole SHD-236, 25.70 m depth). (Abbreviations: qtz = quartz; TL = transmitted light; XPL = cross polarized light).

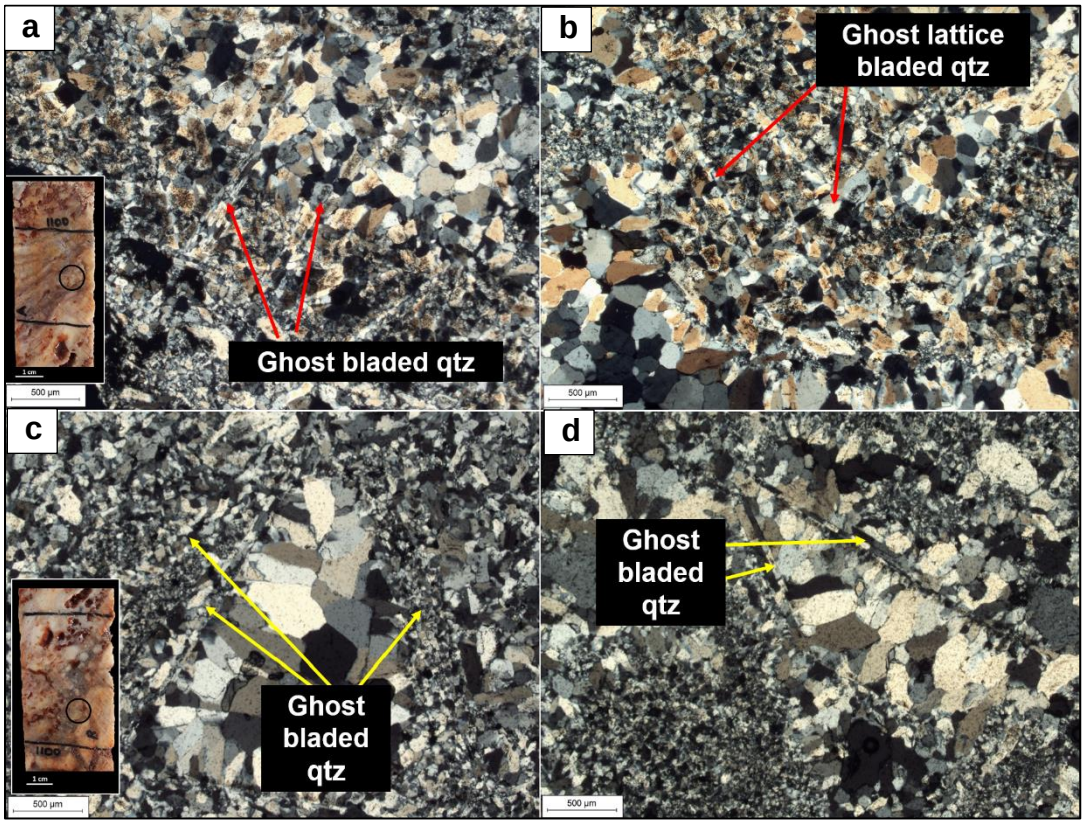

Figure 4.44. Microphotographs (TL, XPL images) of ghost-, lattice, and parallel-bladed quartz. a) and b) ghost- and lattice-bladed quartz (drill hole SHD-227B, 11.00 m depth), c) and d) parallel ghost-bladed quartz (drill hole SHD-236, 67.70 m depth). (Abbreviations: qtz = quartz; TL = transmitted light; XPL = cross polarized light).

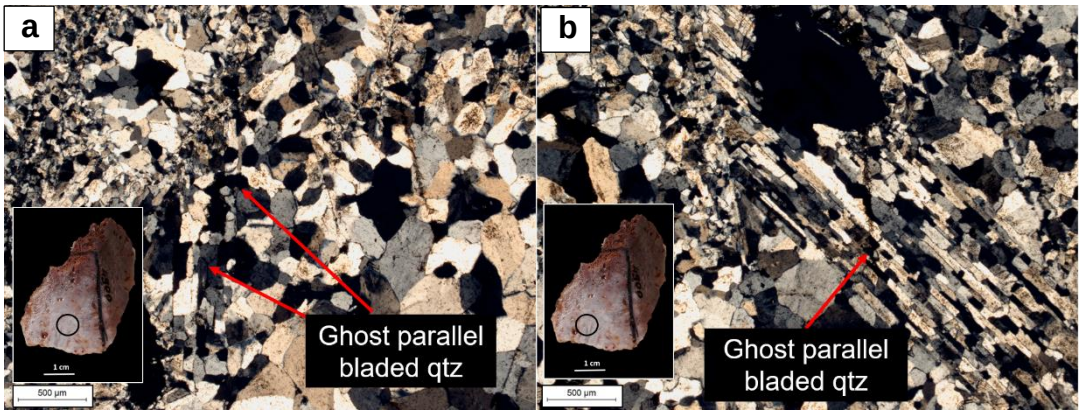

Figure 4.45. Microphotographs (TL, XPL images) of a) ghost-bladed and b) parallel-bladed quartz (drill hole SHD-143, 49.00 m depth). (Abbreviations: qtz = quartz; TL = transmitted light; XPL = cross polarized light).

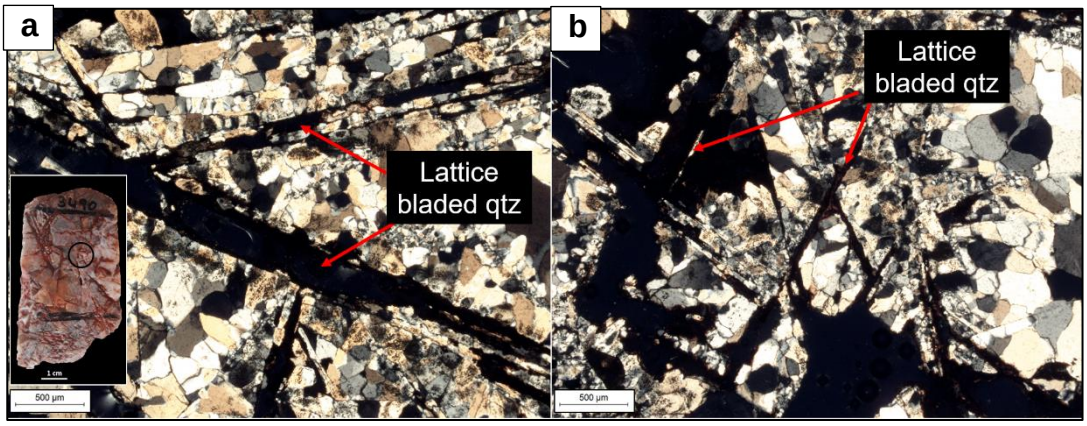

Figure 4.46. Microphotographs (TL, XPL images) of lattice bladed quartz textures from selected sample (drill hole SHD-236, 34.90 m depth) a) and b) showing lattice blades. (Abbreviations: qtz = quartz; TL = transmitted light; XPL = cross polarized light).

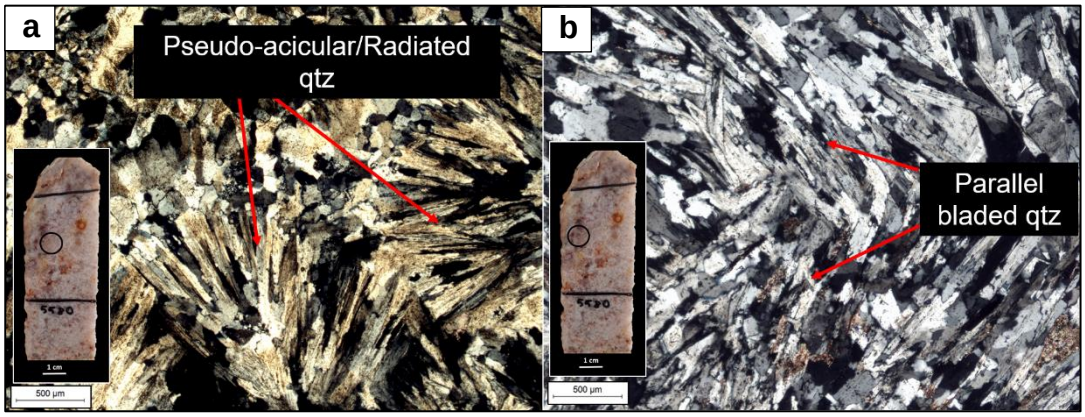

Figure 4.47. Microphotographs (TL, XPL images) of pseudo-acicular or radited quartz texture and parallel bladed quartz texture from selected sample (drill hole SHD-143, 55.80 m depth) a) pseudo-acicular or radiated texture of quartz b) showing ghost parallel bladed texture of quartz. (Abbreviations: qtz = quartz; TL = transmitted light; XPL = cross polarized light).

Stage 1: Brecciated Quartz

At least two distinct stages of syn-mineralization brecciation in quartz was observed as hematite-rich, silica-poor (hematite>silica) matrixed breccias and silica-rich, hematite-poor (silica>hematite) matrixed breccias (Fig. 4.48). Brecciation phases in Sırakayalar mineralized vein fragments can also be observed at the micro-scale (Fig. 4.49); however, these two phases are not easily distinguishable petrographically. Thin section observations showed that brecciation is characterized mostly by massive crystalline quartz phases and even single quartz crystals set within a

siliceous matrix. For this reason, brecciation was interpreted to account for stages between massive crystalline and later bladed phases.

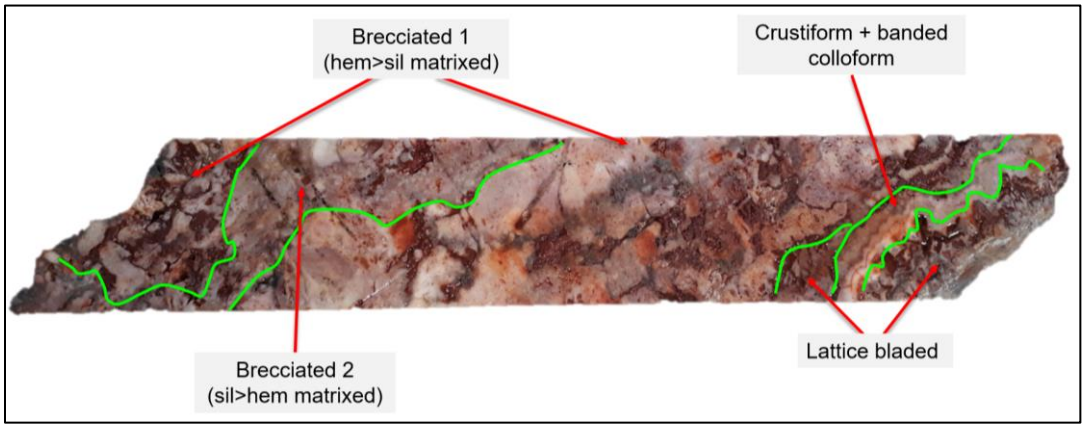

Figure 4.48. Drill core sample of a vein fragment from Sırakayalar talus zone (drill hole SHD-227B, 11.00–11.50 m depth). Early lattice-bladed texture followed by crustiform/colloform-banded quartz, and two phases of brecciation with early massive crystalline quartz in the clasts surrounded by hematitic (hem) or siliceous (sil) matrix. Drill core is approximately 6.3 cm in diameter (HQ).

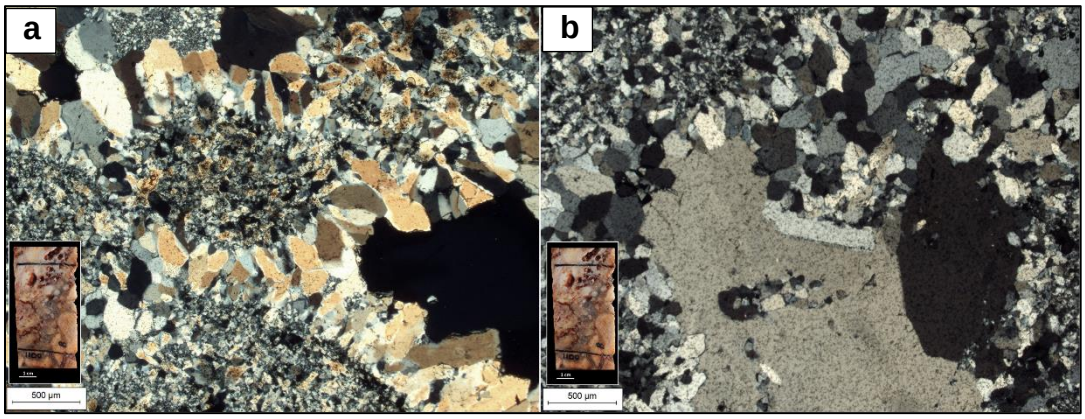

Figure 4.49. Microphotographs (TL, XPL images) of brecciated texture (drill hole SHD-227B, 11.00 m depth). a) Breccia with rounded, silicified clasts surrounded by a siliceous matrix, and partly open vug to lower right, b) large quartz clast surrounded by a siliceous matrix. (Abbreviations: TL = transmitted light; XPL = cross polarized light).

Stages 2 and 3: Crustiform-Comb and Cockade-Comb Quartz

In Sırakayalar, another mineralized quartz phase is represented by crustiform quartz characterized by successive bands of variably-sized quartz including coarse-grained comb quartz and medium-grained saccharoidal quartz (Fig. 4.50a). Cockade texture with concentric bands of variably-sized quartz surrounding rounded to sub-rounded wall-rock clasts is also closely associated with crustiform quartz zones (Fig. 4.50b, Fig. 4.50c). Crustiform and cockade quartz phases are considered as intermediate and late quartz phases in Sırakayalar vein paragenesis, respectively, since they were formed following bladed and massive crystalline quartz, and also later than brecciation.

In addition to these, individual quartz crystals rarely display feathery appearance developed mainly as patches from edges of commonly quartz or less commonly of pyrite crystals. This type of quartz shows radiant extinction under transmitted cross-polarized light (Fig. 4.51).

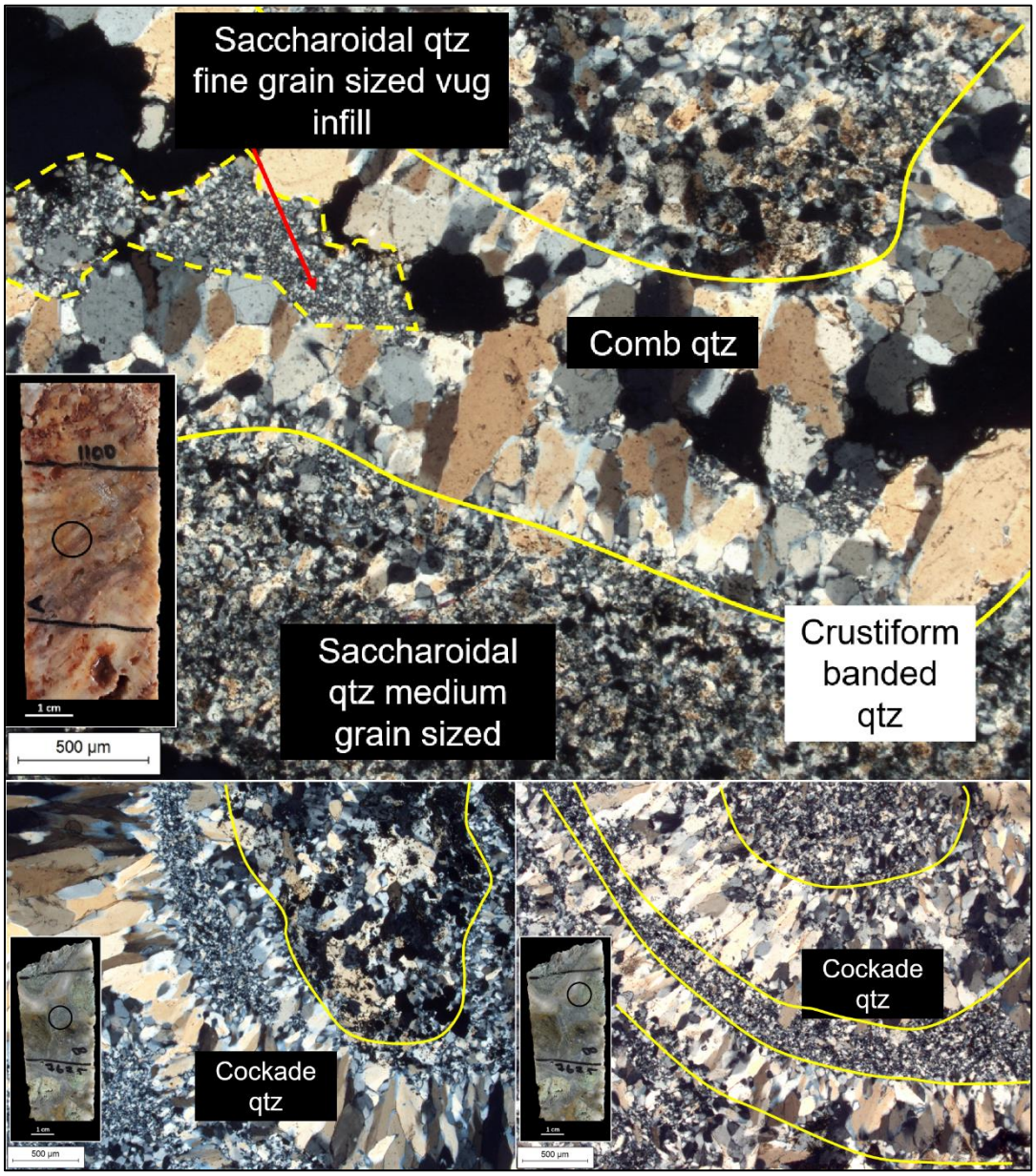

Figure 4.50. Microphotographs (TL, XPL images) of crustiform, comb, and cockade quartz textures from Sırakayalar. a) Successive bands of comb and saccharoidal quartz to form crustiform texture (drill hole SHD-227B, 11.00 m depth), b) and c) Concentric bands of cockade quartz overgrown partly to completely silicified wall-rock clasts (drill hole SHD-227B, 76.75 m depth). (Abbreviations: qtz = quartz; TL = transmitted light; XPL = cross polarized light).

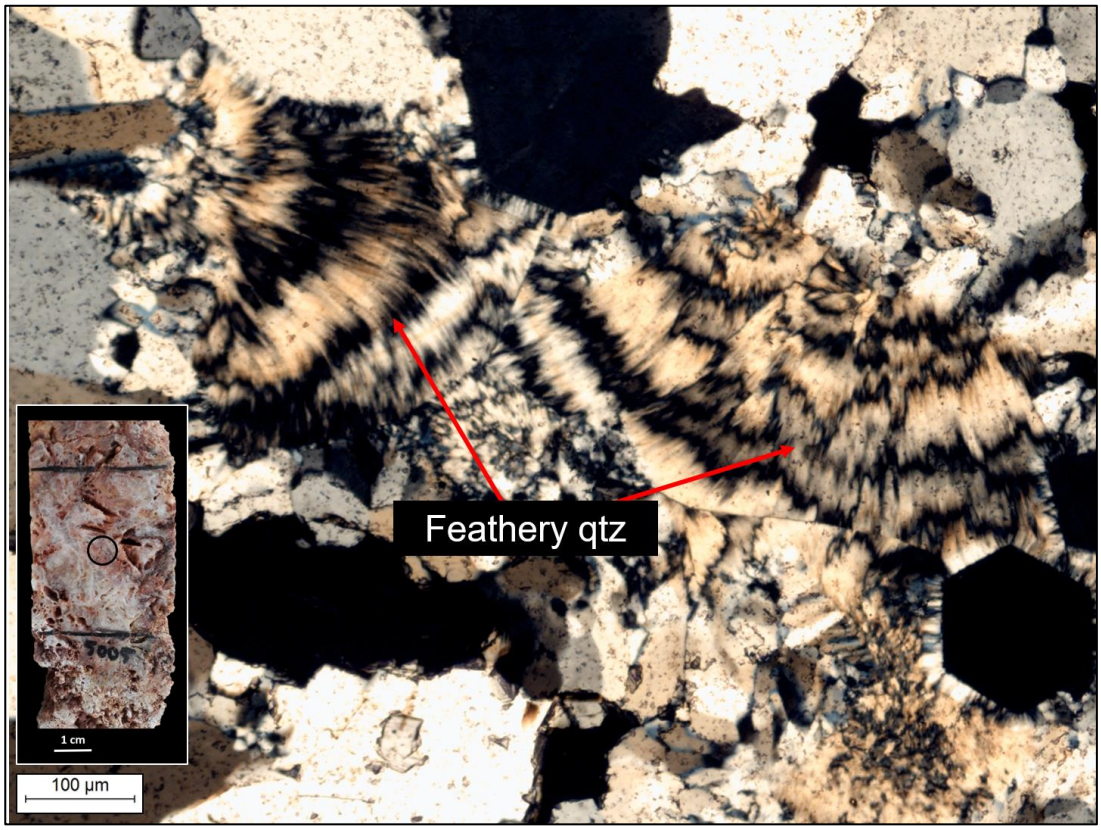

Figure 4.51. Microphotograph (TL, XPL image) showing feathery quartz developed mainly as patches from edges of commonly quartz or less commonly of pyrite crystals (drill hole SHD-143, 50.05 m depth). (Abbreviations: qtz = quartz; TL = transmitted light; XPL = cross polarized light).

4.3 Ore Mineralogy

4.3.1 Karatepe Ore Mineralogy

In the Karatepe Sector, epithermal vein-related Au and Ag mineralization is associated with various quartz-dominant phases. Mineralized veins and wall-rocks of the Karatepe Sector display a simple ore mineral assemblage. Veins and breccias are generally low in sulfide minerals (5–15 vol.%), predominantly consist of Fe-sulfides, and typically lack base metal sulfides. Gold occurs either as native gold or as electrum. Pyrite is the most abundant sulfide mineral both in the veins and also in the metamorphic and igneous wall-rocks (Fig. 4.52). In the wall-rocks, it usually occurs as fine- to medium-grained disseminations, and particularly in the mica schist

it forms aggregates along foliation planes. Native gold and electrum were primarily observed as liberated from weathered/oxidized pyrite (Figs. 4.53 and 4.54), as fine-grained crystals between fine- and medium-grained mosaic/jigsaw quartz (Fig. 4.53), as between medium-grained mosaic, gray quartz veins/veinlets (Figs. 4.55 and 4.56) associated with ductile deformation. Native gold and electrum can be associated with sulfide-rich fluids forming pyrite and arsenopyrite. Arsenopyrite occurs alongside pyrite as euhedral rhombic or as acicular, lath-like crystals (Figs. 4.57 and 4.58). Relatively high Au and Ag grades are mostly related with Stage-1 quartz phase including massive crystalline quartz characterized by mosaic/jigsaw and saccharoidal textures under the microscope. Breccias containing Stage-1 quartz are also associated with Au mineralization. At shallow depths (<30 m), hematite and goethite are common oxidation products after pyrite and arsenopyrite (Fig. 4.53). These supergene phases locally contain inclusions of native gold, suggesting presence of gold in pyrite either as sub-microscopic grains or in solid-solution.

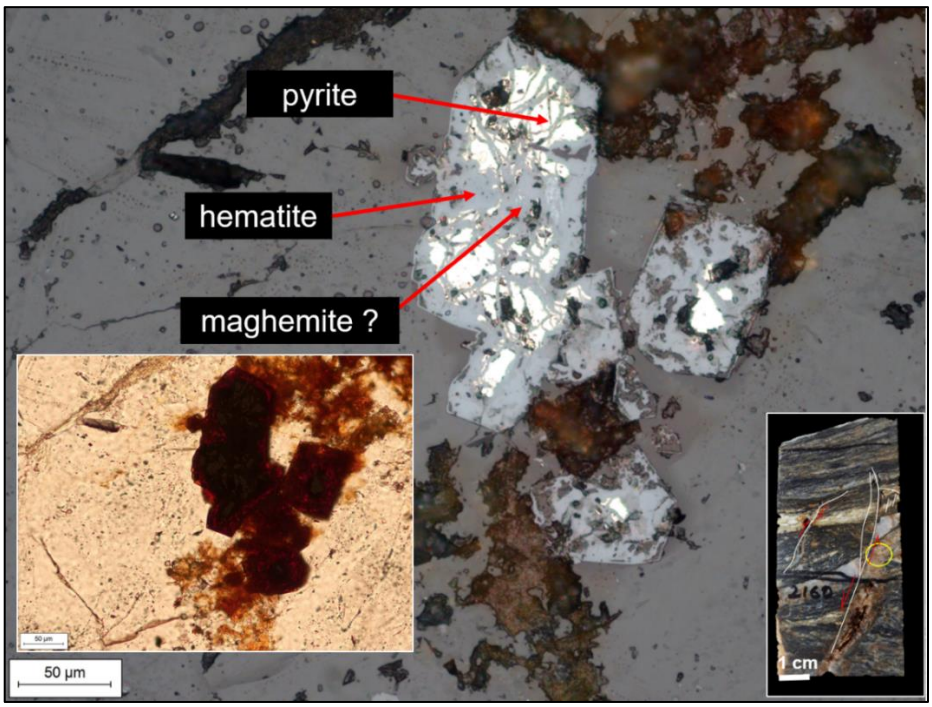

Figure 4.52. Microphotographs of selected sample (drill hole SHD-154; depth 21.60 m) showing comb quartz vein with hematite and possibly maghemite partially replaced pyrite (main image RL, PPL image; inset TL, PPL image). (Abbreviations: TL = transmitted light; RL = reflected light; PPL = plane polarized light).

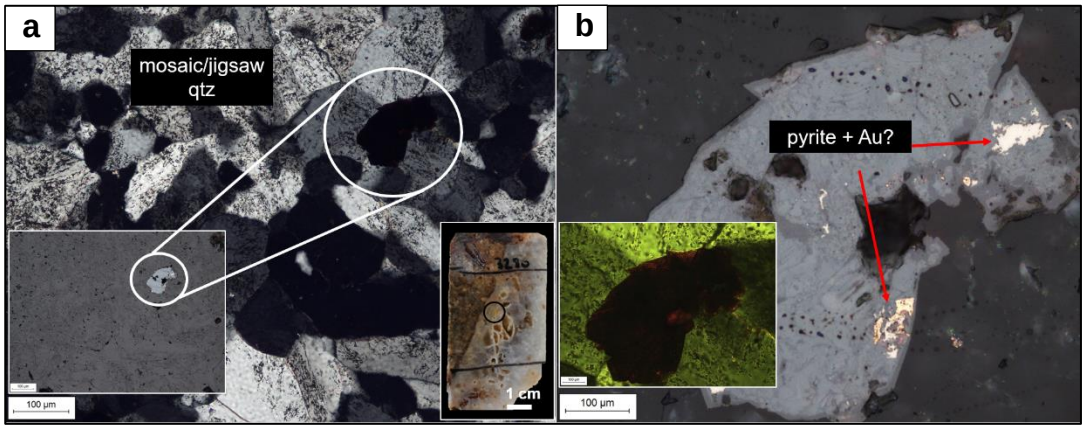

Figure 4.53. Microphotographs of a) sample (drill hole SHD-138, 32.30 m depth) showing mosaic quartz including and weathered pyrite (opaque) (TL, XPL images), and b) enlarged portion of the area highlighted in (a) with inclusions of native gold and relict pyrite. Pyrite almost completely oxidized to hematite and goethite. (Abbreviations: qtz = quartz; TL = transmitted light; XPL = cross polarized light).

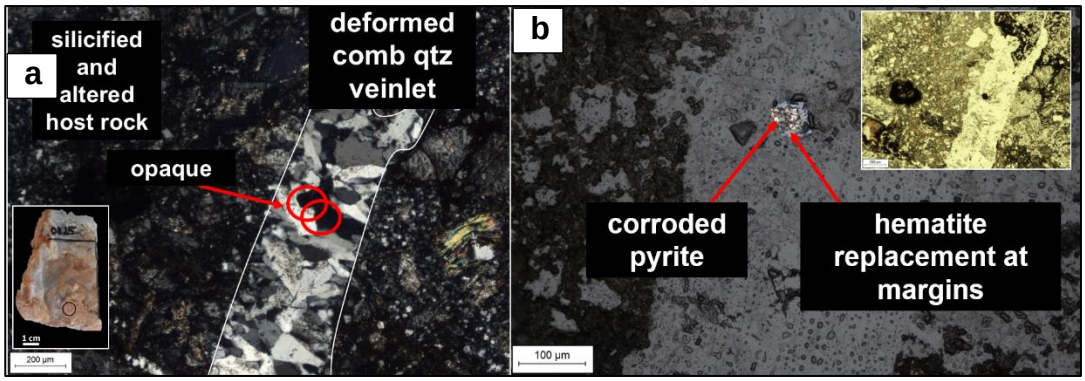

Figure 4.54. Microphotographs of a) sample (drill hole SHD-154, 8.25 m depth) showing comb quartz veinlet with hematite after pyrite (as opaque grains; TL, XPL image), b) enlarged portion of area highlighted in (a) with corroded pyrite (RL, PPL image). (Abbreviations: qtz = quartz; TL = transmitted light; XPL = cross polarized light; RL = reflected light; PPL = cross polarized light).

In addition, higher Au and Ag grades are often concentrated along intervals that comprise a combination of different quartz textures and particularly in zones with hydrothermal breccias. In SHD-154 drill hole, highlighted intervals (Fig. 4.59) having a combination of saccharoidal, cockade, comb and crustiform quartz textures show pyrite and gold association in quartz (Figs. 4.53 and 4.54). In SHD-138 drill hole, remarkable intervals that display a combination of comb, mosaic/jigsaw, and plumose quartz have abundant arsenopyrite, electrum, pyrite, and native gold in pyrite (Fig. 4.60).

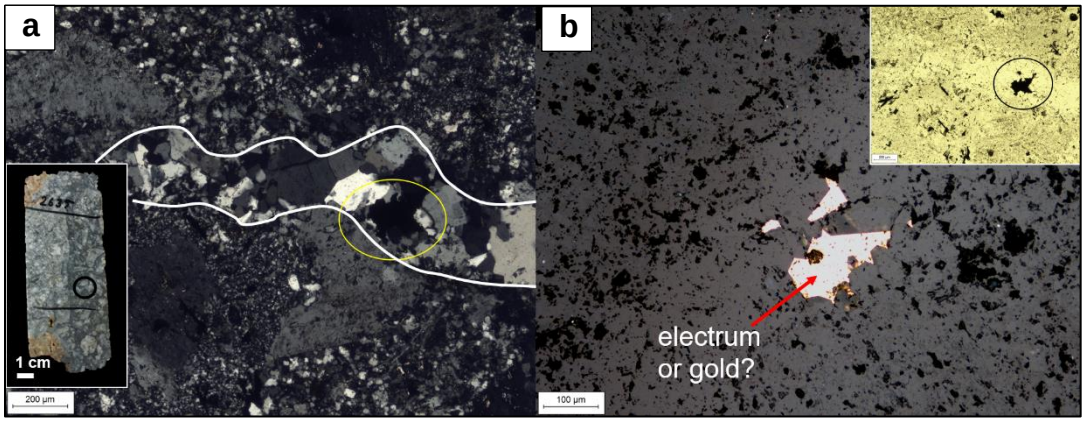

Figure 4.55. Microphotographs of a) sample (drill hole SHD-138, 26.35 m depth) showing wavy mosaic quartz veinlet (TL, XPL image), b) detail of area highlighted in (a) with electrum within mosaic quartz (RL, PPL image). Abbreviations: TL = transmitted light; XPL = cross polarized light; RL = reflected light; PPL = plane polarized light).

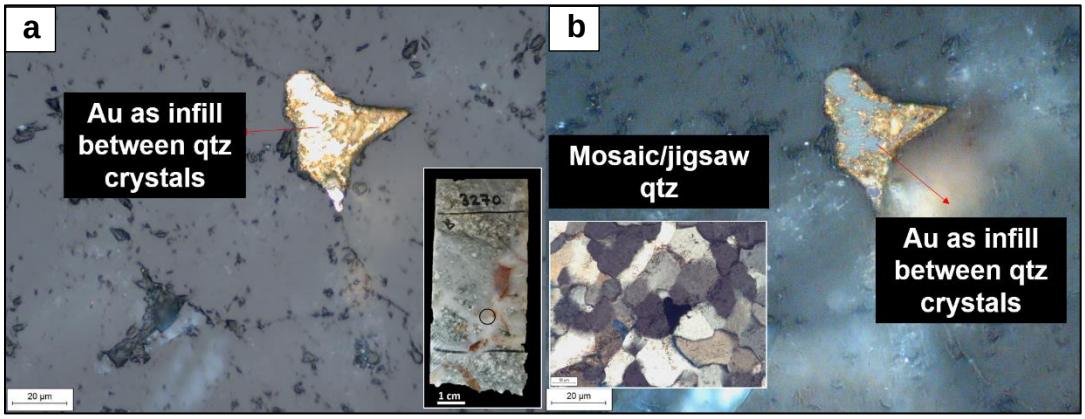

Figure 4.56. Microphotographs from sample (drill hole SHD-154, 32.70 m depth) showing medium grain sized mosaic textured quartz vein including gold (Au) mineral between quartz cystals a) TL, PPL, b) TL, XPL views. (Abbreviations: qtz = quartz; TL = transmitted light; XPL = cross polarized light; PPL = plane polarized light).

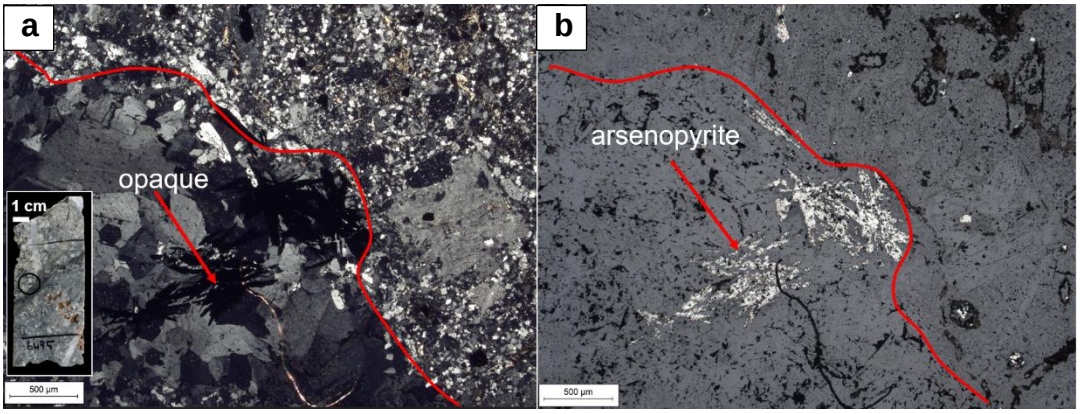

Figure 4.57. Microphotographs of sample (drill hole SHD-154, 64.95 m depth) showing a) deformed possibly mosaic quartz (TL, XPL images) including with b) acicular and radiating arsenopyrite (RL, PPL image). (Abbreviations: TL = transmitted light; XPL = cross polarized light; RL = reflected light; PPL = plane polarized light).

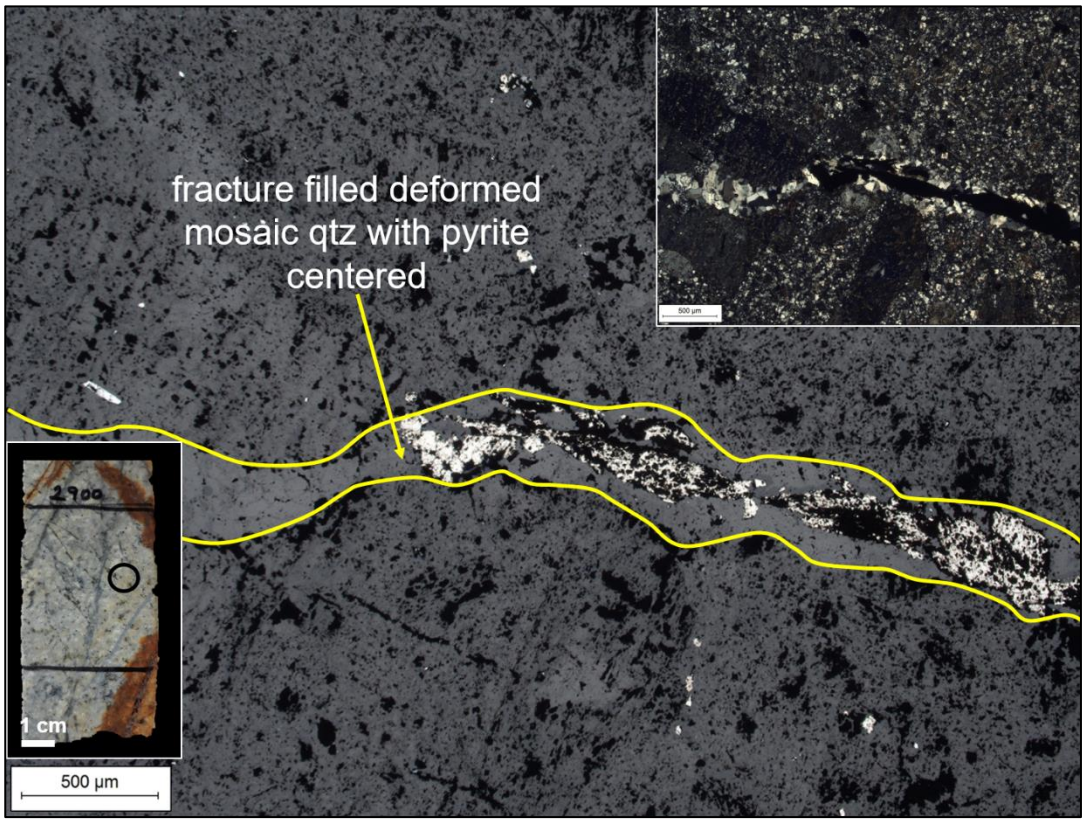

Figure 4.58. Microphotographs of sample (drill hole SHD-154, 29.00 m depth) showing weak stockwork veinlets wth comb to mosaic quartz and pyrite inifill (main image RL, PPL; inset TL, XPL). (Abbreviations: qtz = quartz).

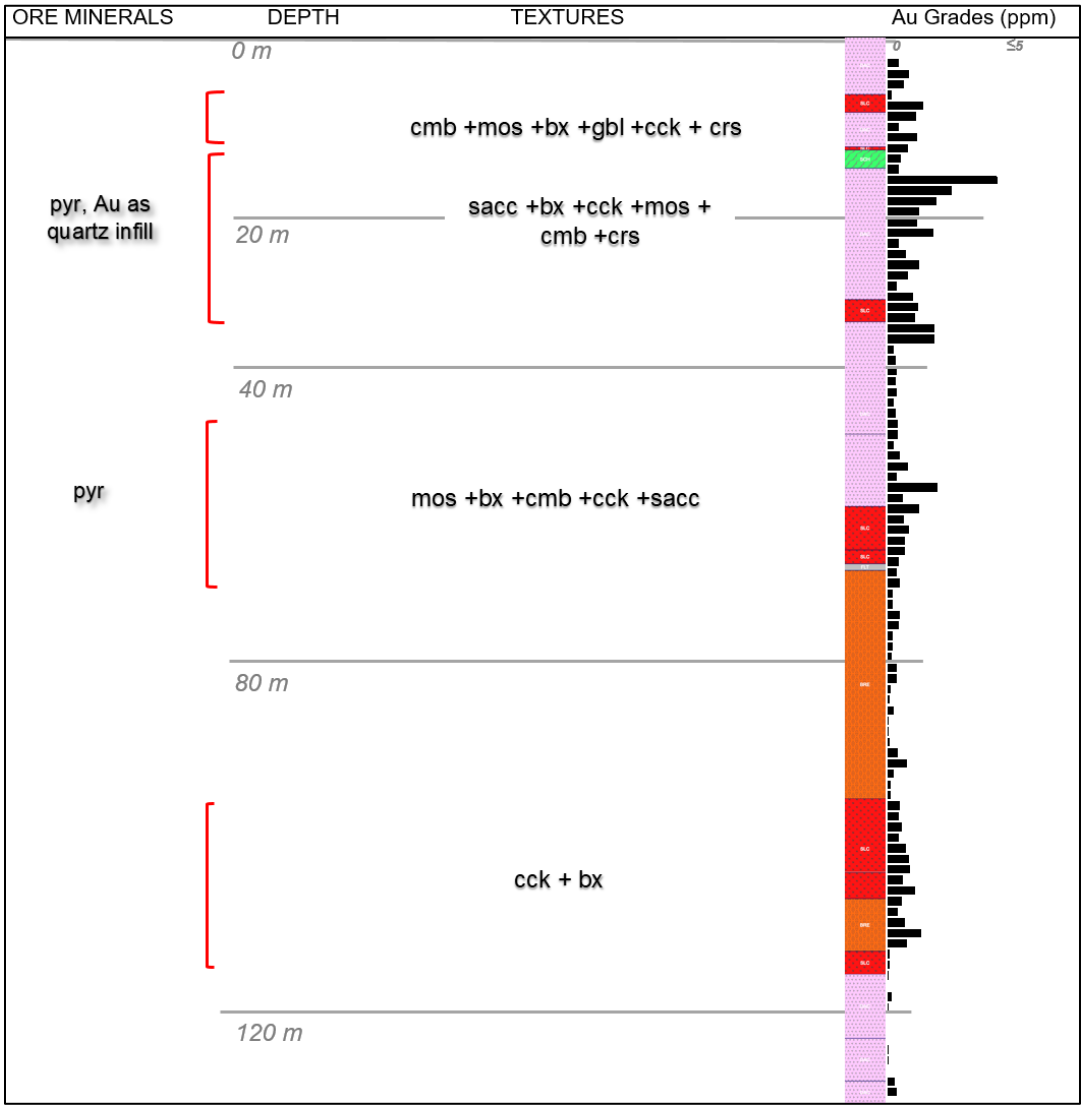

Figure 4.59. Variation of ore mineralogy and textures as well as of Au and Ag grades wth respect to depth in drill hole SHD-154 from the Karatepe Sector. Abbreviations = sacc: saccharoidal; mos: mosaic/jigsaw; bx: brecciation; cmb: comb; sacc: saccharoidal; cck: cockade; crs: crustiform; gbl: ghost-bladed; pyr: pyrite).

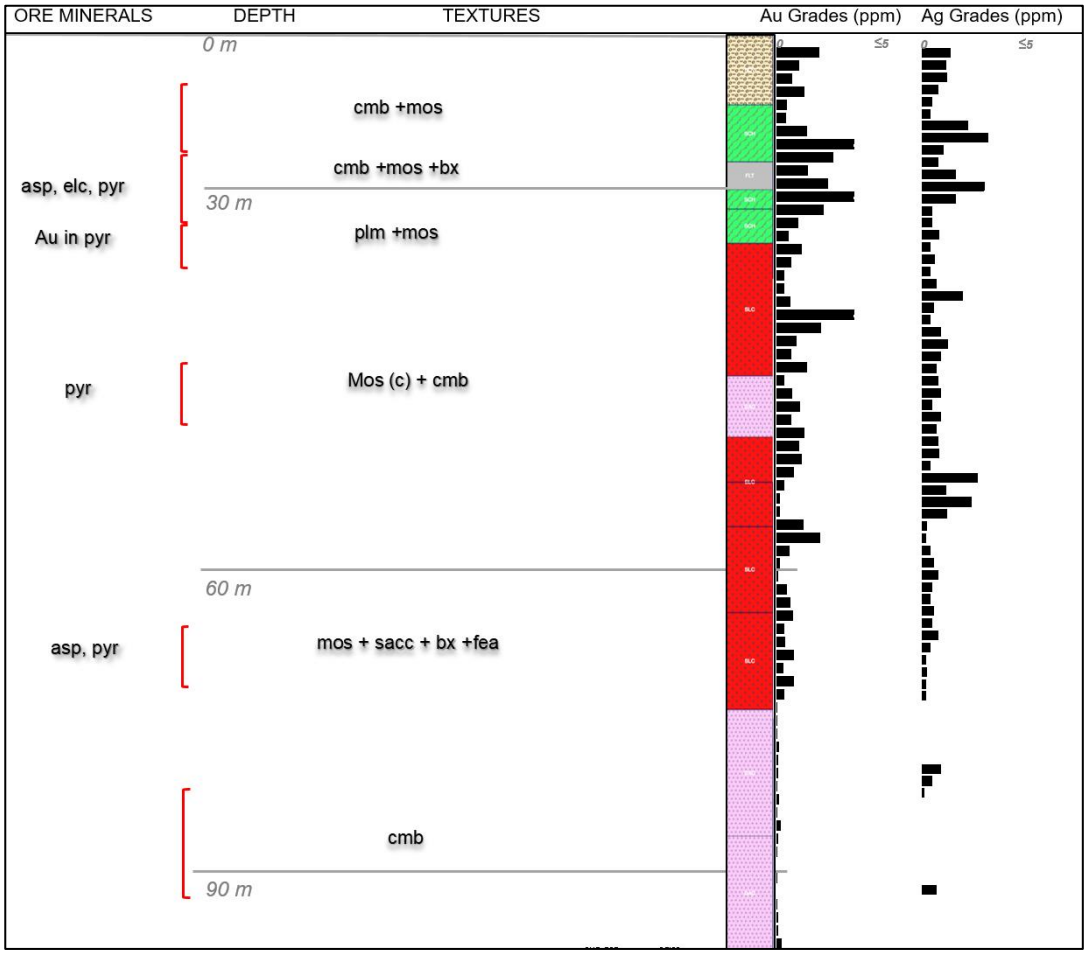

Figure 4.60. Variation of ore mineralogy and textures as well as of Au and Ag grades wth respect to depth in drill hole SHD-138 from the Karatepe Sector. Abbreviations = sacc: saccharoidal; mos: mosaic/jigsaw; bx: brecciation; cmb: comb; fea: feathery; plm: plumose; pyr: pyrite; asp: arsenopyrite; elc: electrum.

4.3.2 Sırakayalar Ore Mineralogy

In the Sırakayalar Sector, epithermal vein-related Au and Ag mineralization is mostly associated with quartz-dominant veins and breccias, as observed in the Karatepe Sector. Petrographic investigation of core samples indicated that Au and sulfide minerals (primarily pyrite and arsenopyrite) are commonly related with replacement-type quartz textures. Native gold was identified in medium-grained saccharoidal quartz, where it interstitally occupies domains in between quartz crystals (Figs. 4.61a–d). Sizes of native gold grains commonly range between 20 and

40 microns, but finer-grained gold particles also do exist. In addition to saccharoidal quartz, gold also shows close spatial relationship to lattice-bladed quartz (Fig. 4.61e). An unidentified low-reflectance mineral with bluish gray color (Figs. 4.62a–b) under plane-polarized light was detected as a late phase after pyrite and arsenopyrite, and was tentatively identified digenite (or another Cu sulfide) likely developed as a replacement mineral after a primary copper phase such as chalcopyrite or tetrahedrite/tennantite (Precejus, 2015). Pyrite often occurs in replacement-type quartz in oxidized float/talus material, and it is commonly hematized due to supergene weathering and oxidation (Figs. 4.63 and 4.62f). Arsenopyrite usually forms acicular, radiating aggregates (Fig. 4.62). It is most prominent in sulfidic damage zone underlying the oxidized talus and sitting a top the basement schists (Fig. 4.64). While sulfide abundance is relatively low ranging between 5 and 10% within the quartz vein fragments in talus zone in Sırakayalar, the faulted talus-schist contact contains higher concentrations of sulfides at 20–25% (up to approximately 30%; Figs. 4.63e and 4.64c).

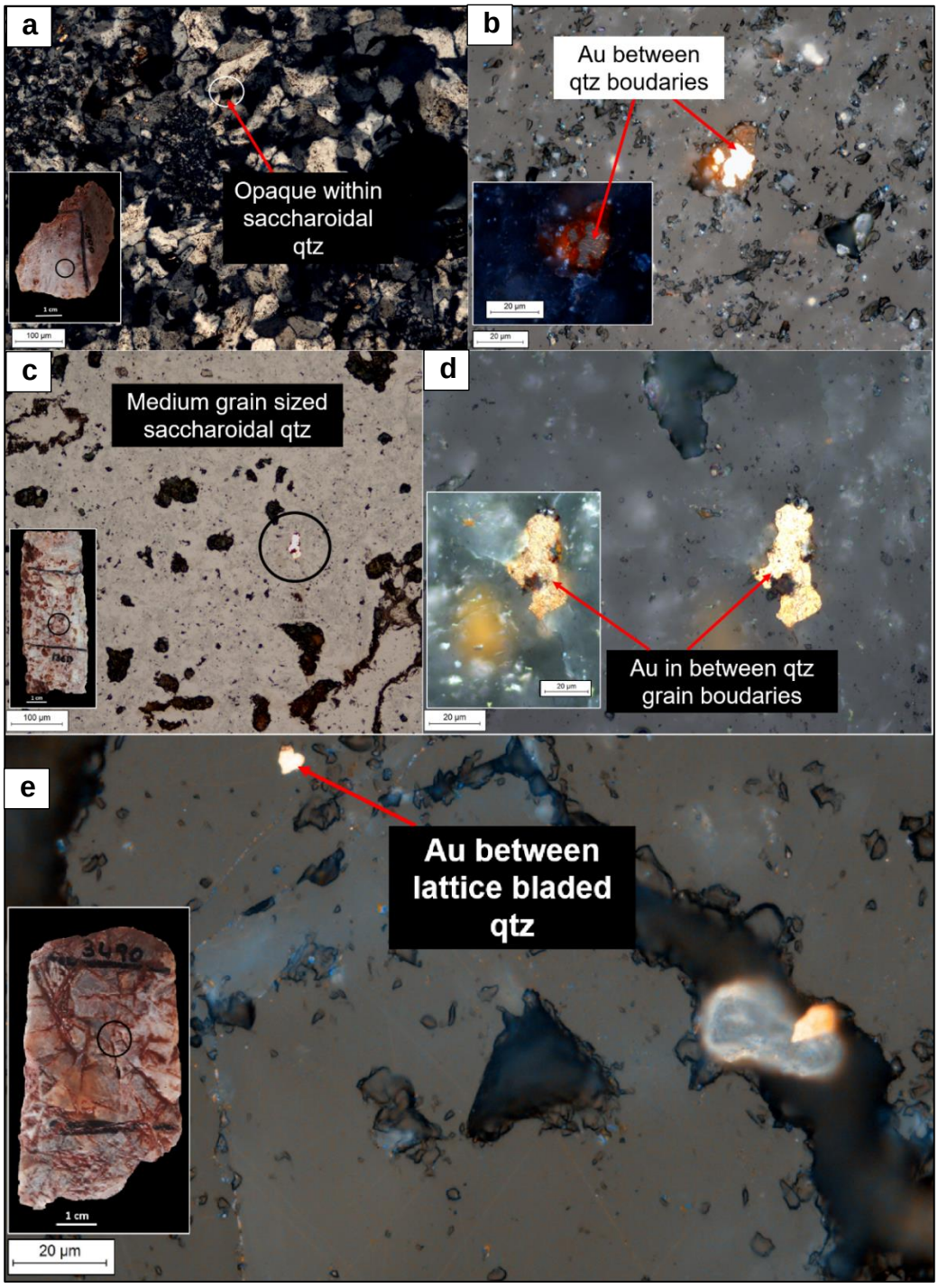

Figure 4.61. Microphotographs of gold mineralized samples in float/talus zone in Sırakayalar. a) Medium-grained saccharoidal quartz (TL, XPL image), b) enlarged portion of the area highlighted in (a) with native gold in saccharoidal quartz (drill hole SHD-143, 49.00 m depth (RL, PPL image), c) Medium-grained saccharoidal quartz (TL, XPL image), d) enlarged portion of the area highlighted in (c) with native gold (drill hole SHD-227B, 13.60 m depth; RL, PPL), e) Native gold in lattice-bladed quartz (drill hole SHD-236, 34. 90 m depth; RL, PPL). (Abbreviations = qtz: quartz; Au: gold; TL = transmitted light; XPL = cross polarized light; RL = reflected light; PPL = plane polarized light).

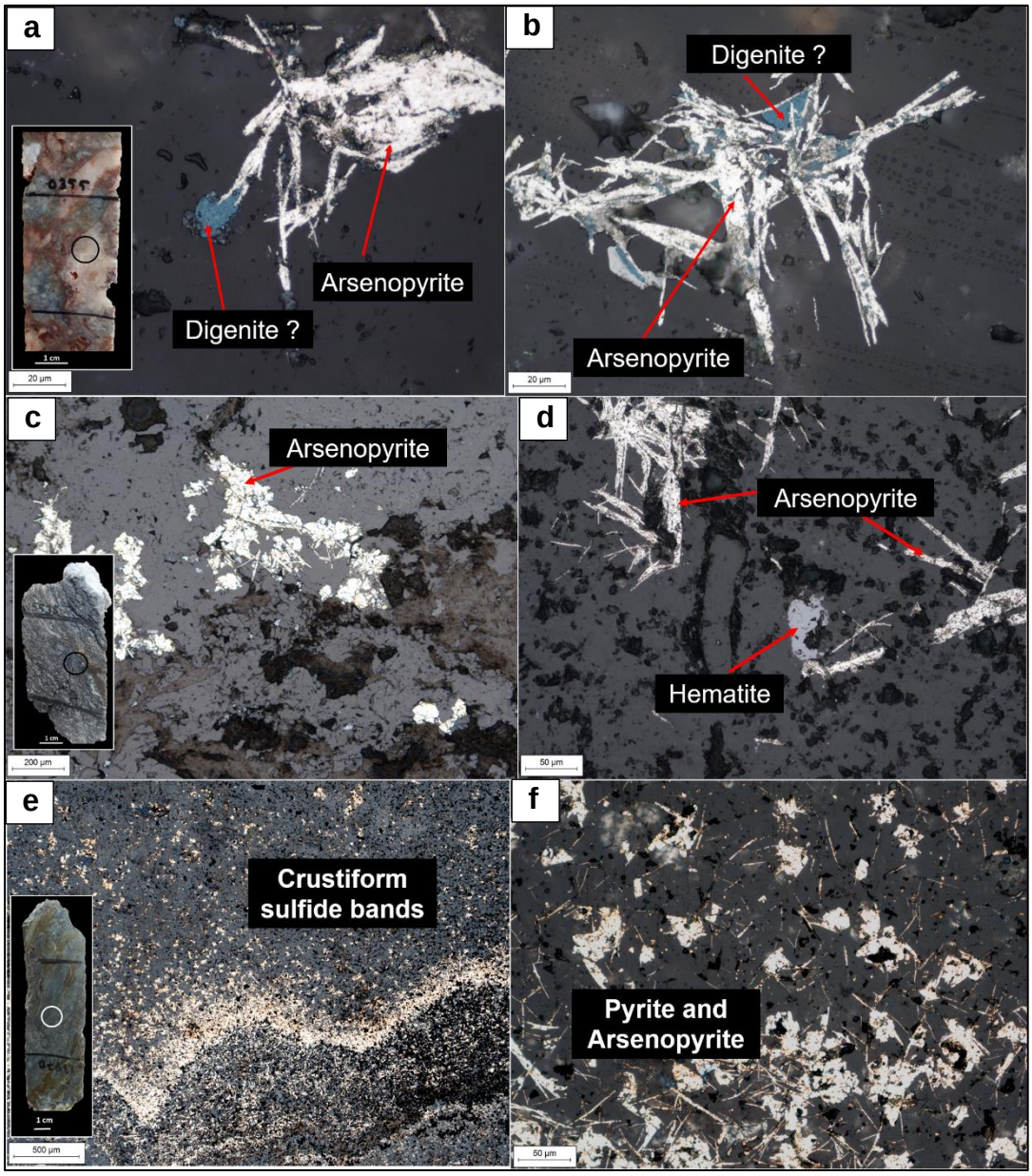

Figure 4.62. Microphotographs (RL, PPL images) of common ore minerals in Sırakayalar. a) and b) Aggregates of star-like radiating arsenopyrite crystals partially replaced by a late, possibly Cu-sulfide phase such as digenite (drill hole SHD-227B, 3.55 m depth). c) and d) Aggregates of star-like radiating arsenopyrite crystals and hematite (after pyrite) sulfidic damage zone (drill hole SHD-236, 55.35 m depth), e) crustiform/colloform sulfide bands containing aggregates of arsenopyrite and pyrite from sulfidic damage zone (drill hole SHD-249A, 138.70 m depth). (Abbreviations: RL = reflected light; PPL = plane polarized light).

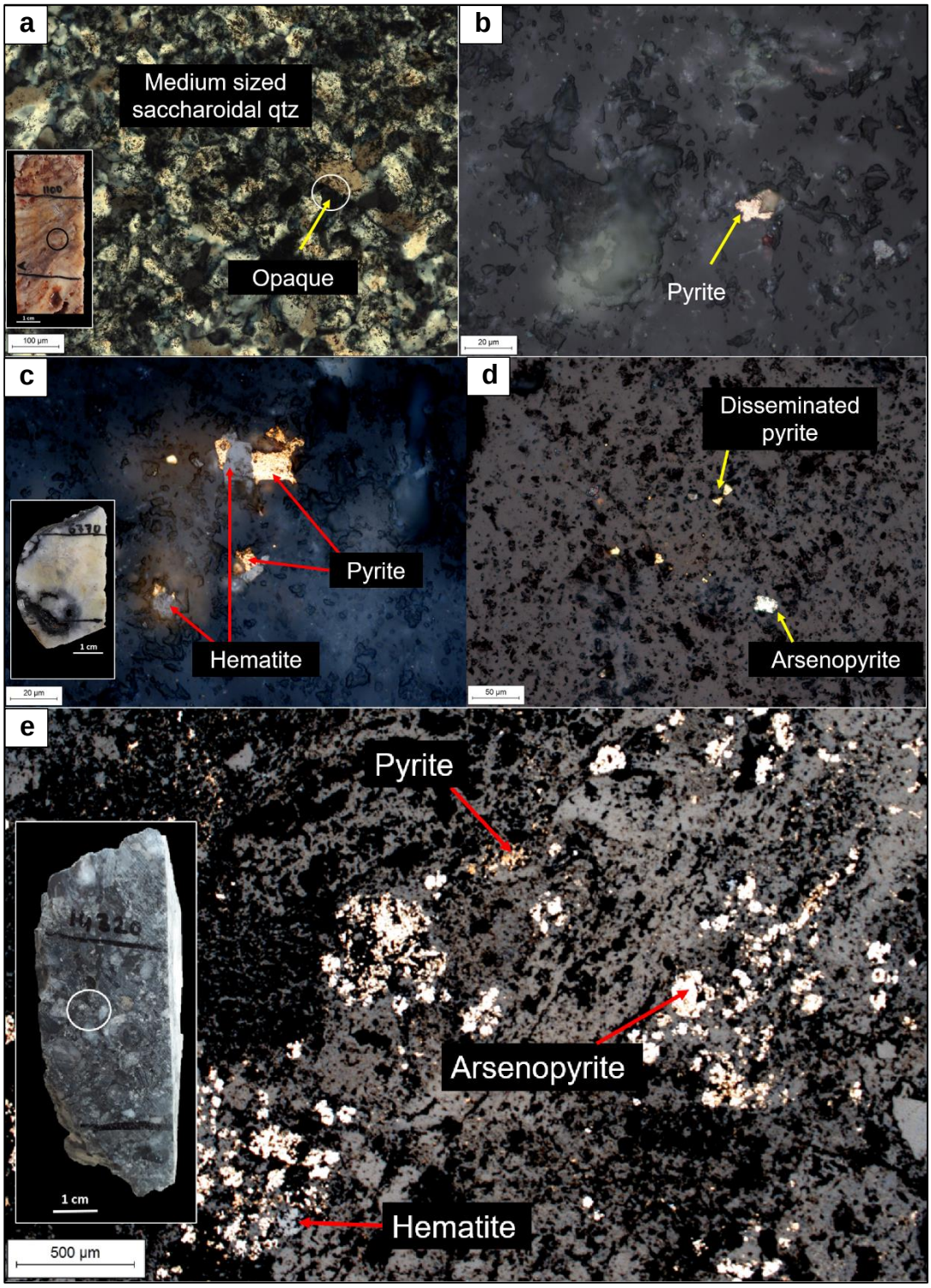

Figure 4.63. Microphotographs of micron sized pyrite mineralization from selected quartz vein samples from float/talus and sulfidic damage zones in Sırakayalar, a) Opaque mineral of pyrite between saccharoidal textured quartz as a band of crustiform texture, (TL, XPL image) (drill hole SHD-227B, 11.00 m depth) b) An pyrite mineralization (RL, PPL image) (drill hole SHD-227B,

11.00 m depth), c) and d) Pyrite with partly hematitized and disseminated arsenopyrite with pyrites (RL, PPL images) (drill hole SHD-236, 67.70 m depth), e) An pyrite and arsenopyrite mineralization (RL, PPL image) (drill hole SHD-249A, 143.20 m depth) (Abbreviations: qtz = quartz; TL = transmitted light; XPL = cross polarized light; RL = reflected light; PPL = plane polarized light).

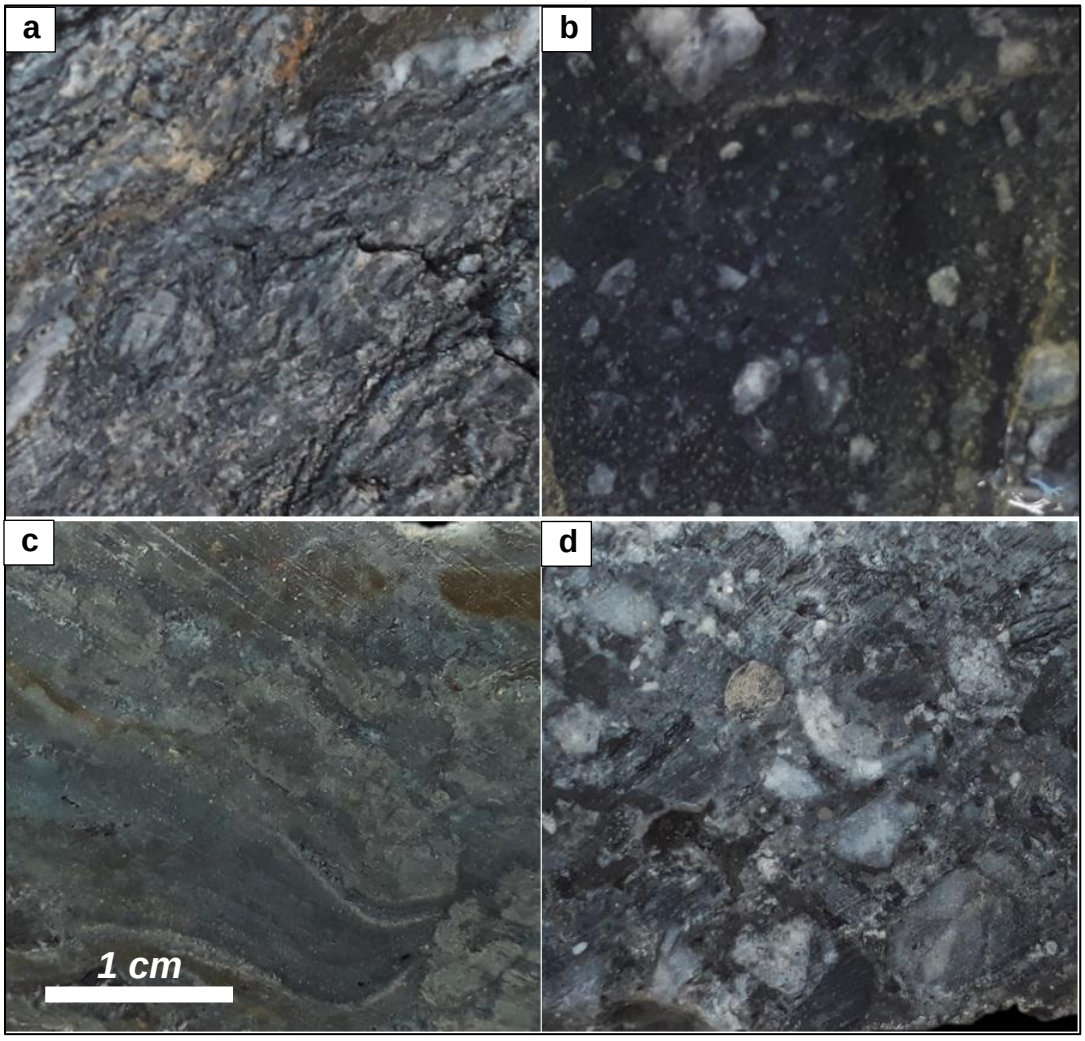

Figure 4.64. Photographs of core samples from Sırakayalar sulfidic damage zone underlying the oxidized talus zone. a) Deformed graphitic schist with disseminated pyrite and arsenopyrite (drill hole SHD-236, 55.35 m depth), b) Highly-brecciated zone with dark-colored graphitic matrix and fine disseminations of pyrite (drill hole SHD-236, 73.80 m depth), c) Colloform banded pyrite and arsenopyrite in the damage zone (drill hole S249A, depth 138.70 m), d) Brecciated and silicified deformation zone within schist with disseminated pyrite in breccia matrix (drill hole S249A, depth 143.20 m).

4.4 Hydrothermal Alteration

Hydrothermal alteration is extensive in the study area and has affected all of the wall-rock lithologies surrounding the silicified veins, especially in the Karatepe Sector where veins are observed in-situ (Fig. 4.65). Preliminary identification of hydrothermal alteration styles and associated mineral phases was achieved by petrographic studies. Short-wave infrared reflectance spectroscopy (SWIR) was further used to compliment petrographic observations.

4.4.1 Alteration in Karatepe and Sırakayalar

Since Karatepe mineralization is in place, effects of hydrothermal alteration are best observed in this part of the mineralized system compared to the Sırakayalar Sector. Hydrothermal assemblages in Karatepe can be characterized by mineral assemblages of distal, distal to proximal and proximal alterations. Spectral and microscopic investigations shed light on the alteration interpretations. Main proximal alteration is characterized by silicification in and immediately around the veins, whereas quartz-sericite/illite ± adularia alteration forms an envelope around the zones of silicification in Karatepe. On the other hand, distal to proximal alteration can be described by the assemblage silica ± smectite ± kaolinite ± Fe-Mg chlorite gradually away from the mineralized veins. Fe-Mg chlorite and relatively minor smectite dominates the outernmost part of the alteration halo.

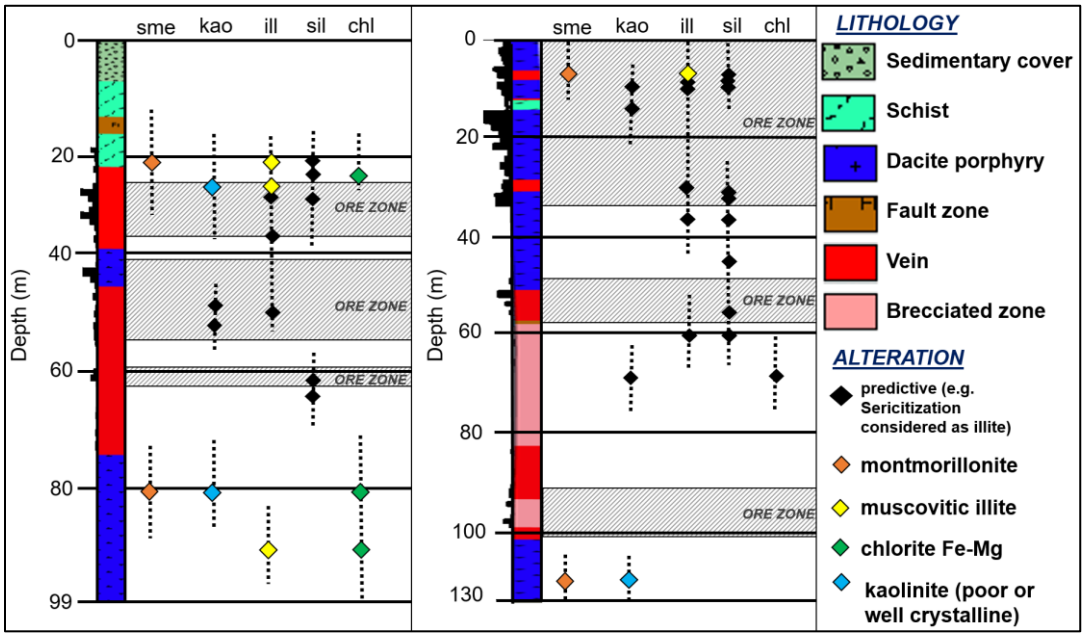

Figure 4.65. Measured and predicted alteration assemblages for Karatepe drill holes of SHD-138 and SHD-154.

Spectral measurements demonstrated presence of montmorillonite as the smectite group mineral with an intense absorption of H_2O at 1900 nm wavelenght range and broad Al-OH absorption at 2200 nm wavelenght range, in SWIR profiles (Figs. 4.66, 4.67, 4.68, and 4.69. Also, the measurements show that chlorite-illite mineral mixtures with weak inflection on Al-OH absorption feature at 2200 nm by Fe-OH and Fe, Mg-OH absorption features near 2250 and 2350 nm wavelenghts in SWIR profiles (Figs. 4.67, 4.70 and 4.71). Kaolinite, besides, show SWIR profile with OH and H_2O absorption features at 1400 and 1900nm wavelength ranges (Figs. 4.71 and 4.72). Such detectible alteration assemblages can be observed together with iron oxide (goethite and/or jarosite) indications showing broad crystal field absorption (CFA) features between 800-900 nm wavelenghts of VNIR (Fig. 4.68). Results of SWIR measurements are summarized in Table 4.2.

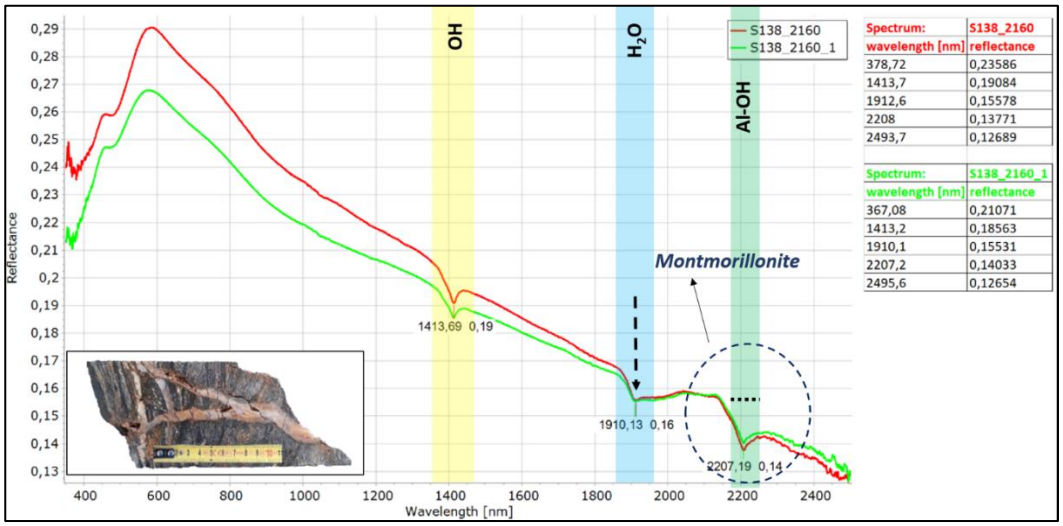

Figure 4.66. SWIR profile with normal reflectance spectra from 350 to 2500 nm for S138-2160 core sample taken from Karatepe Sector, showing distal to proximal hydrothermal alteration assemblage of a smectite mineral as montmorillonite with H_2O absorption at 1900 nm and broad Al-OH band 2200 nm wavelength ranges.

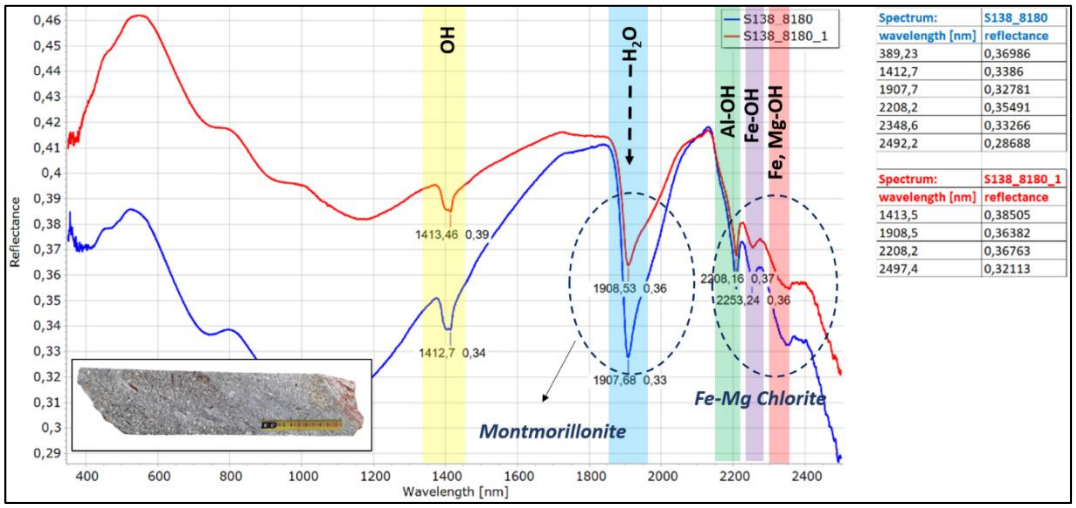

Figure 4.67. SWIR profile with normal reflectance spectra from 350 to 2500 nm for S138-2160 core sample taken from Karatepe Sector, showing distal to proximal hydrothermal alteration assemblages of a smectite mineral as montmorillonite with H_2O absorption at 1900 nm wavelength range, and assemblages of chlorite mineral with Fe-OH and Fe, Mg-OH absorption features near 2250 and 2350 nm wavelength ranges.

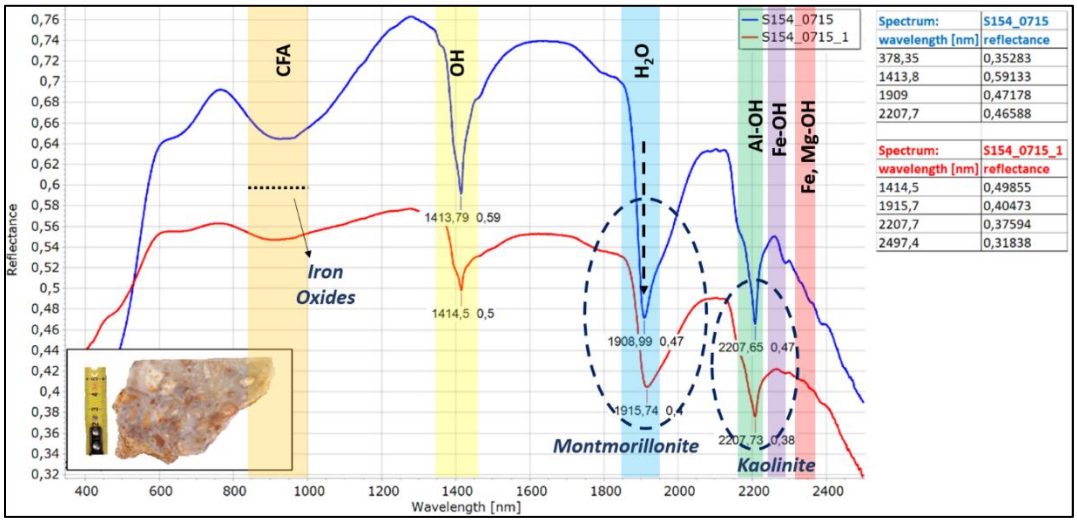

Figure 4.68. SWIR profile with normal reflectance spectra from 350 to 2500 nm for S154-0715 core sample taken from Karatepe Sector, showing distal hydrothermal alteration assemblage of kaolinite with OH and H_2O absorption at 1400 and 1900 nm wavelength ranges, and distal to proximal alteration assemblage of montmorillonite with abrupt absorption of H_2O at 1900 nm wavelength range. Also, iron oxide assemblages like goethite can be detectable with broad CFA (crystal field absorption) at 800-900 nm wavelengths of VNIR (visible and near infrared).

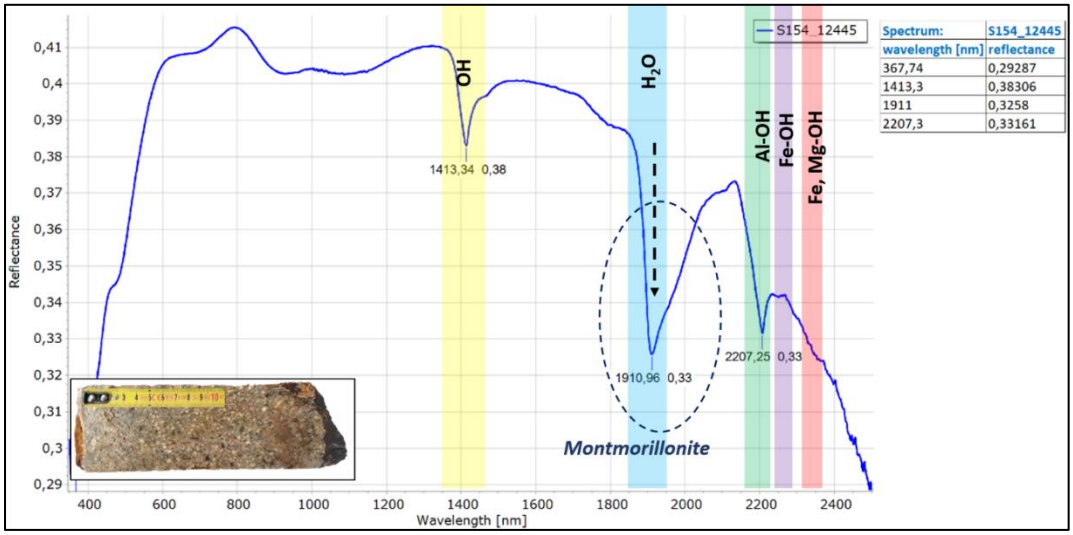

Figure 4.69. SWIR profile with normal reflectance spectra from 350 to 2500 nm for S154-12445 core sample taken from Sırakayalar Sector, showing distal to proximal hydrothermal alteration assemblage of smectite group mineral as montmorillonite with abrupt absorption of H_2O at 1900 nm wavelength range.

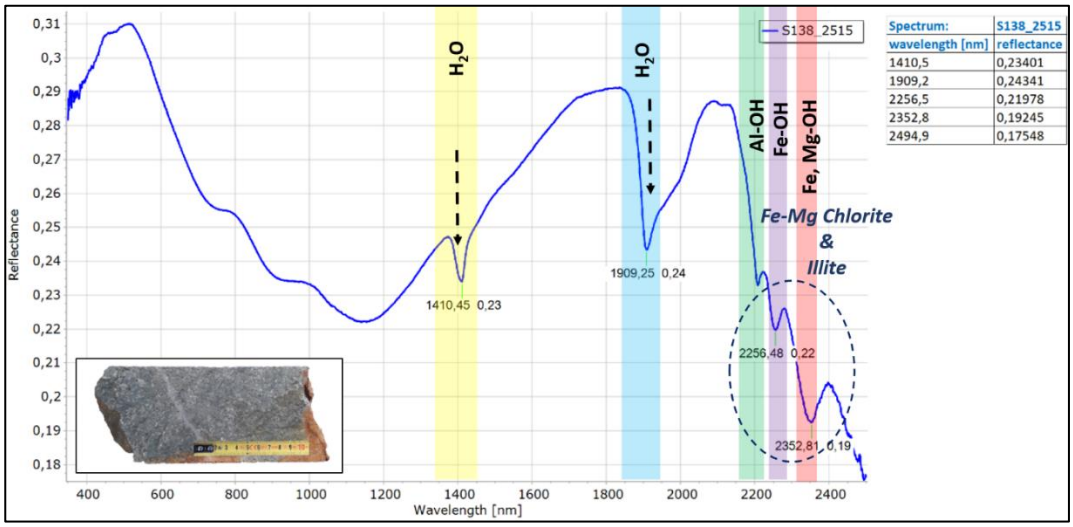

Figure 4.70. SWIR profile with normal reflectance spectra from 350 to 2500 nm for S138-2515 core sample taken from Karatepe Sector, showing distal hydrothermal alteration assemblages of chlorite-illite mineral mixtures with a weak inflection on Al-OH absorption feature at 2200 nm by Fe-OH and Fe, Mg-OH absorption features near 2250 and 2350 nm wavelength ranges.

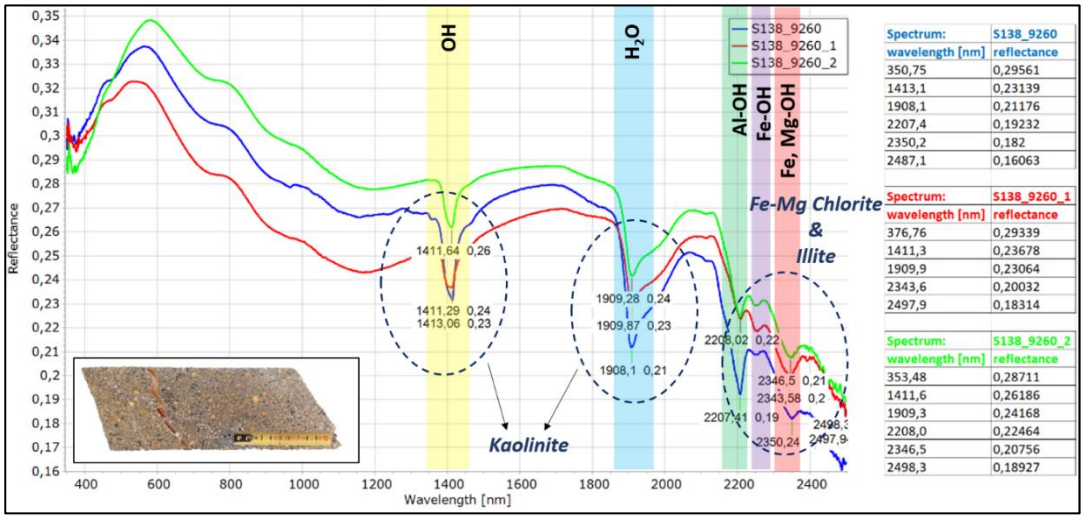

Figure 4.71. SWIR profile with normal reflectance spectra from 350 to 2500 nm for S138-9260 core sample taken from Karatepe Sector, showing distal hydrothermal alteration assemblages of a kaolinite with OH and H_2O absorption at 1400 and 1900 nm wavelength ranges, and assemblages of chlorite-illite mixture with Fe-OH and Fe, Mg-OH absorption features near 2250 and 2350 nm wavelength ranges.

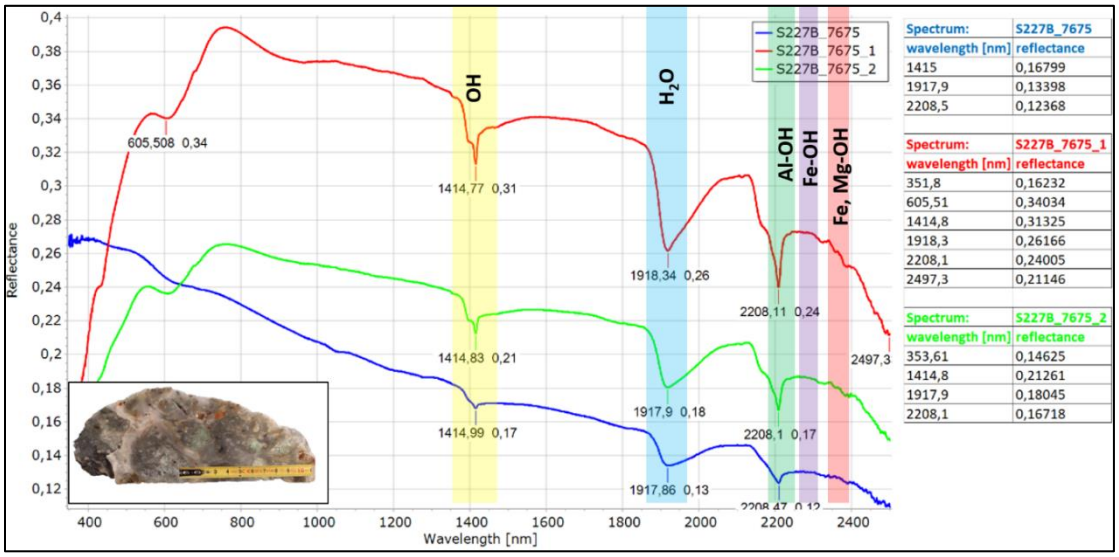

Figure 4.72. SWIR profile with normal reflectance spectra from 350 to 2500 nm for S227B-7675 core sample taken from Karatepe Sector, showing distal hydrothermal alteration of kaolinite with OH and H_2O absorption at 1400 and 1900 nm wavelength ranges.

Table 4.2. Summary table of spectral analysis for selected core samples in the study area, listed by TSG software for measurements done by ASD Terraspec 4 Hi-Res.

Sample	Min1 sTSAS*	Min2 sTSAS	Min3 sTSAS	Min1 sTSAV*
S138-2160	Montmorillonite	MuscoviticIllite	Siderite	
S138-2515	Chlorite-FeMg	MuscoviticIllite		
S138-8180	Chlorite-FeMg	Kaolinite-PX***		
	Chlorite-FeMg	Montmorillonite	Kaolinite-WX	
S138-9260	Chlorite-FeMg	MuscoviticIllite	Kaolinite-PX	
S154-0715	Kaolinite-WX**	Montmorillonite	Jarosite	Goethite
S154-12445	Montmorillonite	Siderite		Goethite
S227B-7675	Siderite	Jarosite	Kaolinite-WX	

*A set of unmixing results: TSAV in the VNIR, sTSAS in the SWIR, **WX: Well crystalline, ***PX: Poorly crystalline

Under the microscope, most samples obtained from drill cores exhibit sericitization, silicification, and chloritization of the wall-rock surrounding mineralized veins in addition to predicted kaolinite and/or smectite (Figs. 4.73, 4.74, 4.75, 4.76, 4.77 and 4.78c). Sericitization is best developed on igneous K-feldspar and plagioclase in dacite-rhyolite porphyry (Fig. 4.73c), as well as on adularia (Fig. 4.73a). Chlorite, on the other hand, has commonly replaced amphibole and biotite, again in igneous wall-rocks (Figs. 4.78a–b). Minor adularia was also identified in altered rocks in

Karatepe, and is likely a product of fluid boiling leading to gold precipitation (Fig. 4.73a). Metamorphic wall-rocks, however, do not show prominent zones of alteration in drill core, as their mineralogy is dominated by phyllosilicates. Such lithologies are expected to remain in equilibrium with the interacting hydrothermal fluids, perhaps unless fluids are significantly oxidized and/or of very low pH.

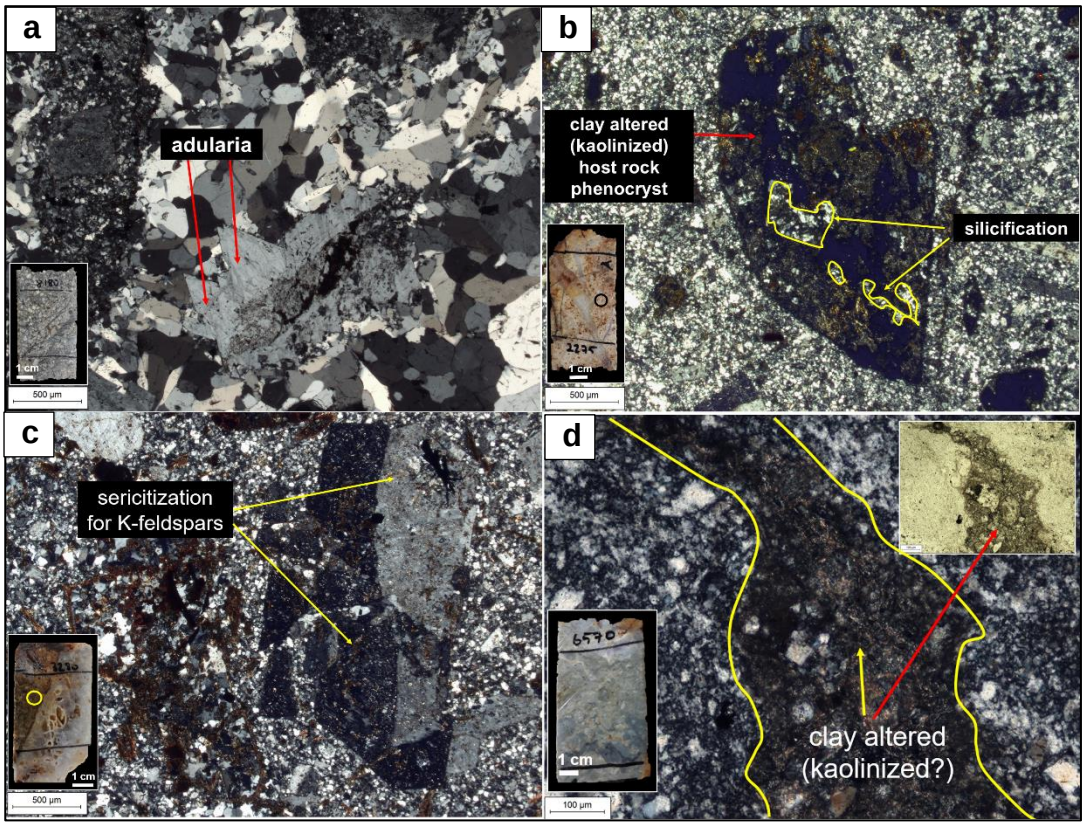

Figure 4.73. Microphotographs (TL, XPL image) mainly of proximal hydrothermal alteration assemblages including sericite and adularia with silicification from drill hole SHD-138 in Karatepe. a) Adularia intergrown with mosaic quartz (81.80 m depth), b) Clay-altered (kaolinite?) and silicified hornblende phenocryst in porphyry wall-rock (22.75 m depth), c) Sericite-altered feldspar in porphyry wall-rock. Orange coloration is due to supergene weathering and (32.30 m depth), d) Clay-altered (kaolinized?) fluidized and brecciated porphyry wall-rock (65.70 m depth). (Abbreviations: TL = transmitted light; XPL = cross polarized light).

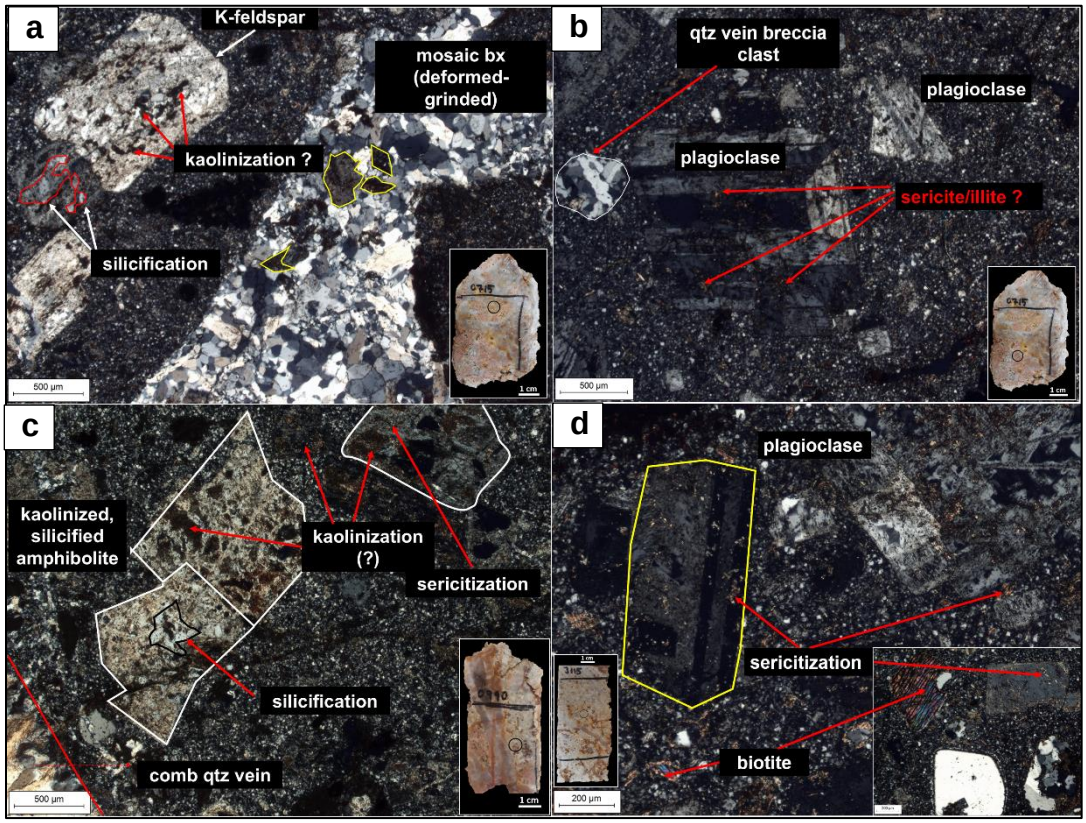

Figure 4.74. Microphotographs (TL, XPL image) mainly of proximal hydrothermal alteration assemblages as including quartz-sericite alteration from SHD-154 drillhole in Karatepe. a) Quartz-clay alteration after feldspars. Porphyry wall-rock cross-cut by a veinlet with mosaic infill (7.15 m depth), b) Weakly-sericitized plagioclase in porphyry wall-rock (7.15 m depth), c) Silica-clay (kaolinite) replacement of hornblende and sericite on feldspars in porphyry wall-rock (9.90 m depth), d) Weak to moderate sericite replacement of feldspar phenocrysts and groundmass in porphyry wall-rock (31.15 m depth). (Abbreviations: TL = transmitted light; XPL = cross polarized light).

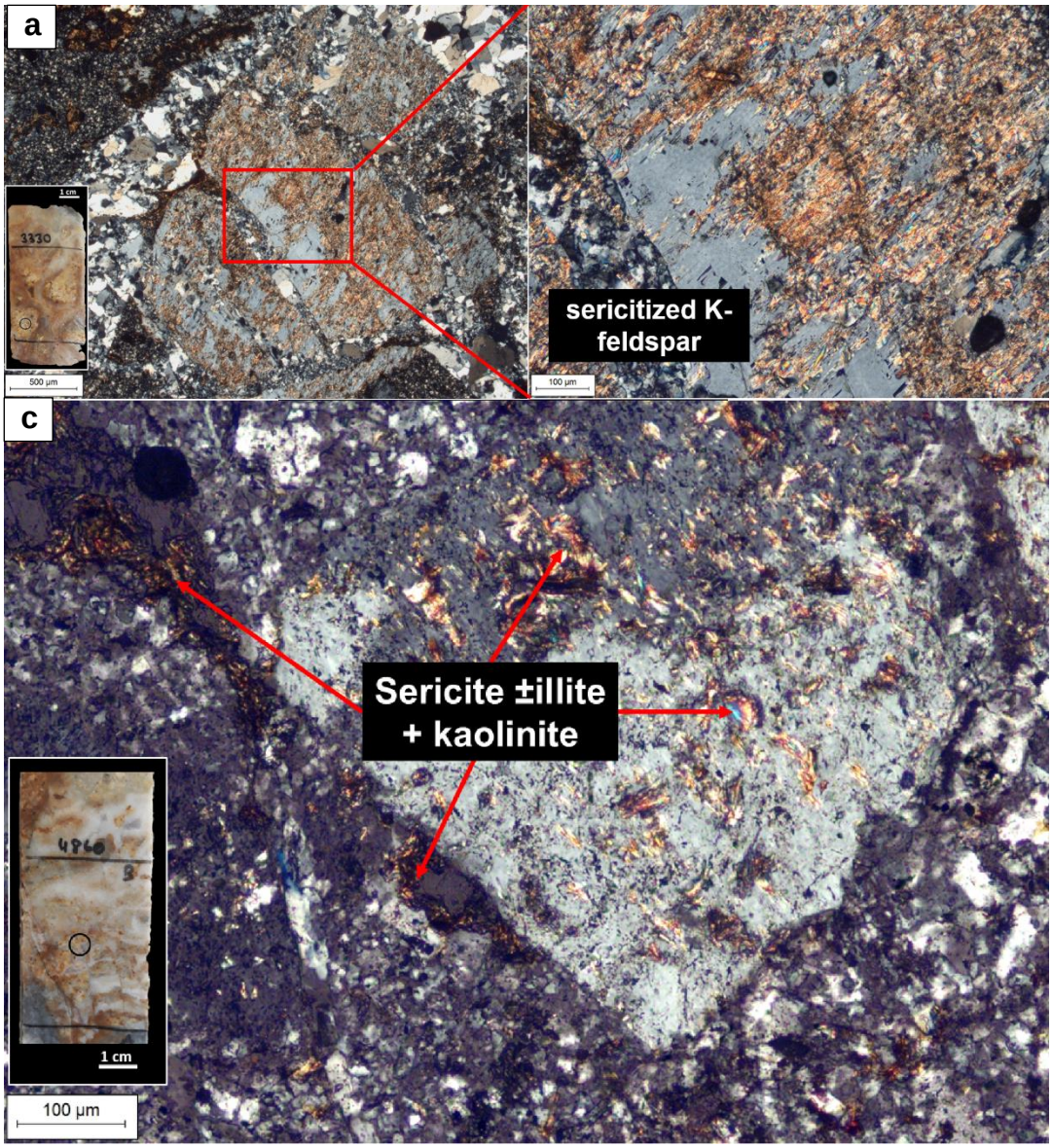

Figure 4.75. Microphotographs (TL, XPl image) mainly of proximal hydrothermal alteration assemblages from drill hole SHD-154 in Karatepe. a) and b) Pervasive quartz-sericite alteration in porphyry wall-rock (33.30 m depth), c) Sericite/illite-kaolinite replacemen of porphyry wall-rock (48.60 m depth). (Abbreviations: TL = transmitted light; XPL = cross polarized light).

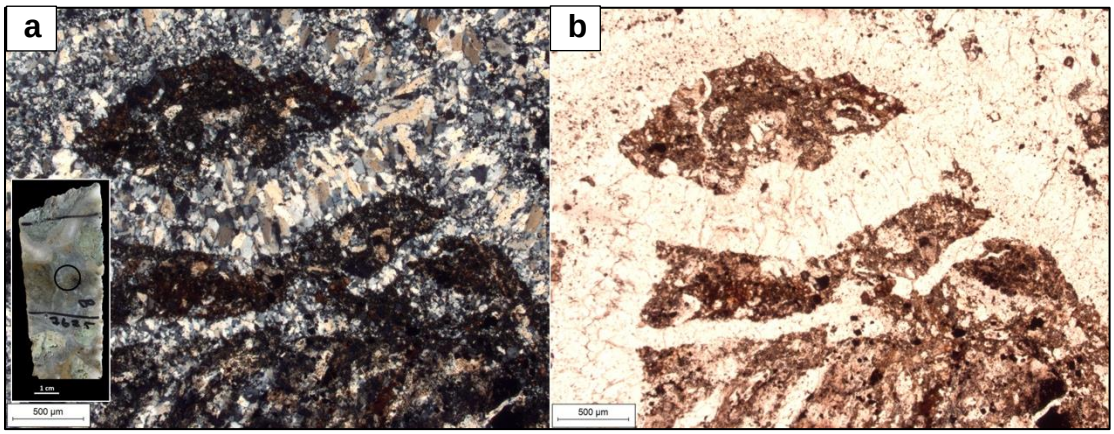

Figure 4.76. Microphotographs of quartz-kaolinite-dominant hydrothermal alteration drill hoe SHD-227B in Sırakayalar (76.75 m depth). a) and b) Quartz-kaolinite replacement of brecciated porphyry and locally cross-cutting comb quartz (TL, XPL and TL, PPL, respectively). (Abbreviations: TL = transmitted light; XPL = cross polarized light; PPL = plane polarized light).

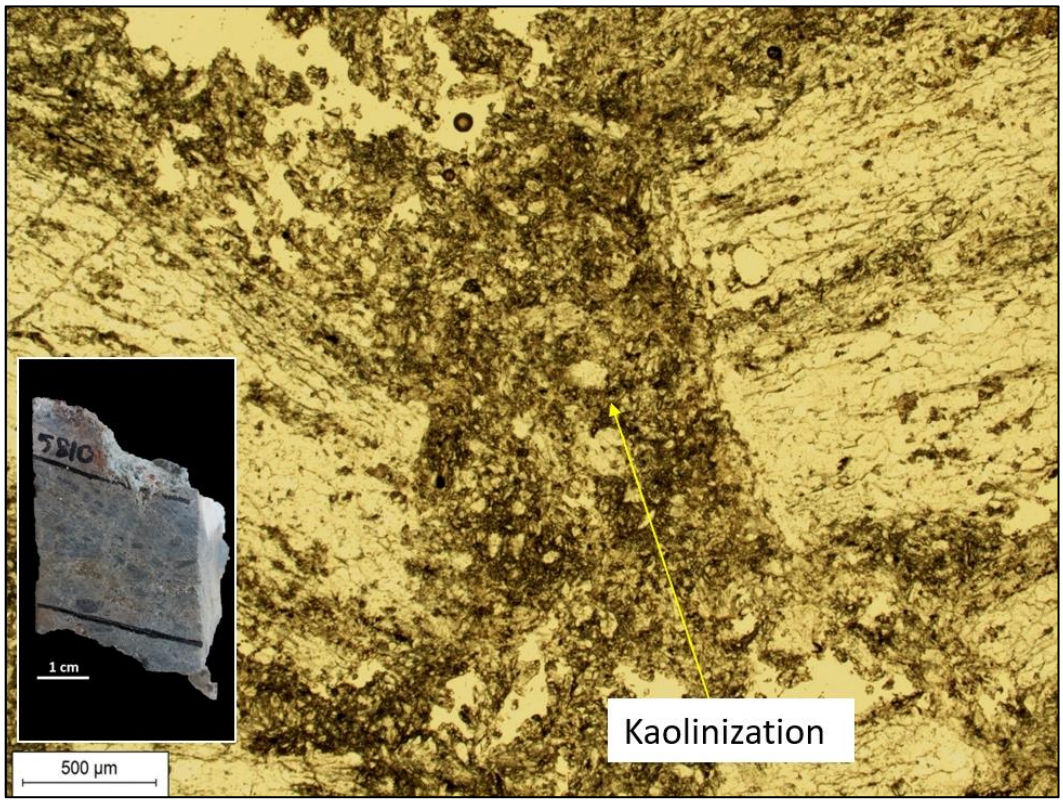

Figure 4.77. Microphotograph (TL, PPL image) view of a sample showing clay (kaolinite) alteration in porphyry wall-rock (drill hole S227B, 58.10 m depth). (Abbreviations: TL = transmitted light; PPL = plane polarized light).

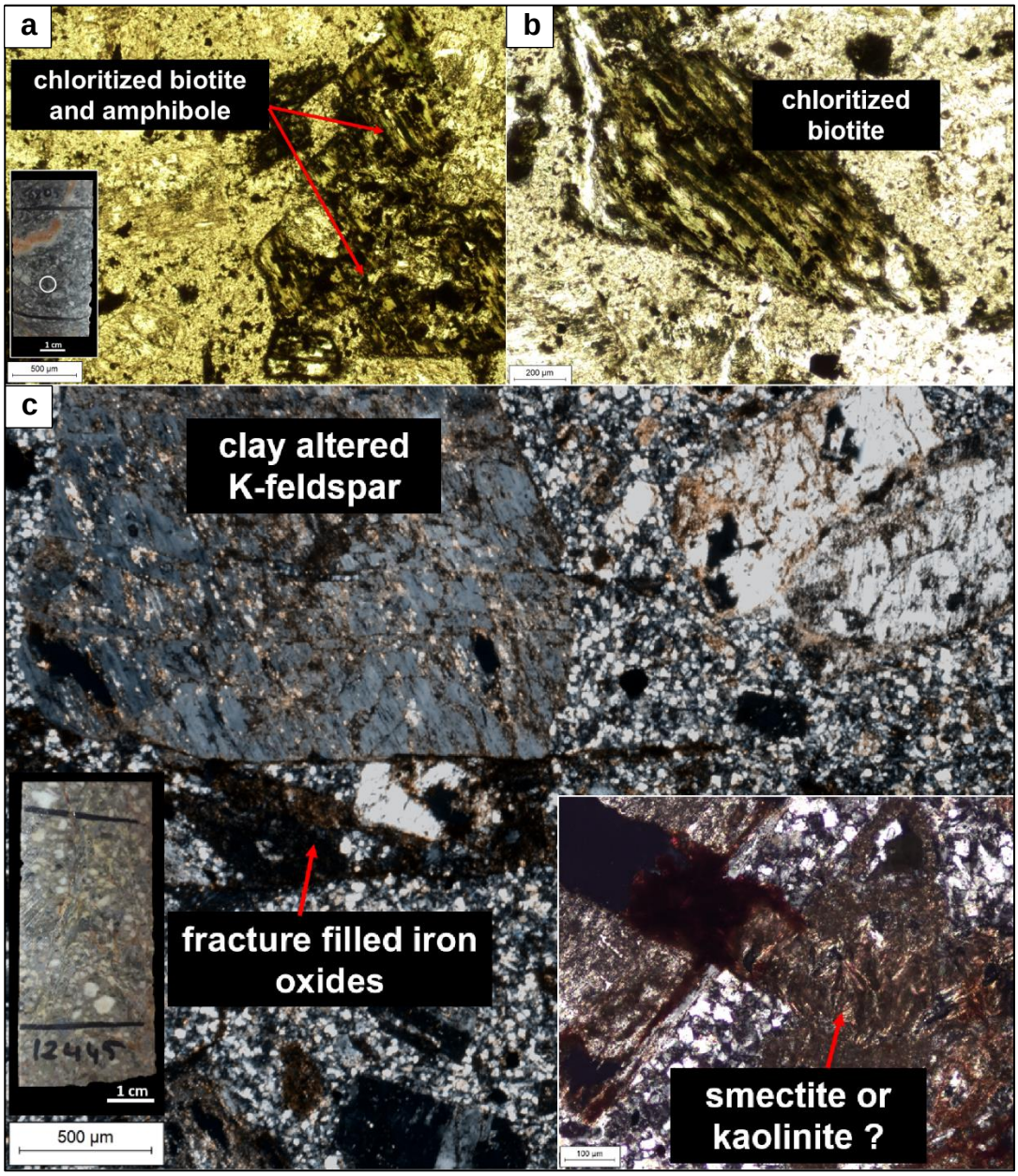

Figure 4.78. Microphotographs of distal and distal to proximal hydrothermal alteration assemblages from drill hole SHD-154 in Karatepe. a) and b) Chlorite and minor sericite replacement of hornblende and biotite in porphyry wall-rock (TL, PPL images; 68.05 m depth), c) Smectite-kaolinite replacement of porphyry wall-rock (TL, XPL image; 124.45 m depth). (Abbreviations: TL = transmitted light; XPL = cross polarized light; PPL = plane polarized light).

4.4.2 Molar Elemental Ratios in Karatepe

Hydrothermal alteration leads to changes in elemental and mineralogical composition of wall-rocks through which hydrothermal fluids are circulated. Such metasomatic exchange reactions can be quantified using a variety of methods including mass exchange calculations, determination of alteration indices, and also utilization of molar element ratios. The latter is commonly used to predict predominant alteration minerals that form through replacement of primary minerals commonly in igneous rocks (e.g., Warren et al., 2007; Barker et al., 2019; Halley, 2020).

In their study conducted on low-sulfidation epithermal systems in New Zealand, Warren et al. (2007) applied molar ratios of common rock-forming elements in feldspars and phyllosilicate alteration minerals to better understand the abundance of alteration minerals in such deposits through the use of routine lithogeochemical data. According to Warren et al. (2007); molar elemental ratios indicate fresh rocks, K gain and Na, Ca loss, presence of illite-smectite-kaolinite assemblages. When K/Al (molar); (1) is in between 0.2 and 0.33, (2) is less than 0.2 and (3) equals to zero, they indicate presence of illite, smectite and kaolinite, respectively (Warren et al., 2007).

A similar attempt was made using the lithogeochemical data of the Karatepe mineralized system, where dacite porphyries are the common wall-rocks around the hydrothermal veins. Metamorphic wall-rock assay data from Karatepe was not used, since the schist unit mainly comprises similar phyllosilicate minerals that are also found in the alteration assemblages. Sırakayalar samples were also not included in ploting of molar ratio diagrams as the mineralized veins in this area are not in direct contact with their igneous wall-rocks.

According to the molar ratio plot for the porphyry unit in Karatepe Sector (Fig. 4.79), majority of data concentrated within interlayed illite-smectite, illite, K-mica with high Na and Ca loss, and both K gain and loss depending on proximity to

mineralization. In this plot, these alteration assemblages correspond with mostly moderate to high grades of Au mineralized samples containing >1 ppm Au (especially in the range 2-5 ppm and >5 ppm Au intervals). Also, it can be understood that there are kaolinite and chlorite assemblages in Karatepe. Altered samples with low or insignificant gold grades (in the range 0.1-0.5 and <0.1 ppm Au intervals) are scattered in Figure 4.79, and some of these samples do not show strong evidence Na and Ca loss.

Overall results are compatible with drill core and thin section observations that indicate that relatively higher grade mineralization at Karatepe is associated with siliceous veins that are surrounded by immediate quartz-sericite/illite alteration with minor or negligible smectite, kaolinite, and adularia in the proximal alteration zones. Sericite in these significantly higher grade zones is either muscovitic or illitic sericite (both minerals were detected petrographically). Although adularia was detected in a few of the inspected samples, its abundance throughout the entire Karatepe mineralization is not significant; that is it is either in low abundance, or the significant amount of adularia formed in or adjacent to the veins has been almost completely altered to sericite.

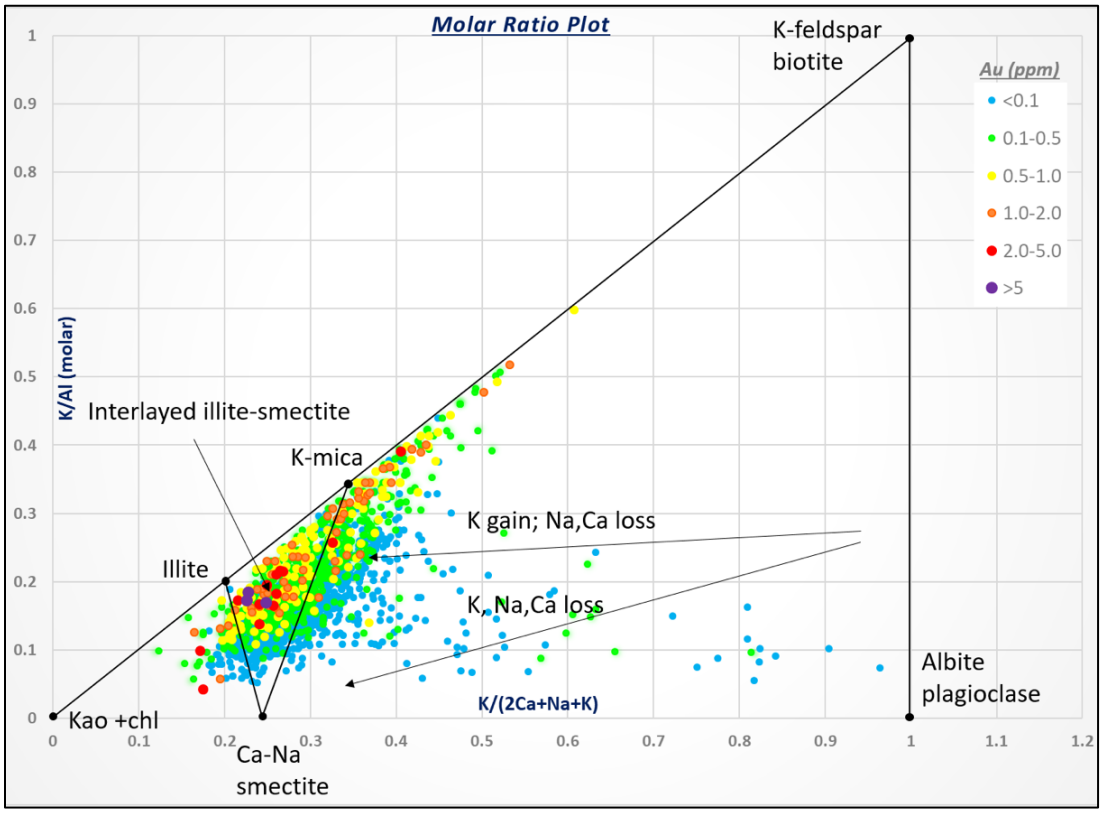

Figure 4.79. Molar ratio plot, (2Ca+Na+K)/Al vs. K/Al, for Karatepe porphyry unit (diagram from Warren et al. 2007). Intervas for gold grades are indicated using different colores.

CHAPTER 5

DISCUSSION

5.1 Geotectonic Setting of the Sırakayalar and Karatepe Deposits

The Sırakayalar and Karatepe Au-Ag deposits of the Şahinli district near Lapseki are two of the significant epithermal-style systems of the Biga Peninsula. Gold-silver mineralization in these two sectors as well as in the adjacent Kovanlık prospect and also the epithermal veins of the Lapseki gold mine to the south (Gülyüz et al., 2018) and the Şahinli deposit to the north (Yılmaz et al., 2010) are all emplaced within the basement Paleozoic schists and/or cross-cutting sub-volcanic and volcanic units of the Eocene Beyçayır volcanics.

Despite a lack of geochronological data from the altered/mineralized veins and from subjacent magmatic host rocks, epithermal mineralization in the aforementioned areas (including the Sırakayalar and Karatepe deposits) is likely to have occurred during or shortly after the Eocene magmatism at the Lapseki area (42–38 Ma; Altunkaynak and Genç, 2008; Erenoğlu et al., 2022). Widespread hydrothermal alteration (silicification, quartz-illite±kaolinite±aduaria, chlorite-epidote±carbonate) observed in the intermediate to felsic sub-volcanic rocks also indicates that epithermal-style mineralization developed as late as the middle Eocene. This presumption provides a broader context for the formation environment of the Karatepe and Sırakayalar epithermal systems, which suggests a post-subduction-related setting following closure of the Izmir-Ankara-Erzincan Ocean at the end of the Mesozoic (Stampfli and Borel, 2004; Moix et al., 2008).

Majority of the base and precious metal deposits in the Biga Peninsula formed in a similar post-subduction environment mainly in two distinct periods; between 42–35 Ma and 29–22 Ma. Epithermal systems between Çanakkale and Lapseki including

the Şahinli district deposits, the Kartaldağ and Madendağ deposits (Yiğit, 2012; Ünal-Imer et al., 2013), and the porphyry-epithermal systems of the Halilağa and TV Tower districts (Leroux, 2016; Smith et al., 2016; Brunetti, 2018) were developed within the former interval.

Lithogeochemical diagrams based on immobile element concentrations indicate that the altered igneous rocks at Karatepe are mainly andesitic to dacitic porphyry units. The least-altered porphyries contain hornblende and biotite phenocrysts as well as magnetite microphenocrysts, indicating the hydrous and oxidized nature of these magmatic units. These geochemical features are conformable with that of other regional Eocene magmatic units, which are similarly represented by calc-alkaline andesitic-dacitic volcanic and volcaniclastics and their sub-volcanic equivalents (e.g. Aldanmaz et al., 2000; Altunkaynak and Genç, 2008; Altunkaynak et al., 2012; Altunkaynak and Dilek, 2013; Kuşcu et al., 2019; Erenoğlu et al., 2022). Sub-alkaline to mildy-alkaline magmatism during this period developed in an extensional setting (Sanchez et al., 2016), likely in response to break-off of the northward subducting Izmir-Ankara-Erzincan Neotethys (e.g., Altunkaynak et al., 2012). According to Richards (2009 and 2011) remelting of the previously subduction-modified lower crustal through such processes (i.e., slab break-off, delamination) through upwelling of the hot asthenosphere may lead to formation of post-subduction porphyry and epithermal systems hosted in magmatic suites with arc-like geochemical signatures. This is widely accepted as the main mechanism that resulted in formation of the majority of Cenozoic magmatic-hydrothermal systems in the Biga Peninsula, particularly including the porphyry, skarn, and high-sulfidation epithermal systems of Eocene and Oligocene age (Yiğit, 2012; Sanchez et al., 2016; Kuşcu et al., 2019). Although it is not within the scope of this study, it is likely that the post-subduction magmatism had a major role in formation of at least the fertile magmatic host rocks of the Karatepe and Sırakayalar epithermal systems. While a reconnaissance fluid inclusion study by Clark (2014) indicated no major magmatic contribution to the ore-forming hydrothermal fluids in the study area, the Şahinli intermediate-sulfidation epithermal mineralization further north is suggested to have

minor magmatic input during base and precious metal mineralization in that area (Yılmaz et al., 2010).

In a broader context, it appears that Eocene magmatism throughout the entire extent of the Izmir-Ankara-Erzincan Suture Zone is fertile for generation of post-subduction epithermal deposits as evidenced from similar systems in the Eskisehir-Bursa district (Rabayrol et al., 2021), the Gicik low-sulfidation deposits in Ankara (Çil, 2018), and the intermediate-sulfidation epithermal systems in the Eastern Pontides (e.g., Mastra; Tüysüz et al., 1995; Bilir, 2015). In all of these districts, mineralization seems to be closely associated with the middle to late Eocene post-subduction calc-alkaline magmatism.

5.2 Nature of Mineralization at Karatepe and Sırakayalar Deposits

In the Karatepe and Sırakayalar Sectors, gold-silver mineralization is mainly contained within quartz veins and breccias hosted in basement metamorphics and dacite porphyry units in Karatepe and a talus zone developed through metamorphic and dacitic units in Sırakayalar. Veins of the Karatepe Sector are relatively intact, and these have been emplaced along steeply-dipping N-S- and E-W-trending normal structures. Textural features of these veins indicate a progression from early massive quartz to later brecciated, crustiform-banded, and cockade veins, in which a significant proportion of mineralization is associated mainly with zones of brecciation.

Immediate wall-rocks at the Karatepe Sector have undergone intense silicification, which have been enveloped by relatively broader zones of argillic (quartz-illite±kaolinite±adularia) and propylitic (chlorite-epidote-carbonate) alteration. Mineralized veins are characterized by low amounts of sulfide minerals dominated by pyrite with lesser arsenopyrite locally accompanied by native gold and electrum. Other common base metal sulfides were neither observed in any of the sampled drill holes, nor any significant base metal enrichment was encountered in drill assay results. The ubiquitous presence of pyrite and arsenopyrite in the mineralized veins

points towards low sulfidation states (Hedenquist et al., 2000; Einaudi et al., 2003). Based on these characteristics, the Karatepe vein system is classified as a typical low-sulfidation epithermal mineralization. The superposition of distinct vein textures indicates high degrees of hydrothermal fluid focusing possibly into zones of structural weakness exploited episodically. The presence of bladed textures and minor adularia in vein wall-rocks suggests that fluid boiling was the main ore precipitating mechanism for epithermal mineralization (e.g., Henley and Brown, 1985; Reed and Spycher, 1985; Berger and Henley, 1989; Hedenquist et al., 2000; Moncada et al., 2012). Fluids were of near neutral to slightly acidic pH in nature as indicated by stable alteration minerals such as adularia and illite (Reyes, 1990; Hedenquist et al., 2000).

Due to its well-preserved nature, hydrothermal alteration is best developed in the Karatepe Sector particularly in the porphyry wall-rocks. Beyond narrow zones of intense silicification, quartz-illite±kaolinite±adularia alteration is the prominent alteration style associated with the mineralized veins. Primary igneous minerals mainly including hornblende and plagioclase are partially to completely altered into illite and quartz with relatively minor kaolinite and adularia. Where texturally observed, adularia has also often been transformed into sericite, indicating predominance of clay-stable weakly-acidic pH conditions. In contrary to igneous wall-rocks, effects of quartz-illite±kaolinite±adularia alteration is rather obscure when the wall-rocks are mica schists. This is perhaps due to the compositional similarity between the phyllosilicate-dominated wall-rocks and the ore fluids. Quartz-illite±kaolinite±adularia alteration is not easily discernable in the schist unit at the outcrop scale, but petrographic observations indicated that fine-grained sericite has at least locally replaced muscovite-phengite phases.

Field/drill core observations combined with petrographic and geochemical studies showed that higher grade gold-silver mineralization at Karatepe is spatially associated with zones of quartz-illite±kaolinite±adularia alteration. Based on the molar ratio plots (Fig. 4.79), ore-bearing fluids are generally illite-stable, but at depths typically greater than 200 meters coarser-grained muscovitic sericite was also

observed at Karatepe drill cores. Presence of muscovite-illite assemblages in the wall-rock alteration suggests an upper temperature limit of about 300°C for the ore fluids (Henley and Ellis, 1983; Reyes, 1990; Hedenquist et al., 2000).

In contrary to the Karatepe Sector, mineralized veins of the Sırakayalar Sector are not found in-situ due to intense post-mineralization faulting. These veins also display typical textures of epithermal precious metal deposits; from massive through colloform-banded and brecciated veins dominated by quartz. Adularia was not observed in any of the samples collected from the Sırakayalar drill holes, but the widespread presence of bladed textures suggests that boiling was the main ore-forming mechanism also in this part of the system. This was also supported by co-existing liquid and vapor-rich fluid inclusions in samples from both Karatepe and Sırakayalar (Clark, 2014). The reconnaissance microthermometric investigation of fluid inclusion assemblages revealed the presence of low-salinity (0.6–1.4 wt.% NaCl equiv.), low- to moderate-temperature (170^{o} to 310^{o}C) fluids with moderate CO_2 contents in both areas (Clark, 2014).

At Sırakayalar, beneath the talus zone, mineralized veins show an increase in intensity at or immediately below the shallowly-dipping faulted schist contact. This suggests that the veins were initially emplaced along this zone, and then repeatedly faulted down and disrupted to form a talus zone comprising mineralized vein and basement rock fragments. The relatively better-preserved veins observed just south of the talus zone are possibly representing the original vein structure at Sırakayalar. However, these veins are likely to have been truncated by a shallowly-dipping detachment fault, since these veins are blind at depth. Such shallow structural zones were likely facilitated district-scale fluid flow, and later the ore-forming fluids channelized into steeply-dipping normal faults to form sub-vertical veins as observed in the Karatepe Sector.

A notable feature of the Sırakayalar Sector is that although the mineralized veins are contained within a red-colored, oxide-rich matrix material, the veins themselves still comprise sulfide minerals. This was interpreted to be a result of quick deposition of

the vein fragments following faulting and disruption of the original veins, which would otherwise are expected to have undergone weathering and oxidation.. The fine-grained nature of this oxide- and clay-rich matrix material was also probably prevented oxidation of the vein fragments at Sırakayalar.

It is hereby suggested that Sırakayalar, in terms of its geological characteristics and ore morphology, is a transported epithermal system that has been formed as a result of episodic fault activity. However, the large sizes (up to 1 meter in length) and angular nature of the vein fragments suggest that the distance of transportation was limited, and that the rootless vein blocks immediately to the south may represent the main source of the vein hosted in talus. Quick burial of the vein fragments was key for the well-preserved nature of the veins and the common presence of sulfides as vein infill.

Supergene oxidation and weathering have developed to a limited extent in both Karatepe and Sırakayalar Sectors. Highly-oxidized siliceous breccias are present within the top 10 meters at Karatepe, and these usually yield higher gold grades due to oxidation of pyrite and arsenopyrite into goethite and possible liberation of refractory gold. As mentioned earlier, despite intense faulting and disruption of the primary ore veins at Sırakayalar and highly-oxidized nature of the talus matrix, the vein fragments embedded within this matrix display only partial oxidation. This was interpreted to be a result of quick burial of the veins following faulting and also due to the relatively impermeable nature of the talus matrix consisting of Fe-(hydr)oxides and clays.

5.3 Regional Significance of the Karatepe and Sırakayalar Deposits

The northern part of the Biga Peninsula, near Lapseki hosts a number of mineralized areas, some of which have shown economic viability. The Lapseki Au mine operated by TÜMAD Mining is located within the adjacent tenement to the south of the Karatepe Sector. The open pit operation at the Lapseki Au mine exploits predominantly N-S- and E-W-trending siliceous, low-sulfidation-style veins in an

area located less than 1 km south from the Karatepe veins. Based on the similar orientation of the veins, and the textural characteristics dominated by massive to crustiform, through brecciated and cockade nature of the veins (Gülyüz et al., 2018 and 2020; Table. 5.1), the Karatepe Sector was interpreted to be the northern continuation of the Lapseki deposit. In addition, the similar juxtaposition of various vein textures at Lapseki indicates that episodic re-opening of mineralized structures have taken place in the southern part of the system as well, most likely due to fluid overpressuring and subsequent fault reactivation to facilitate multi-stage vein development (Gülyüz, 2018).

The Madendağ low-sulfidation epithermal deposit (Fig. 3.7; Table. 5.1) located approximately 35 km southwest is another likely analogue of the low-sulfidation epithermal systems of the Şahinli district. In Madendağ, pyrite-bearing quartz veins are hosted within argillized basement mica schists in the vicinity of Eocene andesite porphyry intrusions (Ünal-İmer et al., 2013).

To the south of Karatepe and Sırakayalar, an intermediate-sulfidation epithermal gold-base metal deposit is present that is known as the Şahinli/Tespihdere deposit (Yılmaz et al., 2010; Table. 5.1). The Şahinli deposit is relatively rich in base metals and is characterized by a mineral assemblage of pyrite, chalcopyrite, sphalerite, galena, tetrahedrite, molybdenite, digenite, chalcocite, covellite, and cerrusite with quartz and barite gangue (Yılmaz, et al. 2010). Detailed fluid inclusion and stable isotope studies indicated that some magmatic component was involved in formation of the Şahinli system, and the deeper alteration zones with muscovitic sericite may be indicative of proximity to a deeper porphyry-style mineralization (Yılmaz et al., 2010).

Table 5.1. Summary characteristic of Cenozoic epithermal systems in Biga Peninsula.

	Şahinli		Lapseki	Şahinli/Tespihdere	Kartaldağ	Madendağ
	Karatepe	**Sırakayalar**				
Geological setting	Subvolcanic stock as dacite porphyry within schist	Not insitu	Subvolcanic stock as QFH porphyry within mica schist	Volcaniclastic rocks bounded by a WNW–ESE-trending graben fault	Dacite porphyry stock	Mica schist overlain and intruded by andesite, dacite flows and domes
Mineralization style	LS epithermal Au-Ag	LS-epithermal Au-Ag	LS epithermal Au	IS epithermal	HS epithermal	LS epithermal
Ore minerals	native Au, electrum, py, asp	Au, py, asp, ±dig	native Au, native Ag	py, cpy, sph, gn, tet, mo, dig, cc,cv, cer	Au, py, cv, sph	Au, py, sph
Quartz textures	massive, brecciated, crustiform banded, cockade, comb	massive, colloform-crustiform banded, brecciated, bladed, comb	crustiform, colloform, brecciated, cockade, saccharoidal, pseudo-bladed	plumose, vug infills, comb, cockade, brecciated	massive/vuggy, vug-lining, banded, colloform, comb	comb, colloform, banded, brecciated
Main alteration styles	silicification - illite ±smectite ±kaolinite ±adularia	-	illite, smectite, sericite ± pyrite	illite/muscovite, mixed-layer illite/smectite, clinochlore, alunite, dickite/nacrite, pyrophyllite	chlorite/smectite–illite±kaolinite, quartz–kaolinite, quartz–alunite–pyrophyllite, quartz–pyrite	sericite–illite–kaolinite, and quartz–pyrite
Host rock age	Eocene (1,2) and Paleozoic (3)	-	Middle Lutetian, Paleozoic	Upper Eocene	Eocene	Paleozoic, Eocene
Data Sources	1,2, in this study	in this study	4	5	6	6

Data Sources: 1= Altunkaynak and Genç (2008), 2= Erenoğlu et al. (2022), 3= Okay and Satır, 2000b 4= Gülyüz (2018), 5= Yılmaz et al. (2010), 6= Ünal-İmer et al. (2013)
Abbreviations: Au= gold, Ag= silver, cpy= chalcopyrite, gn= galena, HS= high-sulfidation, IS= intermediate sulfidation, LS= low sulfidation, mo= molybdenite, py= pyrite, sph=spalerite, tet= tetrahedrite

CHAPTER 6

CONCLUSION

Şahinli Au-Ag deposit including Sırakayalar and Karatepe mineralized systems in NW part of Biga Peninsula was studied by considering combinations of geological mapping, sampling of core samples, petrography, ore and gangue mineral identification, alteration assemblages determining by measured results and predictive observations, and also some mineral geochemistry. Consequently, findings of the study can be clarified as below;

For Karatepe epithermal gold-silver mineralization;

- The mineralization is hosted within graphitic mica schist of Çamlıca metamorphics (~69 Ma; Okay and Satir, 2000b) and dacite porphyry unit called as Karatepe Member which regionally correlates with Eocene volcanics (37 ± 0.9 Ma to 42.08 ±0.09; Altunkaynak and Genç, 2008; Erenoğlu et al., 2022).
- According to Nb, Ti, Y and Zr concentration results of 21 volcanic samples from 6 drillholes of Karatepe, the samples are plotted in ryholite-dacite region at Zr/Ti vs. Nb /Y diagram as a result of evolved magma.
- The mineralization display a great variety of typical low sulfidation quartz textures that cross-cut or overprint each other which shows episodic hydrothermal activities. Quartz stages controlling Au and Ag precipitation can be characterized by 3 phases including the earliest phase (Stage 1) of massive crystalline mosaic/jigsaw and saccharoidal quartz ± ghost bladed, after (Stage 2) comb-crustiform quartz and the latest phase (Stage 3) of cockade-comb quartz. In addition to main quartz phases, minor microscopic quartz textures exist such as plumose and feathery quartz. Also, pulses of brecciation events formed during mineralization and accompanied to the main quartz phases. The brecciation events stand for the times starting from

stage 1 and continuing to stage 2, and starting from stage 2 and continuing stage 3.

- Early stage massive crystalline quartz phase and further brecciated quartz phase for Karatepe display low to highest grades of Au which shows direct proportion with Ag grades while comb and cockade quartz phases mostly observed in low to medium grades.
- Mineralized veins and wall rocks display a simple ore mineral assemblages and accompanying sulfides. Gold occurs either native gold or electrum up to 100μm sizes, mostly observed in mosaic/jigsaw quartz phase of the earliest stage. Sulfide abundances are generally low ranging between 5 and 15 % of the total volume, and pyrite (rhombic, disseminated, weathered forms) is the most abundancy sulfide mineral type together with arsenopyrite with euhedral rhombic form or as acicular, lath-like crystals. Also, high graded intervals of Au and Ag correspond to the intervals observed as the highest sulfide and precious metal abundancy, quartz veins containing the earliest quartz phases overprinted by later quartz phases.
- Deformation indicators can be observed in both microscopic and field observations. Fieldworks bring out outcrops showing faults and shear zones within hosts rocks and contacts of host rocks in Karatepe mineralization. Micro-scale observations demonstrate deformation indicating brecciation, cracking, grinding of quartz crystals, quartz boundary migrations and deformational zonings.
- Main proximal alteration is characterized by silicification, sericitization and ±illite ±adularia minerals around mineralized veins in Karatepe. On the other hand, distal to proximal alteration can be described as an assemblage of silicification ±smectite ±kaolinite ±Fe-Mg chlorite towards the outside of the mineralization. Lastly, distal alteration is observed as an assemblage of Fe-Mg chlorite and less smectite minerals.
- According to molar ratio plot of (2Ca+Na+K)/Al vs. K/Al for Karatepe volcanics, interlayed illite-smectite, illite, K-mica with high Na, Ca loss and

both K gain and loss correspond to mostly moderate to high grades of Au mineralized samples larger than 1 ppm Au grades (especially ranging 2-5 ppm and >5 ppm Au intervals). Also, kaolinite and chlorite assemblages with low or no grades (ranging 0.1-0.5 and <0.1 ppm Au intervals) are scattered in that plot, and some of them do not show a strong evidence of alteration signatures as Na and Ca loss.

For Sırakayalar epithermal gold-silver mineralization;

- Mineralized zone hosts mostly talus/quartz float zone and damage zone beneath the talus material which transported and disrupted from basement metamorphic unit hosted primary mineralization, currently observed in a limited area including old galleries, by episodic faulting mechanisms related with regional deformation. Transportation in Sırakayalar can be thought to be happened through NW and NNE directions when general trend of preserved float/talus zone is considered in that area. The mineralized zone covered by younger clastic units of Sektaşı formation place to place at the surface.
- Talus unit, displays 0.25 km2 area immediately east of the NW-trending valley (Sarısu River) in the central sections, consists of quartz vein fragments (up to approximately 2 meters in size) as well as fragments derived from mica schist and andesite-dacite porphyries. These variably-sized vein and wall rock fragments are cemented by a fine-grained wad that contains Fe-oxide and clays, which gives it a typical red color in the surface.
- The damage zone cannot be clearly observed from the surface. Its behavior and content can only be understood by drill holes. This zone consists dominantly highly deformed and partially brecciated schist and some mineralized veins. Also, this zone can be characterized by being transitional boundary from oxide to sulfide states. It generally contain pyrite and arsenopyrite mineralization which can be observable as macro and micro-scales.

- The mineralization display a great variety of typical low sulfidation quartz textures that cross-cut or overprint each other which shows episodic hydrothermal activities. Quartz stages controlling Au and Ag precipitation can be characterized by 3 phases including the earliest phase (Stage 1) of massive crystalline mosaic/jigsaw and saccharoidal to later bladed quartz, after (Stage 2) crustiform-comb quartz and the latest phase (Stage 3) of cockade-comb quartz. In addition to main quartz phases, minor microscopic quartz textures exist such as flamboyant quartz. Also, pulses of brecciation events formed during mineralization and accompanied to the main quartz phases. The brecciation events stand dominantly for massive crystalline quartz of stage 1 by at least two phases including silica-rich matrixed and hematite-rich matrixed brecciations.
- Mineralized vein boulders and fragments and damage zone beneath the talus display a simple ore mineral assemblages and accompanying sulfides. Gold occurs either native gold or electrum with 20 to 40μm sizes, mostly observed in massive crystalline and bladed (parallel, acicular, lattice and ghost) quartz phases of the earliest stage. Intersections of high precious metal grades contains sulfide minerals like arsenopyrite, pyrite and trace amount of digenite which is probable a tennantite replacement. While sulfide abundance is relatively low ranging between 5-10% at overall quartz vein boulders in oxidized talus zone in Sırakayalar, it is clearly high ranging generally between 20-25% at damage zone underlying the talus zone in Sırakayalar.
- Disrupted veins at Sırakayalar represent the first example of a buried epithermal system in Biga Peninsula and suggests potential for similar epithermal Au-Ag mineralization in the region under younger cover.

REFERENCES

Altunkaynak, Ş., & Genç, Ş. C. (2008). Petrogenesis and time-progressive evolution of the Cenozoic continental volcanism in the Biga Peninsula, NW Anatolia (Turkey). Lithos, 102(1), 316-340.

Arribas Jr, A. (1995). Characteristics of high-sulfidation epithermal deposits, and their relation to magmatic fluid. Mineralogical Association of Canada Short Course, 23, 419-454.

Baker, T. (2019). Gold±copper endowment and deposit diversity in the Western Tethyan magmatic belt, southeast Europe: Implications for exploration. Economic Geology, 114(7), 1237-1250.

Beccaletto, L., & Jenny, C. (2004). Geology and correlation of the Ezine Zone: a Rhodope fragment in NW Turkey?. Turkish Journal of Earth Sciences, 13(2), 145-176.

Berger, B. R. & Henley, R. W. (1989). Advances in the Understanding of Epithermal Gold-Silver Deposits, with Special Reference to the Western United States. In R. W. Henley (Ed.), The Geology of Gold Deposits: The Perspective in 1988. essay, Society of Economics Geologists. DOI: https://doi.org/10.5382/Mono.06, ISBN (electronic): 9781629490014

Berra, F., & Angiolini, L. (2014). The Evolution of the Tethys Region throughout the Phanerozoic: A Brief Tectonic Reconstruction.

Bilir, M. E. (2015). Geochemical and geochronological characterization of the Early-Middle Eocene magmatism and related epithermal systems of the Eastern Pontides, Turkey. Muğla Sıtkı Koçman Üniversitesi (thesis).

Bingol, E., Akyurek, B., Korkmazer, B., 1975. Geology of the Biga Peninsula and some characteristics of the Karakaya Formation. Symposium Book of 50th anniversary of the Turkish Republic, MTA, Ankara, pp. 71–76 (in Turkish with English abstract).

Bonev, N., & Beccaletto, L. (2007). From syn-to post-orogenic Tertiary extension in the north Aegean region: constraints on the kinematics in the eastern Rhodope–Thrace, Bulgaria–Greece and the Biga Peninsula, NW Turkey. Geological Society, London, Special Publications, 291(1), 113-142.

Bozkaya, G., Banks, D., Ozbas, F., & Wallington, J. (2014). Fluid processes in the Tesbihdere base-metal-Au deposit: Implications for epithermal mineralization in the Biga Peninsula, NW Turkey. Open Geosciences, 6(2), 148-169.

Brun, J. P., & Sokoutis, D. (2007). Kinematics of the southern Rhodope core complex (North Greece). International Journal of Earth Sciences, 96(6), 1079-1099.

Brun, J. P., & Sokoutis, D. (2010). 45 my of Aegean crust and mantle flow driven by trench retreat. Geology, 38(9), 815-818.

Brunetti, P., Miskovic, A., Hart, C.J.R., Davies, A., Creasser, R. (2016, September). Geology of the Halilağa porphyry Cu-Au deposit and Emergence of an Eocene Metallogenic Belt in NW Turkey. SEG 2016 Conference: Tethyan Tectonics and Metallogeny, Çeşme,Turkey.

Cavazza, W., Okay, A. I., & Zattin, M. (2009). Rapid early-middle Miocene exhumation of the Kazdağ Massif (western Anatolia). International Journal of Earth Sciences, 98(8), 1935-1947.

Çelik, Ö. F., Marzoli, A., Marschik, R., Chiaradia, M., Neubauer, F., & Öz, İ. (2011). Early–middle Jurassic intra-oceanic subduction in the İzmir-Ankara-Erzincan Ocean, northern Turkey. Tectonophysics, 509(1-2), 120-134.

Christie, A. B., Simpson, M. P., Brathwaite, R. L., Mauk, J. L., & Simmons, S. F. (2007). Epithermal Au-Ag and Related Deposits of the Hauraki Goldfield, Coromandel Volcanic Zone, New Zealand. Economic Geology, 102(5), 785–816. doi:10.2113/gsecongeo.102.5.785

Çiçek, M., & Oyman, T. (2016). Origin and evolution of hydrothermal fluids in epithermal Pb-Zn-Cu±Au±Ag deposits at Koru and Tesbihdere mining districts, Çanakkale, Biga Peninsula, NW Turkey. Ore Geology Reviews, 78, 176-195.

Clark, J. N., Holwell, D. A., Siddle, R. J., & Keser, M. (2014). (rep.). Geochemical and mineralogical characteristics of the Şahinli epithermal Au-Ag deposits, Western Turkey (pp. 1–50).

Clark, R. N. (1999). Spectroscopy of rocks and minerals, and principles of spectroscopy. Remote Sensing for the Earth Sciences: Manual of Remote Sensing, 3, 3–58. https://doi.org/10.1111/j.1945-5100.2004.tb00079.x Hauff, P. (2008). An overview of VIS-NIR-SWIR field spectroscopy as applied to precious metals exploration. Arvada, Colorado: Spectral International Inc,.

Cooke, D. R., & McPhail, D. C. (2001). Epithermal Au-Ag-Te mineralization, Acupan, Baguio district, Philippines: numerical simulations of mineral deposition. Economic Geology, 96(1), 109-131.

Cooke, D. R., & Simmons, S. F. (2000). Characteristics and genesis of epithermal gold deposits. Reviews in Economic Geology, 13, 221-244.

Corbett, G. (2002). Epithermal gold for explorationists. AIG News, 67, 1-8.

Cunningham-Dunlop, I.R. (2011). Technical Report on the Halilağa Exploration Property, Çanakkale, Western Turkey (NI43-101). Retrieved from LibertyGold website: http://libertygold.ca/index.php/our-projects/halilaga/technical-reports

David A. John, Albert H. Hofstra, Robert J. Fleck, Jon E. Brummer, Eric C. Saderholm; Geologic Setting and Genesis of the Mule Canyon Low-Sulfidation Epithermal Gold-Silver Deposit, North-Central Nevada. Economic Geology 2003; 98 (2): 425–463. doi: https://doi.org/10.2113/gsecongeo.98.2.425

Delaloye, M., & Bingöl, E. (2000). Granitoids from western and northwestern Anatolia: geochemistry and modeling of geodynamic evolution. International Geology Review, 42(3), 241-268.

Dong, G., Morrison, G., & Jaireth, S. (1995). Quartz textures in epithermal veins, Queensland; classification, origin and implication. Economic Geology, 90(6), 1841-1856.

Dönmez, M., Akçay, A. E., Genç, Ş., & Acar, Ş. (2005). Biga yarımadasında Orta-Üst Eosen volkanizması ve denizel ignimbiritler. Maden Tetkik ve Arama Dergisi, (131), 49-61.

Dowling, K., & Morrison, G. (1989). Application of quartz textures to the classification of gold deposits using North Queensland examples. Economic Geology Monograph, 6, 342-355.

Du Bray, E. A. (2017). Geochemical characteristics of igneous rocks associated with epithermal mineral deposits—A review. Ore Geology Reviews, 80, 767–783. doi:10.1016/j.oregeorev.2016.08.023

Einaudi, M. T., Hedenquist, J. W., & Inan, E. E. (2003). Sulfidation state of fluids in active and extinct hydrothermal systems: Transitions from porphyry to epithermal environments. Special Publication-Society of Economic Geologists, 10, 285-314.

Emmons, W. H. (1918). Discussion of a paper headed" Genetic classification of underground volatile agents"[by RA Daly]. Economic Geology, 13(2), 144-145.

Ercan, T., Türkecan, A., Guillou, H., Satır, M., Sevin, D., & Şaroğlu, F. (1999). Features of the Tertiary volcanism around Sea of Marmara. Bulletin of the Mineral Research and Exploration, 120(120), 97-118.

Erenoglu, O., Bozcu, M., Billor, M.Z., 2022, Age and petrology of Eocene-Oligocene calc-alkaline volcanism in Biga Peninsula (NW Turkey): Implications for magma origin and geodynamic evolution. Journal of African Earth Sciences, v. 192, 104559.

Erkül, F., Helvaci, C., & Sözbilir, H. (2005). Evidence for two episodes of volcanism in the Bigadiç borate basin and tectonic implications for western Turkey. Geological Journal, 40(5), 545-570.

Frimmel, H. E. (2008). Earth's continental crustal gold endowment. Earth and Planetary Science Letters, 267(1-2), 45-55.

Gülyüz, N. (2017). Textural and structural characteristics of the Kestanelik epithermal vein system, NW Turkey: implications for permeability enhancement mechanisms and gold exploration in epithermal systems (Doctoral dissertation, University of Strathclyde).

Gülyüz, N., Gülyüz, E., Shipton, Z. K., Kuşcu, İ., & Lord, R. A. (2020). Geological and mineralization characteristics of the Kestanelik epithermal Au-Ag deposit in the Tethyan Metallogenic Belt, NW Turkey. Geosciences Journal, 24(4), 407-424.

Gülyüz, N., Shipton, Z. K., Kuşcu, İ., Lord, R. A., Kaymakcı, N., Gülyüz, E., & Gladwell, D. R. (2018). Repeated reactivation of clogged permeable pathways in epithermal gold deposits: Kestanelik epithermal vein system, NW Turkey. Journal of the Geological Society, 175(3), 509-524.

Günaydın, A. (2017). Arıklı Ve Nusratlı Köyleri (Ayvacik-Çanakkale) Yumrulu Fosfat Ve Fay Kontrollü Hidrotermal–Fosfat Cevherleşmelerinin Jeolojisi Ve Jeokimyasi. Maden Tetkik ve Arama Dergisi, (155), 135-150.

Halley, S. (2020). Mapping magmatic and hydrothermal processes from routine exploration geochemical analyses. Economic Geology, 115(3), 489-503.

Hedenquist, J. W., Arribas, A. N. T. O. N. I. O., & Gonzalez-Urien, E. (2000). Exploration for epithermal gold deposits. Reviews in Economic Geology, 13(2), 45-77.

Hedenquist, J. W., Arribas, A., & Gonzalez-Urien, E. (2000). Exploration for epithermal gold deposits. Reviews in Economic Geology, 13(2), 45-77.

Hedenquist, J. W., Arribas, A., & Reynolds, T. J. (1998). Evolution of an intrusion-centered hydrothermal system; Far Southeast-Lepanto porphyry and epithermal Cu-Au deposits, Philippines. Economic Geology, 93(4), 373-404.

Henley, R. W., & Ellis, A. J. (1983). Geothermal systems ancient and modern: a geochemical review. Earth-science reviews, 19(1), 1-50.

Hou, Z., Zaw, K., Pan, G., Mo, X., Xu, Q., Hu, Y., & Li, X. (2007). Sanjiang Tethyan metallogenesis in SW China: tectonic setting, metallogenic epochs and deposit types. Ore Geology Reviews, 31(1-4), 48-87.

Hunt, G. R. (1977). Spectral signatures of particulate minerals in the visible and near infrared. Geophysics, 42(3). https://doi.org/10.1190/1.1440721

İmer, E. Ü., Güleç, N., Kuşcu, İ., & Fallick, A. E. (2013). Genetic investigation and comparison of Kartaldağ and Madendağ epithermal gold deposits in Çanakkale, NW Turkey. Ore Geology Reviews, 53, 204-222.

Janković, S. (1977). The copper deposits and geotectonic setting of the Thethyan Eurasian Metallogenic Belt. Mineralium Deposita, 12(1), 37-47.

Jannas, R. R., Beane, R. E., Ahler, B. A., & Brosnahan, D. R. (1990). Gold and copper mineralization at the El Indio deposit, Chile. Journal of Geochemical Exploration, 36(1-3), 233-266.

Jannas, R. R., Bowers, T. S., Petersen, U., & Beane, R. E. (1999). High-sulfidation deposit types in the El Indio district, Chile. Society of Economic Geologists, 7, 219-266.

John, D. A. (2001). Miocene and early Pliocene epithermal gold-silver deposits in the northern Great Basin, western United States: Characteristics, distribution, and relationship to magmatism. Economic Geology, 96(8), 1827-1853.

John, D. A., Garside, L. J., Wallace, A. R., & Kizis, J. A. (1999). Magmatic and tectonic setting of late Cenozoic epithermal gold-silver deposits in northern Nevada, with an emphasis on the Pah Rah and Virginia Ranges and the northern Nevada rift. Geological Society of Nevada Special Publication, 29, 64-158.

Karacık, Z., Yılmaz, Y., Pearce, J. A., & Ece, Ö. I. (2008). Petrochemistry of the south Marmara granitoids, northwest Anatolia, Turkey. International Journal of Earth Sciences, 97(6), 1181-1200.

Kuşcu, İ., Tosdal, R. M., & Gençalioğlu-Kuşcu, G. (2019). Episodic porphyry Cu (-Mo-Au) formation and associated magmatic evolution in Turkish Tethyan collage. Ore Geology Reviews, 107, 119-154.

Kuşcu, İ., Tosdal, R. M., Gencalioğlu-Kuşcu, G., Friedman, R., & Ullrich, T. D. (2013). Late Cretaceous to middle Eocene magmatism and metallogeny of a portion of the southeastern Anatolian orogenic belt, east-central Turkey. Economic Geology, 108(4), 641-666.

Leroux, G. M. (2016). Stratigraphic and petrographic characterization of HS epithermal Au-Ag mineralization at the TV Tower district, Biga Peninsula, NW Turkey (Doctoral dissertation, University of British Columbia).

Mark H. Reed, Nicolas F. Spycher, 1985. "Boiling, Cooling, and Oxidation in Epithermal Systems: A Numerical Modeling Approach", Geology and Geochemistry of Epithermal Systems, B. R. Berger, P. M. Bethke

Moghadam, H. S., Khademi, M., Hu, Z., Stern, R. J., Santos, J. F., & Wu, Y. (2015). Cadomian (Ediacaran–Cambrian) arc magmatism in the ChahJam–Biarjmand metamorphic complex (Iran): Magmatism along the northern active margin of Gondwana. Gondwana Research, 27(1), 439-452.

Moix, P., Beccaletto, L., Kozur, H. W., Hochard, C., Rosselet, F., & Stampfli, G. M. (2008). A new classification of the Turkish terranes and sutures and its implication for the paleotectonic history of the region. Tectonophysics, 451(1), 7-39.

Moncada, D., Mutchler, S., Nieto, A., Reynolds, T. J., Rimstidt, J. D., & Bodnar, R. J. (2012). Mineral textures and fluid inclusion petrography of the epithermal Ag–Au deposits at Guanajuato, Mexico: Application to exploration. Journal of Geochemical Exploration, 114, 20-35.

Moritz, R., Rezeau, H., Ovtcharova, M., Tayan, R., Melkonyan, R., Hovakimyan, S., ... & Putlitz, B. (2016). Long-lived, stationary magmatism and pulsed porphyry systems during Tethyan subduction to post-collision evolution in the southernmost Lesser Caucasus, Armenia and Nakhitchevan. Gondwana Research, 37, 465-503.

Murakami, H., Watanabe, Y., Stein, H. (2005) - Re-Os ages for molybdenite from the Tepeoba breccia-centered Cu-Mo-Au deposit, western Turkey: Brecciation-triggered mineralization. In: Mao, J., Bierlein, F.P., (Eds.), Mineral Deposit Research:Meeting the Global Challenge, Proceedings of the Eight Biennial SGA Meeting, Beijing, China, 18-21 August, 2005, pp. 805-808.

Nollan, T. B. (1933). Epithermal precious-metal deposits of the western states. In Lindgren volume (pp. 623-640). American Institute of Mining and Metallurgical Engineers.

Okay, A. I., & Göncüoğlu, M. C. (2004). The Karakaya Complex: a review of data and concepts. Turkish Journal of Earth Sciences, 13(2), 75-95.

Okay, A. I., & Satir, M. (2000a). Coeval plutonism and metamorphism in a latest Oligocene metamorphic core complex in northwest Turkey. Geological Magazine, 137(5), 495-516.

Okay, A. İ., & Satir, M. (2000b). Upper Cretaceous eclogite-facies metamorphic rocks from the Biga Peninsula, Northwest Turkey. Turkish Journal of Earth Sciences, 9(2-3), 47-56.

Okay, A. I., & Tüysüz, O. (1999). Tethyan sutures of northern Turkey. Geological Society, London, Special Publications, 156(1), 475-515.

Okay, A. I., Satir, M., Maluski, H., Siyako, M., Monie, P., Metzger, R., & Akyuz, S. (1996). Paleo-and Neo-Tethyan events in northwest Turkey Geological and geochronological constraints, Tectonic Evolution of Asia A. Yin, M. Harrison, 420–441.

Okay, A. I., Siyako, M., & Bürkan, K. A. (1990). Geology and tectonic evolution of the Biga Peninsula. Bulletin of the Turkish Association of Petroleum Geologists, 2(1), 83-121.

Okay, A. I., Siyako, M., & Bürkan, K. A. (1991). Geology and tectonic evolution of the Biga Peninsula, northwest Turkey. Bulletin of the Technical University of Istanbul, 44(1-2), 191-256.

Pracejus, B. (2015). The ore minerals under the microscope: an optical guide, (pp. 120). Elsevier.

Rabayrol, F., Hart, C. J., Friedman, R. M., & Spikings, R. A. (2021). Diachronous Magmatic and Cu-Au-Mo Metallogenic Responses to Slab Roll-Back Initiation from Northwest Anatolia to the Balkans, Western Tethyan Eocene Magmatic Belt.

Ransome, F. L. (1907). The association of alunite with gold in the Goldfield district, Nevada. Economic Geology, 2(7), 667-692.

Ransome, F. L. (1907). The association of alunite with gold in the Goldfield district, Nevada. Economic Geology, 2(7), 667-692.

Reyes, A.G., 1990: Petrology of Philippine geothermal systems and the application of alteration mineralogy to their assessment. 1. Volcanol. Geotherm. Res., 43, 279-309.

Richards, J. P. (2015). Tectonic, magmatic, and metallogenic evolution of the Tethyan orogen: From subduction to collision. Ore Geology Reviews, 70, 323-345.

Richards, J. P., & Sholeh, A. (2016). The Tethyan tectonic history and Cu-Au metallogeny of Iran. Tectonics and Metallogeny of the Tethyan Orogenic Belt. Society of Economic Geologists, Special Publication, 19, 193-212.

Ring, U., Glodny, J., Will, T., & Thomson, S. (2010). The Hellenic subduction system: high-pressure metamorphism, exhumation, normal faulting, and large-scale extension. Annual Review of Earth and Planetary Sciences, 38, 45-76.

Rinne, M. L., Cooke, D. R., Harris, A. C., Finn, D. J., Allen, C. M., Heizler, M. T., & Creaser, R. A. (2018). Geology and geochronology of the Golpu porphyry and Wafi epithermal deposit, Morobe Province, Papua New Guinea. Economic Geology, 113(1), 271-294.

Rye, R. O., Bethke, P. M., & Wasserman, M. D. (1992). The stable isotope geochemistry of acid sulfate alteration. Economic Geology, 87(2), 225-262.

Sanchez, M. G., McClay, K. R., King, A. R., & Wijbrams, J. R. (2016). Cenozoic Crustal Extension and Its Relationship to Porphyry Cu-Au-(Mo) and Epithermal Au-(Ag) Mineralization in the Biga Peninsula, Northwestern Turkey. Society of Economic Geologists, Inc. Special Publication, 19, 113-156.

Sander, M. V., & Black, J. E. (1988). Crystallization and recrystallization of growth-zoned vein quartz crystals from epithermal systems; implications for fluid inclusion studies. Economic Geology, 83(5), 1052-1060.

Sayit, K., Bedi, Y., Tekin, U. K., Göncüoglu, M. C., & Okuyucu, C. (2017). Middle Triassic back-arc basalts from the blocks in the Mersin Mélange, southern Turkey: Implications for the geodynamic evolution of the Northern Neotethys. Lithos, 268, 102-113.

Sayıt, K., & Göncüoglu, M. C. (2013). Geodynamic evolution of the Karakaya Mélange Complex, Turkey: a review of geological and petrological constraints. Journal of Geodynamics, 65, 56-65.

Şengör, A. C., & Yilmaz, Y. (1981). Tethyan evolution of Turkey: a plate tectonic approach. Tectonophysics, 75(3-4), 181-241.

Şengün, F., Yiğitbaş, E., & Tunç, I. O. (2011). Geology and tectonic emplacement of eclogite and blueschists, Biga peninsula, northwest Turkey. Turkish Journal of Earth Sciences, 20(3), 273-285.

Seward, T. (1973). Thio complexes of gold and the transport of gold in hydrothermal ore solutions. Geochimica et Cosmochimica Acta, 37(3), 379–399. doi:10.1016/0016-7037(73)90207-x

Seward, T. M. (1989). The hydrothermal chemistry of gold and its implications for ore formation: boiling and conductive cooling as examples.

Seward, T. M., Williams-Jones, A. E., & Migdisov, A. A. (2014). 13.2–The chemistry of metal transport and deposition by ore-forming hydrothermal fluids. Treatise on geochemistry, 29-57.

Shimizu, T. (2014). Reinterpretation of quartz textures in terms of hydrothermal fluid evolution at the Koryu Au-Ag deposit, Japan. Economic Geology, 109(7), 2051-2065.

Sillitoe, R. H. (2015). Epithermal paleosurfaces. Mineralium Deposita, 50(7), 767-793.

Sillitoe, R. H. (2015). Epithermal paleosurfaces. Mineralium Deposita, 50(7), 767-793.

Sillitoe, R. H., & Bonham, H. F. (1984). Volcanic landforms and ore deposits. Economic Geology, 79(6), 1286-1298.

Sillitoe, R. H., & Hedenquist, J. W. (2003). Linkages between volcanotectonic settings, ore-fluid compositions, and epithermal precious metal deposits. Special Publication-Society of Economic Geologists, 10, 315-343.

Simmons, S. F., & Browne, P. R. (2000). Hydrothermal minerals and precious metals in the Broadlands-Ohaaki geothermal system: Implications for understanding low-sulfidation epithermal environments. Economic Geology, 95(5), 971-999.

Simmons, S. F., White, N. C., & John, D. A. (2005). Geological characteristics of epithermal precious and base metal deposits.

Simmons, S. F., White, N. C., & John, D. A. (2005). Geological characteristics of epithermal precious and base metal deposits. Society of Economic Geologists, 100, 485-522.

Siyako, M., Bürkan, K. A., & Okay, A. I. (1989). Tertiary geology and hydrocarbon potential of the Biga and Gelibolu peninsulas. Turkish Association of Petroleum Geologists Bulletin, 1(3), 183-99.

Smith, M. T., Lepore, W. A., Incekaraoğlu, T., Shabestari, P., Boran, H., & Raabe, K. (2014). Küçükdağ: A New, High Sulfidation Epithermal Au-Ag-Cu Deposit At The Tv Tower Property In Western Turkey. Economic Geology, 109(6), 1501-1511.

Stampfli, G. M. (2000). Tethyan oceans. Geological society, london, special publications, 173(1), 1-23.

Stampfli, G. M., & Borel, G. D. (2002). A plate tectonic model for the Paleozoic and Mesozoic constrained by dynamic plate boundaries and restored synthetic oceanic isochrons. Earth and Planetary Science Letters, 196(1-2), 17-33.

Stampfli, G. M., & Borel, G. D. (2004). The TRANSMED transects in space and time: constraints on the paleotectonic evolution of the Mediterranean domain. In The TRANSMED Atlas. The Mediterranean region from crust to mantle (pp. 53-80). Springer, Berlin, Heidelberg.

Stoffregen, R. E. (1987). Genesis of acid-sulfate alteration and Au-Cu-Ag mineralization at Summitville, Colorado. Economic Geology, 82(6), 1575-1591.

Taylor, B. E. (2007). Epithermal gold deposits. Mineral Deposits of Canada: A synthesis of major deposit-types, district metallogeny, the evolution of geological provinces, and exploration methods: Geological Association of Canada, Mineral Deposits Division, Special Publication, 5, 113-139.

Teal, L., & Benavides, A. (2010). History and geologic overview of the Yanacocha mining district, Cajamarca, Peru. Economic Geology, 105(7), 1173-1190.

Tekin, U.K., Goncuoglu, M.C., Turhan, N., 2002. First evidence of Late Carnian radiolarians from the zmir-Ankara suture complex, central Sakarya, Turkey : implications for the opening age of the Izmir-Ankara branch of Neo-Tethys. Geobios 35, 127–135.

Tekin, U. K., Okuyucu, C., Sayit, K., Bedi, Y., Noble, P. J., Krystyn, L., & Göncüoglu, M. C. (2019). Integrated Radiolaria, benthic foraminifera and conodont biochronology of the pelagic Permian blocks/tectonic slices and geochemistry of associated volcanic rocks from the Mersin Mélange, southern Turkey: Implications for the Permian evolution of the northern Neotethys. Island Arc, 28(2), e12286.

Tobisch, O. (2005). A PRACTICAL GUIDE TO ROCK MICROSTRUCTURE: by Ron H. Vernon. Cambridge, 2004. 594 pp. Hardbound 130,softbound 70.

Tunç, İ. O., Yiğitbaş, E., Şengün, F., Wazeck, J., Hofmann, M., & Linnemann, U. (2012). U-Pb zircon geochronology of northern metamorphic massifs in the Biga Peninsula (NW Anatolia-Turkey): new data and a new approach to understand the tectonostratigraphy of the region. Geodinamica Acta, 25(3-4), 202-225.

Tüysüz, O., Dellaloğlu, A. A., & Terzioğlu, N. (1995). A magmatic belt within the Neo-Tethyan suture zone and its role in the tectonic evolution of northern Turkey. Tectonophysics, 243(1-2), 173-191.

Ünal, E. (2010). Genetic investigation and comparison of Kartaldağ and Madendağ epithermal gold mineralization in Çanakkale-region, Turkey (Master's thesis, Middle East Technical University).

Vila, T., & Sillitoe, R. H. (1991). Gold-rich porphyry systems in the Maricunga belt, northern Chile. Economic Geology, 86(6), 1238-1260.

von Quadt, A., Moritz, R., Peytcheva, I., & Heinrich, C. A. (2005). 3: Geochronology and geodynamics of Late Cretaceous magmatism and Cu–Au mineralization in the Panagyurishte region of the Apuseni–Banat–Timok–Srednogorie belt, Bulgaria. Ore Geology Reviews, 27(1-4), 95-126.

Warren, I., Simmons, S. F., & Mauk, J. L. (2007). Whole-rock geochemical techniques for evaluating hydrothermal alteration, mass changes, and compositional gradients associated with epithermal Au-Ag mineralization. Economic Geology, 102(5), 923-948.

White, N. C., & Hedenquist, J. W. (1995). Epithermal gold deposits: styles, characteristics and exploration. SEG Discovery, (23), 1-13.

White, N. C., Leake, M. J., McCaughey, S. N., & Parris, B. W. (1995). Epithermal gold deposits of the southwest Pacific. Journal of geochemical exploration, 54(2), 87-136.

Yigit, O. (2009). Mineral deposits of Turkey in relation to Tethyan metallogeny: implications for future mineral exploration. Economic Geology, 104(1), 19-51.

Yigit, O. (2012). A prospective sector in the Tethyan Metallogenic Belt: Geology and geochronology of mineral deposits in the Biga Peninsula, NW Turkey. Ore Geology Reviews, 46, 118-148.

Yılmaz, H. (2002). Ovacik gold deposit: An example of quartz-adularia–type gold mineralization in Turkey. Economic Geology, 97(8), 1829-1839.

Yilmaz, H., Oyman, T., Sonmez, F. N., Arehart, G. B., & Billor, Z. (2010). Intermediate sulfidation epithermal gold-base metal deposits in Tertiary subaerial volcanic rocks, Şahinli/Tespih Dere (Lapseki/Western Turkey). Ore Geology Reviews, 37(3), 236-258

Zeeck, L. R. (2018). The Role of Flashing in the Formation of High-Grade, Low-Sulfidation Epithermal Deposits: A Case Study from the Omu Camp in Hokkaido, Japan. Colorado School of Mines.